GEOLOGICA ULTRAIECTINA

Mededelingen van het
Instituut voor Aardwetenschappen der
Rijksuniversiteit te Utrecht

No. 49

A HYBRID METHOD FOR THE SOLUTION OF SEISMIC WAVE PROPAGATION PROBLEMS

ARIE VAN DEN BERG

GEOLOGICA ULTRAIECTINA

Mededelingen van het
Instituut voor Aardwetenschappen der
Rijksuniversiteit te Utrecht

No. 49

A HYBRID METHOD FOR THE SOLUTION OF SEISMIC WAVE PROPAGATION PROBLEMS

CIP-GEGEVENS KONINKLIJKE BIBLIOTHEEK, DEN HAAG

Berg, Arie Pieter van den

A hybrid method for the solution of seismic wave
propagation problems / Arie Pieter van den Berg.
- [S.l. : s.n.]. - Ill. - (Geologica Ultraiectina ; no. 49)
Proefschrift Utrecht. - Met lit. opg.
ISBN 90-71577-04-X
SISO 562 UDC 681.3.001.572:550.34.01(043.3)
Trefw.: geofysica.

A HYBRID METHOD FOR THE SOLUTION OF SEISMIC WAVE PROPAGATION PROBLEMS

EEN HYBRIDE OPLOSSINGSMETHODE VOOR SEISMISCHE GOLFVOORTPLANTINGSPROBLEMEN

(met een samenvatting in het Nederlands)

PROEFSCHRIFT

TER VERKRIJGING VAN DE GRAAD VAN DOCTOR AAN
DE RIJKSUNIVERSITEIT TE UTRECHT, OP GEZAG VAN
DE RECTOR MAGNIFICUS PROF. DR. J.A. VAN GINKEL
VOLGENS BESLUIT VAN HET COLLEGE VAN DEKANEN
IN HET OPENBAAR TE VERDEDIGEN OP MAANDAG
2 NOVEMBER 1987 DES NAMIDDAGS TE 12.45 UUR

DOOR

ARIE PIETER VAN DEN BERG

GEBOREN OP 24 JUNI 1950 TE OUD-BEIJERLAND

PROMOTOR: PROF. DR. N.J. VLAAR

(VERBONDEN AAN DE FACULTEIT GEOLOGIE EN GEOFYSICA)

voor mijn ouders
voor Annemiek en Niels

The research described in this thesis was carried out at the:

Institute of Earth Sciences,
Department of Theoretical Geophysics
P.O. Box 80.025
3508 TA Utrecht
The Netherlands

Contents

SAMENVATTING

Voortdurende verbeteringen in data acquisitie technieken leiden tot een toename in quantiteit en kwaliteit van de data, die beschikbaar zijn voor interpretatie in termen van aardmodellen. Tegelijkertijd biedt de toenemende capaciteit van de computers aangewend bij de interpretatie van deze data de mogelijkheid gedetailleerder modellen te gebruiken in computer simulaties en inversie berekeningen. Een gevolg hiervan is, dat onze kennis van de structuur en de evolutie van de aarde voortdurend toeneemt. Naast de vooruitgang van de theorie stellen de toegenomen mogelijkheden op het gebied van computer simulatie (modeleren) ons in staat nauwkeuriger voorspellingen en analyses van aardbevingsrisico's uit te voeren. Meer detail en grotere flexibiliteit in aardmodellen, vereisen de implementatie van nieuwe berekeningsmethoden om de modellen numeriek te kunnen simuleren. Verschillende berekeningsmethoden zijn gebaseerd op de methode van separatie van variabelen, wat de toepasbaarheid beperkt tot betrekkelijk eenvoudige modellen. Aan de andere kant worden technieken die deze beperkingen niet kennen, bijvoorbeeld discretisatie methoden, zoals de eindige differentie methode en de eindige elementen methode, in hun toepasbaarheid beperkt door de begrenzing van computer geheugens en processor snelheden.

In dit proefschrift wordt een methode gepresenteerd voor de berekening van de seismische respons van een klasse van modellen, opgebouwd uit een regelmatig achtergrond medium, met een anomalie in de vorm van een onregelmatig insluitsel van beperkt volume. Deze methode combineert een eindige elementen formulering voor de begrensde anomalie met een integraal representatie voor het regelmatig achtergrond medium. De integraal representatie bevat integraal kernen, die samenhangen met de Greense functie van het achtergrond medium. We definieren een achtergrond medium regelmatig als er een algoritme beschikbaar is voor de Greense functie. Omdat deze hybride methode slechts gedeeltelijk berust op een eindige elementen formulering zijn de beperkingen tengevolge van beperkte computer faciliteiten minder stringent als voor een volledige eindige elementen methode.

Beschouw als illustratie van de specifieke voordelen van de methode het volgende probleem. Stel dat we effecten van een plaatselijke anomalie op de bodembeweging aan het aardoppervlak willen modelleren, voor een invallende golf geexciteerd door een aardbeving op teleseismische afstand. Als de afmetingen van de anomalie klein zijn ten opzichte van de straal van de aarde en de afstand van de anomalie tot de aardbevingshaard, dan kunnen we het model gebruiken van een vlakke golf, invallend vanuit een regelmatige halfruimte met een anomalie nabij het vrije oppervlak. De aanwezigheid van een onregelmatige anomalie sluit het gebruik van analytische methoden om dit probleem op te lossen uit. Als we een discretisatie methode willen gebruiken, worden we door beperkte computer faciliteiten gedwongen om een eindig model van het medium te gebruiken, waardoor kunstmatige randen worden geintroduceerd. Door dit laatste worden we geconfronteerd met het probleem van ongewenste randeffecten en de vraag hoe de excitatie van het eindige model dient te worden gespecificeerd. Bij toepassing van de hybride methode voor dit probleem hoeven we alleen de locale anomalie te discretiseren en zal het niet nodig zijn (voor een anomalie

van beperkt volume) het model af te breken. De invloed van het achtergrond medium en de excitatie van het golfveld zijn beide in de integraal representatie opgenomen. Hierdoor kampen we niet langer met ongewenste randeffecten en de excitatie van het golfveld wordt op een juiste wijze verwerkt.
De formulering van de hybride eindige elementen / integraalvergelijking techniek wordt afgeleid voor het algemene geval van elastische golven in een drie dimensionaal (3-D) algemeen achtergrond medium, met een insluitsel met eindig volume. De methode is geimplementeerd voor het beperkter geval van horizontaal gepolariseerde shear (SH) golven in een homogeen 2-D medium met een eindig onregelmatig insluitsel.
Een beknopte formulering van de hybride methode is gepubliceerd in (van den Berg, 1984) en recenter, met uitkomsten van berekeningen, in (van den Berg, 1987).

Hoofdstuk 2 van dit proefschrift begint met een specificatie van het op te lossen probleem type in termen van de bewegingsvergelijking en met een definitie van gebruikte notaties. In hoofdstuk 3 worden de eindige elementen vergelijkingen geintroduceerd. De benaderende uitdrukkingen voor het golfveld worden gedefinieerd en de bewegingsvergelijking wordt gediscretiseerd, resulterend in een stelsel algebraische vergelijkingen. In hoofdstuk 4 wordt de integraal representatie geintroduceerd. Deze wordt vervolgens gediscretiseerd - resulterend in een stelsel algebraische vergelijkingen - en de evaluatie van de coefficienten van de vergelijking wordt besproken. Het 2-D scalair geval wordt meer in detail behandeld. Hoofdstuk 5 behandelt de structuur van de in hoofdstuk 3 en 4 afgeleide gekoppelde algebraische vergelijkingen. Er wordt een efficient numeriek schema beschreven om de simultane vergelijkingen op te lossen. In hoofdstuk 6 worden uitkomsten van berekeningen gegeven voor verschillende scalaire 2-D golfdiffractie problemen. Sectie 6.1 behandelt de diffractie van een vlakke golf door een cylinder. De uitkomsten van de berekeningen worden vergeleken met resultaten van een reeksoplossing. In sectie 6.2 modeleren we de respons van rechthoekige onregelmatigheden op een aantal verschillende golfveld excitaties. Sectie 6.3 geeft de resultaten voor modellen van een halfruimte met een anomalie aan het oppervlak. Sectie 6.3.1 behandelt een canyon topografie; sectie 6.3.2 een lage snelheids afzetting aan het vrije oppervlak. Er wordt een vergelijking gemaakt tussen uitkomsten van de hybride methode en een eindige differentie methode. In hoofdstuk 7 worden conclusies samengevat.
De appendix behandelt meer gedetaileerd een aantal onderwerpen, die relevant zijn voor het eerste deel van het proefschrift. In appendix A wordt de in de hybride methode gebruikte interpolatie van vector velden besproken. Appendix B bevat een afleiding van de gebruikte integraal representatie, inclusief termen die de excitatie door een invallend golfveld beschrijven. Appendix C behandelt het eenduidigheids probleem samenhangend met de integraal vergelijking voor bepaalde frequenties. Appendix D geeft een globale beschrijving van een implementatie van de hybride methode in een programma pakket.

Chapter 1

SUMMARY

Continuing improvements in data acquisition techniques result in an increase in quantity and quality of data available for interpretation in terms of earth models. At the same time increasing performance of computers used in the interpretation process allows more detailed models to be used in computer simulation and inversion. As a result, our knowledge of the structure and evolution of the earth is continuously increasing. Apart from the theoretical benefits, our growing abilities in computer simulation (modeling) allow us to make more precise predictions and risk assessments. More detail and greater flexibility in earth models, require the implementation of new computational techniques, to simulate the models numerically. Many computational techniques are based on a separation of variables, which limits their applicability to relatively simple models. On the other hand, techniques that do not have these limitations, such as discretization techniques like the finite difference and finite element method, are limited in their applicability by practical restrictions, such as finite computer memory and speed of computation.

In this thesis a method is presented to compute the seismic response of a class of models, consisting of a regular background medium, with an irregular inclusion of finite extent. In this method the wave field on the bounded inclusion is formulated using a finite element description. For the wave field in the - possibly infinite - regular background medium we use an integral representation. The integral representation involved contains integral kernels related to the Green's function of the background medium. We define a background medium to be regular when an algorithm for the Green's function is available. Because this hybrid method relies only partly on a finite element formulation, the restrictions imposed by finite computer resources are less severe then for a full finite element method.

As an illustration of the specific advantages of the method, consider the following problem. Suppose we want to model the effects of a local anomaly on the ground motion at the earth's surface, in the presence of an incident wave, excited by an earthquake at a teleseismic distance. If the dimensions of the anomaly are small compared to the radius of the earth and the distance between the anomaly and the earthquake source, we can use as a model a plane wave, incident from a regular halfspace containing a localized anomaly near the free surface. The presence of an irregular anomaly excludes the use of analytical methods to solve this problem. If we want to use a discretization method, the fact that we are restricted to finite computer resources forces us to truncate the model of the medium, introducing artificial boundaries. This leaves us with the problem how to deal with the undesirable boundary effects and how to specify the model excitation in the finite model. Using the hybrid method for this type of problem we

only have to discretize the localized anomaly and a truncation of the model will not be necessary (assuming an anomaly of limited volume). The effect of the background medium and the wave field excitation are both included in the integral representation, therefore we no longer have undesirable boundary effects and the wave field excitation is handled correctly.
We derive the formalism for the hybrid finite element / integral equation technique for the general case of elastic wave propagation problems in a three dimensional (3-D) general background medium, with an inclusion of finite volume. The method has been implemented for the more restricted case of SH waves in a homogeneous 2-D medium with a finite irregular inclusion.
A concise description of the formalism of the hybrid method has been published in (van den Berg, 1984) and more recently, including computational results, in (van den Berg, 1987).

In chapter 2 of this thesis we start with a specification of the type of problem to be solved in terms of the equation of motion and with a definition of notations used. Chapter 3 contains an introduction of the finite element equations. The approximating expressions for the wave field are defined and the equation of motion is discretized, resulting in a system of algebraic equations. In chapter 4 the boundary integral representation is introduced. The representation is then discretized - resulting in a system of algebraic equations - and the evaluation of the equation coefficients is discussed. The 2-D scalar case is treated in greater detail. Chapter 5 treats the structure of the coupled algebraic equations derived in chapters 3 and 4. It presents an efficient numerical solution scheme for the simultaneous equations. In chapter 6 we present numerical results for several 2-D scalar wave diffraction problems. Section 6.1 treats the diffraction of a plane wave by a cylinder. The numerical results are compared with results from a series solution. In section 6.2 we model the response of rectangular irregularities for a number of different wave field excitations. Section 6.3 gives results for models of a halfspace, with an anomaly at the surface. Section 6.3.1 deals with a canyon topography, section 6.3.2 with a low velocity fill at the free surface. A comparison is made between results of the hybrid method and a finite difference method. In chapter 7 conclusion are summarized.
The appendix treats a number of topics, relevant for the main part of the thesis, in more detail. In Appendix A the interpolation of vector fields used in the hybrid method is discussed. Appendix B contains a derivation of the integral representation used, including terms describing the excitation by an incident wave field. Appendix C treats the uniqueness problem connected with the integral equation, for certain frequencies. Appendix D gives an outline of an implementation of the hybrid method in a program package .

Chapter 2

PROBLEM STATEMENT

In the following we will define the field equations of motion dealt with in the remainder of this thesis.
The following notational conventions are adopted:

(1) Continuous fields and their indices such as vector and tensor fields are denoted by lower case symbols.

(2) Vectors of discrete (sampled) field values and their indices are printed in upper case symbols.

(3) Non scalar quantities, vectors, tensors and matrices are printed in boldface symbols.

(4) The summation convention applies for repeated indices.

The particle displacement field in an elastic medium is described by the elastodynamic equation (Aki and Richards, 1981)

$$\rho \frac{\partial^2 u_i}{\partial t^2} = \partial_j \tau_{ij} + f_i \tag{2.1}$$

where we use the notation defined in table 2.1. The stress tensor τ_{ij} is related to the displacement field through the stress-strain relation. We consider a linear stress-strain relation only, which takes the general form

$$\tau_{ij} = c_{ijkl}\,\varepsilon_{kl} = c_{ijkl}\,1/2(\partial_k u_l + \partial_l u_k) = c_{ijkl}\,\partial_k u_l \tag{2.2}$$

where c_{ijkl} is the stress-strain tensor and $\varepsilon_{kl} = 1/2(\partial_k u_l + \partial_l u_k)$ is the strain tensor. For an isotropic medium we have

$$c_{ijkl} = \lambda \delta_{ij} \delta_{kl} + \mu(\delta_{ik}\delta_{jl} + \delta_{il}\delta_{jk}) \tag{2.3}$$

δ_{ij} is the Kronecker delta, λ and μ are the Lamé parameters, (Aki and Richards, 1981).

We will mainly deal with a frequency domain description of the field equations. Transforming (2.1) to the frequency domain, using the transform pair

$$H(\omega) = \int_{-\infty}^{\infty} h(t) e^{i\omega t}\, dt \tag{2.4a}$$

table 2.1 list of notations used

ρ	mass density
λ,μ	Lamé parameters
c_{ijkl}	stress-strain tensor
x_i	i^{th} cartesian coordinate of a point in space
u_i	i^{th} component of the particle displacement field
τ_{ij}	i,j^{th} element of the stress tensor
f_i	i^{th} component of the body force field
$\frac{\partial}{\partial t}$	partial derivative with respect to time
∂_j	partial derivative with respect to the cartesian coordinate x_j

$$h(t) = \frac{1}{2\pi} \int_{-\infty}^{\infty} H(\omega) e^{-i\omega t}\, d\omega \tag{2.4b}$$

we get for the elastodynamic equation

$$\partial_j \tau_{ij}(\mathbf{x},\omega) + \rho\omega^2 u_i(\mathbf{x},\omega) = -f_i(\mathbf{x},\omega) \tag{2.5}$$

As in (2.5), identical notations are used for both the frequency and time domain representations of the fields. In most cases the field arguments will be omitted from the equations. We consider wave propagation problems in inhomogeneous media i.e the physical parameters ρ,λ,μ are functions of the space coordinates. In particular we consider regular unbounded media V_∞ with an irregular inclusion of finite extent V. We define a medium to be regular when an algorithm is available for the Green's function of the medium (Aki and Richards, 1981). The i^{th} component of the Green's displacement field at a point $\mathbf{x}$, due to a point force at a point $\mathbf{x}_0$ in the direction of the k^{th} axis is denoted as $u_i^k(\mathbf{x},\mathbf{x}_0)$. Likewise, the stress tensor for the same Green's displacement is written as $\tau_{ij}^k(\mathbf{x},\mathbf{x}_0)$. The Green's function is a solution of the fundamental equation

$$\partial_j \tau_{ij}^k(\mathbf{x},\omega) + \rho\omega^2 u_i^k(\mathbf{x},\omega) = -\delta_{ik}\,\delta(\mathbf{x}-\mathbf{x}_0) \tag{2.6}$$

- where $\delta(\mathbf{x})$ is the Dirac delta function in 3-D space. When the irregular inclusion is in welded contact with its exterior, the particle displacement u_i and the traction vector $t_i = \tau_{ij} n_j$ across its boundary surface ∂V is continuous. A further condition to be imposed on the wave field is the radiation condition. Kupradze (1963) and Tan (1975) discuss alternative forms of a radiation condition, prescribing the asymptotic behaviour of the wave field at large distance from the source. This radiation condition is used in the derivation of integral representations for the wave field in an unbounded medium.
In this thesis we will show how the equation (2.5), for a bounded volume, supplemented with an integral equation (introduced in chapter 4) on the boundary surface can be solved. Once the frequency domain solution to the equations has been obtained for a band of (discrete) frequency values, the corresponding time domain solution can be obtained using the (discrete) inverse Fourier transform.

Chapter 3

FINITE ELEMENT FORMULATION FOR THE WAVE FIELD IN A BOUNDED VOLUME

For the wave field in a region of limited volume we use a description in terms of finite elements. The finite element method (FEM) is a powerful method to construct numerical solutions of partial differential equations. Extensive descriptions of the FEM are given in text books by Desai and Abel (1972), Strang and Fix (1973) and Zienkiewicz (1977). The method offers a great flexibility in the geometry of the solution domain and an important advantage over other methods such as the finite difference method is its capability to use irregular space grids. Using irregular grids one can handle regions with variable grid point density depending on the spatial variation of the solution, and the physical parameters of the medium. Previous applications of the finite element method to seismological problems, mainly dealing with surface waves, can be found in (Lysmer and Kuhlemeyer, 1969) and (Lysmer and Drake, 1971). Applications to body wave propagation problems were given by Smith (1975) and Day (1977).
This chapter is subdivided in the following way: in section 3.1 the discretization of the elastodynamic fields is specified, in section 3.2 we derive the finite element equations in the frequency domain for the general elastodynamic case and in section 3.3 the use of boundary conditions with the finite element formalism is discussed.

3.1. Discretization of the elastodynamic fields

The equation of motion in the frequency domain introduced in chapter 2 is

$$-\partial_j \tau_{ij} - \rho\omega^2 u_i = f_i \tag{3.1}$$

We will reduce this partial differential equation to a set of linear algebraic equations using the finite element method. To this end we define a space grid of connected nodal points on the solution domain V of (3.1) and we replace the displacement vector field $\mathbf{u}(\mathbf{x})$ by an approximation in terms of nodal point values using interpolation. A more extended discussion of vector field approximation by means of interpolation can be found in appendix A.

We denote the approximate field with an overbar $\bar{\mathbf{u}}(\mathbf{x}) \approx \mathbf{u}(\mathbf{x})$,

$$u_i(\mathbf{x}) \approx \bar{u}_i(\mathbf{x}) = \sum_{M=1}^{N} u_i(\mathbf{x}_M)\phi_M(\mathbf{x}) \quad , \mathbf{x} \in V \tag{3.2}$$

where the $\mathbf{x}_M$, $M=1, \cdots, N$ are the nodal points and the scalars $\phi_M(\mathbf{x})$ are the interpolating functions (see appendix A).
Next we rearrange the displacement components $u_i(\mathbf{x}_M)$ in (3.2) in a single vector with dN components;

$$u_i(\mathbf{x}_M) = U_K \quad , K = d(M-1)+i \quad , M=1, \cdots, N \tag{3.3}$$

where d is the number of components in the displacement field.
Substitution of (3.3) into (3.2) results in:

$$\bar{u}_i(\mathbf{x}) = \sum_{K=1}^{dN} U_K \Phi_{iK}(\mathbf{x}) \tag{3.4}$$

where the interpolation matrix $\Phi(\mathbf{x})$ (for the case $d=3$) is given by:

$$\Phi(\mathbf{x}) = \begin{bmatrix} \phi_1(\mathbf{x}) & 0 & 0 & \cdots & \phi_N(\mathbf{x}) & 0 & 0 \\ 0 & \phi_1(\mathbf{x}) & 0 & \cdots & 0 & \phi_N(\mathbf{x}) & 0 \\ 0 & 0 & \phi_1(\mathbf{x}) & \cdots & 0 & 0 & \phi_N(\mathbf{x}) \end{bmatrix} \tag{3.5}$$

On the boundary surface ∂V of the domain V we will introduce the traction field as a separate unknown, and approximate this field in terms of nodal point values using interpolation.
Denoting the approximated field by an overbar we have :

$$\tau_{ij} n_j = t_i \approx \bar{t}_i = \sum_{J=1}^{dN} \Phi_{iJ}(\mathbf{x}) T_J \quad , \mathbf{x} \in \partial V \tag{3.6}$$

where we have used the same interpolating functions in (3.6) and (3.4). Throughout the domain volume V we define the elements of the stress tensor in terms of the nodal point displacements. For a linear elastic medium we get :

$$\tau_{ij}(\mathbf{x}) \approx \bar{\tau}_{ij}(\mathbf{x}) = \tau_{ij}[\bar{u}(\mathbf{x})] = \sum_{K=1}^{dN} U_K \tau_{ij}[\Phi_K(\mathbf{x})] \, , \mathbf{x} \in V \tag{3.7}$$

where Φ_K denotes the K^{th} column vector of the interpolation matrix Φ. With the expressions (3.4), (3.6) and (3.7) we have specified the discretized elastodynamic state $\{u_i, \tau_{ij}\}$ on the domain V in terms of a finite number of parameters; nodal point displacements throughout V and nodal point tractions on the boundary ∂V .

3.2. Algebraic equations for the discretized fields

In section 3.1 we defined a discretized elastodynamic state in terms of a finite number

of field parameters

$$U_K \ , K=1, \cdots ,dN \ , T_J \ , J=1, \cdots ,dN_b$$

N_b the number of nodal points on the boundary. We will use Galerkin's principle, which restates the problem in a weak form (Strang and Fix, 1973; Zienkiewicz, 1977) to derive a set of algebraic equations for the unknown field parameters.
Taking the inner-product of (3.1) with the vector $\Phi_L(\mathbf{x})$ and integrating over the domain V we have

$$\int_V \Phi_{iL} \{-\partial_j \tau_{ij} - \rho\omega^2 u_i - f_i\} \, dV = 0 \ , L=1, \cdots ,dN \tag{3.8}$$

Equation (3.8) is known as Galerkin's principle applied to the elastodynamic equation. The equation requires the residue of the differential equation (3.1) to be orthogonal to the real interpolating functions Φ_L in the sense of the natural functional inner-product

$$(\mathbf{f} \, . \, \mathbf{g}) = \int_V f_i g_i^* dV$$

$\mathbf{f}(\mathbf{x})$, $\mathbf{g}(\mathbf{x})$ complex valued vector fields on V and * denoting complex conjugation.
Integrating (3.8) by parts we get :

$$-\int_{\partial V} \Phi_{iL} \tau_{ij} n_j dA + \int_V \{\tau_{ij} \partial_j \Phi_{iL} - \rho\omega^2 u_i \Phi_{iL} - f_i \Phi_{iL}\} dV = 0 \ ,$$

$$L = 1, \cdots ,dN \tag{3.9}$$

Substitution of the discretized traction (3.6), the discretized stress tensor (3.7) and the discretized displacement field (3.4) into (3.9) we get :

$$-\sum_{J=1}^{dN} T_J \int_{\partial V} \Phi_{iL} \Phi_{iJ} dA + \sum_{K=1}^{dN} U_K \int_V \{\tau_{ij}[\Phi_K] \partial_j \Phi_{iL} - \rho\omega^2 \Phi_{iK} \Phi_{iL}\} dV =$$

$$\int_V f_i \Phi_{iL} dV \ , L=1,2, \cdots ,dN \tag{3.10}$$

These are the finite element equations for the elastodynamic problem; a set of algebraic equations in the unknown field parameters $U_K \ , K=1, \cdots ,dN$, and T_J, $J=1, \cdots ,dN_b$.
Using matrix notation we get :

$$-\sum_{J=1}^{dN} D_{LJ} T_J + \sum_{K=1}^{dN} (S_{LK} - \omega^2 M_{LK}) U_K = F_L \ , L=1, \cdots ,dN \tag{3.11}$$

where the static stiffness matrix $\mathbf{S}$ is defined as :

$$S_{LK} = \int_V \tau_{ij}[\Phi_K] \partial_j \Phi_{iL} dV \tag{3.12}$$

and the mass matrix $\mathbf{M}$:

$$M_{LK} = \int_V \rho \Phi_{iK} \Phi_{iL} \, dV \tag{3.13}$$

the boundary traction matrix **D** is defined :

$$D_{LJ} = \int_{\partial V} \Phi_{iL} \Phi_{iJ} \, dA \tag{3.14}$$

The frequency dependent force vector **F** is defined by :

$$F_L = \int_V \Phi_{iL} f_i \, dV \tag{3.15}$$

The structure of the matrices **S** , **M** and **D** depends on the choice of the base functions Φ_M , $M=1, \cdots, N$ involved in the approximation of the fields. In general however, because the base functions have a local support - zero valued outside a limited number of neighbouring elements - it follows from the integral expressions (3.12), $\cdots$,(3.15), that the matrices are sparse.

3.2.1. Some properties of the finite element matrices

The following properties of the matrices **S**, **M**, **D** will proof to be useful in implementations.
From the definition (3.12) it follows, that the stiffness matrix **S** is symmetric.

$$S_{KL} = \int_V \tau_{ij} [\Phi_L] \partial_j \Phi_{iK} \, dV = \int_V c_{ijpq} \partial_p \Phi_{qL} \partial_j \Phi_{iK} \, dV$$

using the symmetry properties of the stress strain tensor, $c_{ijpq} = c_{jiqp} = c_{qpji}$ (Aki and Richards, 1980), we have

$$S_{KL} = \int_V c_{qpji} \partial_j \Phi_{iK} \partial_p \Phi_{qL} \, dV = S_{LK}$$

Both **M** and **D** are symmetric and positive definite. Symmetry follows from inspection of (3.14) and (3.15).
In order to prove, that **M** is positive definite, define an inner-product on a suitable space of vector fields on V.

$$(\mathbf{f} \,.\, \mathbf{g}) = \int_V \rho(\mathbf{x}) f_i(\mathbf{x}) g_i(\mathbf{x}) \, dV$$

then we have for the interpolation $\bar{\mathbf{f}}(\mathbf{x}) = \Phi(\mathbf{x})\mathbf{F}$

$$(\bar{\mathbf{f}} \,.\, \bar{\mathbf{f}}) = \int_V \rho(\mathbf{x}) \bar{f}_i(\mathbf{x}) \bar{f}_i(\mathbf{x}) \, dV = \int_V \rho(\mathbf{x}) \| \bar{f}_i(\mathbf{x}) \|^2 \, dV \; > 0 \; , \bar{\mathbf{f}}(\mathbf{x}) \neq \mathbf{0}$$

and

$$(\bar{\mathbf{f}} \,.\, \bar{\mathbf{f}}) = (\sum_K F_K \Phi_{iK} \,.\, \sum_L F_L \Phi_{iL})$$

$$= \sum_K \sum_L \int_V \rho \Phi_{iK} \Phi_{iL} \, dV \; F_K F_L = \sum_K \sum_L \mathbf{M}_{KL} F_K F_L > 0$$

which concludes the proof for **M**.
Considering a space of vector fields on ∂V and substitution of $\rho(\mathbf{x}) = 1$, results in a similar proof for **D**.

Characteristic for the finite element method is the fact, that the matrices (3.12), $\cdots$,(3.15) are evaluated in a matrix assembly procedure, that sums the contributions of the finite elements to the corresponding integrals for the matrix elements. Thus, the stiffness matrix (3.12) is assembled using

$$S_{LK} = \int_V \tau_{ij} [\Phi_K] \partial_j \Phi_{iL} \, dV = \sum_{e=1}^{N_e} \int_{V_e} \tau_{ij} [\Phi_K] \partial_j \Phi_{iL} \, dV$$

where N_e is the number of finite elements in the domain, V_e a finite element.
For the evaluation of the finite element matrices, standard software is available, see (Desai and Abel, 1972) and (Zienkiewicz, 1977) for examples and Fortran source listings. We have used a package of general purpose finite element subroutines (Segal, 1981) for the implementation of the finite element part of the present hybrid method.

3.3. Boundary conditions

In order to obtain a unique solution of the equation (3.1) suitable boundary conditions must be specified on the boundary V, (Courant and Hilbert, 1968). A similar situation occurs when we discretize the solution as in section 3.1 and formulate a discrete solution in terms of a system of linear equations (3.11).
There are $d(N+N_b)$ unknowns in the system (3.11) and only dN equations, so the system is underdetermined and we have to specify boundary conditions to obtain a unique solution. Two easily implementable types of boundary conditions are available; zero boundary traction

$$t_i(\mathbf{x}) = 0 \;\; , i=1,2,3 \; , \mathbf{x} \in \partial V \tag{3.16}$$

or zero boundary displacement,

$$u_i(\mathbf{x}) = 0 \;\; , i=1,2,3 \; , \mathbf{x} \in \partial V \tag{3.17}$$

(3.16,17) correspond to the homogeneous Neumann and Dirichlet conditions in potential theory.
In case we specify zero traction on the boundary ∂V the traction terms in (3.11) vanish and we have a system of dN equations in the dN nodal point displacements, which can

be solved in principle. For the zero displacements condition we may use an indirect argument, here the total number of unknown displacements in the discretized problem is $d(N-N_b)$ and we can construct a solution within a subspace $\mathbf{B}_0{}^h \subset \mathbf{B}^h$ using only those $N-N_b$ functions $\mathbf{\Phi}_L \in \mathbf{B}^h$ that are zero on the boundary ∂V, see appendix A. Applying Galerkin's principle to the subspace $\mathbf{B}_0{}^h$, the boundary traction term will again vanish from equation (3.11), this time because the matrix $\mathbf{D}$ is zero, as follows from the definition (3.14). We now have a system of $N-N_b$ equations in just as many unknowns, which can be solved numerically.

In many practical situations neither one of the homogeneous boundary conditions (3.16) or (3.17) corresponds to the actual physical conditions. If, for instance, we want to model wave propagation in a infinite space we will have to limit the domain V because of computer limitations. This introduces an artificial boundary ∂V on which boundary conditions must be prescribed, which are however generally unknown. When conditions (3.16) or (3.17) are applied in this problem the artificial boundary will produce "unphysical" boundary effects in the form of reflected and diffracted waves. Several methods have been proposed to reduce these artificial waves, see for instance (Smith, 1974) and (Reynolds, 1978) but none of these methods is entirely satisfactory. We will follow a different approach and supply a complete description of the field outside a bounded volume V using a boundary integral equation on ∂V in chapter 4. Matching the integral equation to the finite element equations derived in section 3.2 will result in a full system of equations in chapter 5.

Chapter 4

INTEGRAL REPRESENTATIONS FOR THE WAVE FIELD

In the present hybrid method we use an additional description of the wave field outside the bounded region V, an integral representation for the field in the region V_∞–V, where V_∞ is the background medium. This integral representation accounts for the influence of the background medium on the wave field. The integral equation derived from the integral representation results - after discretization - in an underdetermined system of linear algebraic equations. Combining these equations with the finite element equations derived in chapter 3 will result in a full system of linear algebraic equations.
However it can be shown, that the description of the field with the type of integral equation used leads to non-unique solutions for certain characteristic frequencies (Copley, 1968; Schenck, 1968; Colton and Kress, 1983a), (see appendix C). Following Schenck (1968) and Tobocman (1984), null field equations are supplemented to the integral equation, to overcome these problems. After adding these supplementary equations, we end up with an overdetermined system, that can be solved numerically. An efficient solution scheme for this extended set of integral equations combined with the finite element equations is derived in chapter 5.
Previous work on hybrid methods, combining a discretization approaches with a boundary integral representation techniques has been reported by several authors. Olson and Hwang (1971) combined an integral equation and a finite difference approach to model water waves in a harbour basin. Similar problems are treated by Berkhoff (1974, 1976) who combines an integral representation and a finite element approach. A formulation for general field problems, with a hybrid approach, combining a finite elements and a boundary integral representation, was proposed by Zienkiewicz et al. (1977) and by Wilton (1978), who applied it to problems of single frequency scattering in fluids, with an elastic wave scatterer. Shtivelman (1984, 1985) derived a method in which the wave field was set up in a bounded irregular region using a finite difference formulation. The field obtained on the boundary of the irregular region was then propagated into the exterior domain using a boundary integral representation. Shtivelman's work was limited to 2-D scalar wave propagation problems in homogeneous or weakly inhomogeneous background media. A similar method for the 2-D elastodynamic case and homogeneous background media was reported by Kummer et al. (1987). The wave propagation problem in the methods of Shtivelman and Kummer is split up in decoupled problems for the bounded inclusion and its exterior. These methods do not include multiple interactions between the bounded irregularity treated with the finite difference method and its exterior.
Investigations of integral equations in elastodynamic problems are described by Kupradze (1956, 1963), De Hoop (1958), Sharma (1967) and Tan (1975a). A rigorous

treatment of integral equations for the acoustic problem is given by Colton and Kress (1983a). Computational results are given by Banaugh and Goldsmith (1963) for acoustic wave scattering and Wong and Jennings (1975), who used a similar integral equation in a seismological modeling problem - for the special case of SH polarization - to study the effect of topography in the free surface of a halfspace on incident waves. Tan (1975a,b) used a set of coupled integral equations, to study wave diffraction in homogeneous media with homogeneous obstacles. Schuster (1984) discusses several types of integral equations for the acoustic case, applied to seismic modeling problems.
The rest of this chapter, is divided as follows; the formalism for the 3-D elastodynamic case is derived in sections 4.1-4.3. In section 4.4 we derive in greater detail the equation for the 2-D scalar case.

4.1. Introduction of the boundary integral representation

The boundary integral equation to be used here is derived from Betti's theorem, the equivalent of Green's theorem in potential theory (Kupradze, 1963). A derivation of the representation theorem and the resulting integral equations is given in appendix B. The integral representation for the wave field excited by a body force field $\mathbf{f}(\mathbf{x})$ is (see appendix B)

$$\oint_{\partial V} (u_i \tau_{ij}^k - u_i^k \tau_{ij}) n_j \, dA + \int_{V_\infty - V} f_i u_i^k \, dV = \begin{cases} 0 & , \ \mathbf{x}_p \in V \\ c_i^k(\mathbf{x}_p) u_i(\mathbf{x}_p) & , \ \mathbf{x}_p \in \partial V \\ u_k(\mathbf{x}_p) & , \ \mathbf{x}_p \in V_\infty - V \end{cases} \quad (4.1a,b,c)$$

where $\{u_i, \tau_{ij}\}$ corresponds to the unknown wave field and $\{u_i^k(\mathbf{x},\mathbf{x}_p), \tau_{ij}^k(\mathbf{x},\mathbf{x}_p)\}$ is the Green's state - the wave field generated by a point force in the x_k direction, situated in $\mathbf{x}_p$. The point $\mathbf{x}_p$ is a singular point of the Green's state and in case $\mathbf{x}_p \in \partial V$, the surface integral is understood to be the Cauchy principal value for the singular point, denoted by a bar in the integral sign. In section 4.2 the numerical evaluation of the boundary integral and the treatment of the singular point $\mathbf{x}_p$ is discussed. The tensor $c_i^k(\mathbf{x}_p)$ is defined in appendix B. In (4.1) the wave field excited by a body force field is given. An alternative expression can be derived for the case of excitation by an incident wave field. In that case we define the total field to be the sum of an undisturbed field $\mathbf{u}^0$ - that would be observed in the absence of scattering obstacles - and a scattered field $\mathbf{u}^{sc}$, $\mathbf{u}=\mathbf{u}^0+\mathbf{u}^{sc}$. The integral equation then becomes (see appendix B)

$$\oint_{\partial V} (u_i \tau_{ij}^k - u_i^k \tau_{ij}) n_j \, dA = \begin{cases} u_k^{sc}(\mathbf{x}_p) & , \ \mathbf{x}_p \in V_\infty - V \\ c_i^k(\mathbf{x}_p) u_i(\mathbf{x}_p) - u_k^0(\mathbf{x}_p) & , \ \mathbf{x}_p \in \partial V \\ -u_k^0(\mathbf{x}_p) & , \ \mathbf{x}_p \in V \end{cases} \quad (4.2a,b,c)$$

(4.1b) and (4.2b) represent inhomogeneous integral equations for the unknown total field $\{u_i, \tau_{ij}\}$ on the boundary ∂V. (4.1a) and (4.2c), for interior evaluation points

$\mathbf{x}_p \in V$ are the null field equations. Once the field on the boundary is known, the field in the interior can be calculated using (4.1c) or (4.2a).
Two special cases of (4.2) can be distinguished with homogeneous boundary conditions of either Dirichlet type;

$$u_i(\mathbf{x}) = 0 \quad , i=1,2,3 \quad , \mathbf{x} \in \partial V \tag{4.3a}$$

representing a rigid obstacle, or of Neumann type;

$$\tau_{ij}(\mathbf{x}) n_j = t_i(\mathbf{x}) = 0 \quad , i=1,2,3 \quad , \mathbf{x} \in \partial V \tag{4.3b}$$

representing a traction free obstacle such as a vacuum cavity. A half space with an indentation can be considered as a special case of a cavity reaching the free surface. In section 6.3 we present results of the calculations of the diffraction of plane waves by a canyon topography.
In appendix C it is shown that the integral equation (4.2b) has non-unique solutions for characteristic frequencies, the spectrum of internal Dirichlet eigenfrequencies of the volume V. It is shown there, that both

$$\int_{\partial V} u_i \tau_{ij}^k n_j \, dA - c_i^k(\mathbf{x}_p) u_i(\mathbf{x}_p) = 0 \tag{4.4a}$$

and

$$\int_{\partial V} u_i^k \tau_{ij} n_j \, dA = 0 \tag{4.4b}$$

have nontrivial solutions for the characteristic frequencies. This implies, that the boundary value problems (4.3a,b) do not have unique solutions for the characteristic frequencies. Another consequence is, that the combination of finite element equation (3.11) and (discretized) integral equation (4.1b),(4.2b) cannot be solved uniquely, with the solution scheme derived in chapter 5, for any of the characteristic frequencies. This limits the applicability of the integral equations to single frequency computations, and frequencies not close to one of the characteristic frequencies. The deficiency of integral equations of the type (4.1b),(4.2b), with either one of the boundary conditions (4.3a,b) is well known, (Hoenl et al., 1961; Copley, 1968; Schenck, 1968; Colton and Kress, 1983a), see appendix C. Several solutions for the non-uniqueness problem have been proposed. Schenck (1968) applies the null field equations (4.1a),(4.2a) for the interior of the volume V. It can be shown (appendix C), that for both the boundary value problems of (4.3a,b) we obtain a set of equations with a unique solution if we combine the null field equations with the integral equations (4.1b),(4.2b). Schenck applied this method to acoustic radiation problems, for a range of frequencies. In (Bolomey and Tabbara, 1973) and (Tobocman, 1984), the method is applied to acoustic scattering problems. Several authors have used other integral equations, (Burton and Miller, 1973; Colton and Kress, 1983a), involving strongly singular integrals. In the present hybrid - finite element / boundary integral equation method we adopt Schenck's extended integral equation method to overcome the non uniqueness problems of the

integral operators involved. In appendix C we derive the fundamental results on which this extended integral equation approach is based.

4.2. Discretization of the integral representation

The integral expressions (4.1,2) in terms of the wave field can be transformed into linear algebraic expressions in a finite number of wave field values. To this end we discretize the boundary surface ∂V, replacing it by a grid of connected nodal points coinciding with the boundary points of the volume grid $\mathbf{G}$ discussed in chapter 3 and appendix A. Next we use an approximation of the field on the boundary, using an interpolation scheme in terms of a discrete set of field values, identical to the one applied in the derivation of the finite element equations in chapter 3, (see also appendix A).

$$u_i(\mathbf{x}) \simeq \bar{u}_i(\mathbf{x}) = \sum_J U_J \Phi_{iJ}(\mathbf{x}) \quad , \mathbf{x} \in \partial V \tag{4.5}$$

$$\tau_{ij}(\mathbf{x}) n_j = t_i(\mathbf{x}) \simeq \bar{t}_i(\mathbf{x}) = \sum_L T_L \Phi_{iL}(\mathbf{x}) \quad , \mathbf{x} \in \partial V \tag{4.6}$$

where $\mathbf{U}$ is a vector of nodal point displacement component values, as defined in (3.3) and $\mathbf{T}$ is a vector of traction component values on the boundary surface.
In the following we only consider the case of excitation by an incident wave field. The alternative case - excitation by a force field - is almost identical to the former. The interpolating expressions are substituted into the integral representation (4.2b,c), taking the evaluation point $\mathbf{x}_p$ first as a nodal point on the boundary, $\mathbf{x}_p = \mathbf{x}_I \in \mathbf{G}$, (4.2b) and second as an evaluation point of the null field equation in the interior of V, (4.2c). The contribution from the Green's stress term to the integral equation (4.2b) can be expressed directly in terms of the nodal displacement components of the boundary evaluation point $\mathbf{x}_I$.

$$c_i^k(\mathbf{x}_I) u_i(\mathbf{x}_I) = \sum_{i=1}^{3} c_i^k(\mathbf{x}_I) u_i(\mathbf{x}_I) = \sum_{i=1}^{3} c_i^k(\mathbf{x}_I) \sum_J \delta_{J\{d(I-1)+i\}} U_J$$

$$= \sum_J \sum_{i=1}^{3} c_i^k(\mathbf{x}_I)\, \delta_{J\{d(I-1)+i\}} U_J = \sum_J C_{IJ}^k U_J$$

Substitution into the integral representation (4.2b,c) we get

$$\oint_{\partial V} \tau_{ij}^k \sum_J U_J \Phi_{iJ} n_j \, dA - \oint_{\partial V} u_i^k \sum_L T_L \Phi_{iL} \, dA = \sum_J C_{IJ}^k U_J - u_k^0(\mathbf{x}_I) \ ,$$

$$I = 1, \cdots, N_b \tag{4.7a}$$

$$\int_{\partial V} \tau_{ij}^k \sum_J U_J \Phi_{iJ} n_j dA - \int_{\partial V} u_i^k \sum_L T_L \Phi_{iL} dA = -u_k^0(\mathbf{x}_I) \ ,$$

$$I = N_b+1, \cdots, N_b+N_s \qquad (4.7b)$$

$$\sum_J U_J \{ \int_{\partial V} \tau_{ij}^k n_j \Phi_{iJ} dA - C_{IJ}^k \} - \sum_L T_L \int_{\partial V} u_i^k \Phi_{iL} dA = E_I^k \ ,$$

$$I = 1, \cdots, N_b \qquad (4.8a)$$

$$\sum_J U_J \int_{\partial V} \tau_{ij}^k n_j \Phi_{iJ} dA - \sum_L T_L \int_{\partial V} u_i^k \Phi_{iL} dA = E_I^k \ ,$$

$$I = N_b+1, \cdots, N_b+N_s \qquad (4.8b)$$

where $k=1, \cdots, d$ in (4.7,8).
Defining

$$\bar{B}_{IJ}^k = \int_{\partial V} \tau_{ij}^k(\mathbf{x},\mathbf{x}_I) n_j \Phi_{iJ}(\mathbf{x}) dA(\mathbf{x}) \qquad (4.9)$$

$$B_{IJ}^k = \bar{B}_{IJ}^k - C_{IJ}^k \quad , I=1, \cdots, N_b \qquad (4.10a)$$

$$B_{IJ}^k = \bar{B}_{IJ}^k \quad , I=N_b+1, \cdots, N_b+N_s \qquad (4.10b)$$

$$A_{IL}^k = \int_{\partial V} u_i^k(\mathbf{x},\mathbf{x}_I) \Phi_{iL}(\mathbf{x},\mathbf{x}_I) dA(\mathbf{x}) \qquad (4.11)$$

we get a set of linear algebraic equations

$$\sum_J B_{IJ}^k - \sum_L A_{IL}^k T_L = E_I^k \quad , I=1, \cdots, N_b+N_s \qquad (4.12)$$

where $E_I^k = -u_k^0(\mathbf{x}_I)$, N_b the number of nodal points on the boundary, $J, L=1, \cdots, dN_b$, dN_b the number of elements in the vector of discrete boundary field values, d the number of components in the displacement field and N_s the number of evaluation points of the null field equation (4.2c). The system of equations (4.12) can be written schematically as,

$$\left[\mathbf{B}, -\mathbf{A}\right] \begin{bmatrix} \mathbf{U} \\ \mathbf{T} \end{bmatrix} = \mathbf{E} \qquad (4.13)$$

The identical structure of the matrices **A** and **B** is illustrated by the following equation

(showing **B** only) for the case of a 2-component displacement field ($d=2$).

$$\begin{bmatrix} B^1_{11} & B^1_{12} & . & B^1_{1\,2N_b} \\ B^2_{11} & B^2_{12} & . & B^2_{1\,2N_b} \\ . & . & . & . \\ . & . & . & . \\ B^1_{N_b 1} & B^1_{N_b 2} & . & B^1_{N_b\,2N_b} \\ B^2_{N_b 1} & B^2_{N_b 2} & . & B^2_{N_b\,2N_b} \\ . & . & . & . \\ B^2_{(N_b+N_s)1} & B^2_{(N_b+N_s)2} & . & B^2_{(N_b+N_s)\,2N_b} \end{bmatrix} \times$$

$$\times \begin{bmatrix} U_1 \\ U_2 \\ . \\ . \\ U_{2N_b-1} \\ U_{2N_b} \\ . \\ U_{2(N_b+N_s)-1} \\ U_{2(N_b+N_s)} \end{bmatrix} = \begin{bmatrix} E^1_1 \\ E^2_1 \\ . \\ . \\ E^1_{N_b} \\ E^2_{N_b} \\ . \\ E^1_{(N_b+N_s)} \\ E^2_{(N_b+N_s)} \end{bmatrix} \tag{4.14}$$

For $N_s>0$ this is an overdetermined set of equations, that can be solved for the displacement field on the free boundary ∂V.

4.3. Evaluation of the integral coefficients

In section 4.2 the integral representation (4.2) was transformed into a set of linear equations by means of a discretization of the unknown field on the boundary ∂V of the obstacle. The coefficients in the equations were expressed as boundary integrals (4.10,11)

$$B_{IJ}^{k} = \int\!\!\!\!\!\!-_{S_J} \tau_{ij}^{k}(\mathbf{x},\mathbf{x}_I)\Phi_{iJ}(\mathbf{x})n_j\,dA(\mathbf{x}) - C_{IJ}^{k} \tag{4.15}$$

$$A_{IJ}^{k} = \int\!\!\!\!\!\!-_{S_J} u_i^{k}(\mathbf{x},\mathbf{x}_I)\Phi_{iJ}(\mathbf{x})n_j\,dA(\mathbf{x}) \tag{4.16}$$

where the boundary integrals are taken over the intersection of the boundary ∂V and the limited supports of the interpolating functions ϕ_J (see appendix A), denoted by a single symbol $S_J = \partial V \cap s(\phi_J)$.
For $\mathbf{x}_I \notin S_J$ the integrands are non singular and we have

$$B_{IJ}^{k} = \int_{S_J} \tau_{ij}^{k}(\mathbf{x},\mathbf{x}_I)\Phi_{iJ}(\mathbf{x})n_j\,dA(\mathbf{x}) \tag{4.15a}$$

$$A_{IJ}^{k} = \int_{S_J} u_i^{k}(\mathbf{x},\mathbf{x}_I)\Phi_{iJ}(\mathbf{x})n_j\,dA(\mathbf{x}) \tag{4.16a}$$

For the evaluation of the integrals (4.15a), (4.16a) we have used a numerical integration scheme, since expressions for the Green's state, that can be integrated analytically in (4.15a), (4.16a) are available only for special background media. Using a numerical evaluation of the matrix coefficients we keep the formulation general and applicable to more complicated media such as layered halfspaces, for which the Green's state has to be calculated numerically.
When $\mathbf{x}_I \in S_J$ the integrands in (4.15) and (4.16) are singular, since $\mathbf{x}_I$ is the singular point of the Green's state. In order to obtain sufficient accuracy, numerical integration through the singular point should be avoided.
To this end we split up the Green's state into a singular and a regular part.

$$\{u_i^{k}, \tau_{ij}^{k}\} = \{u_i^{sk}+u_i^{rk}, \tau_{ij}^{sk}+\tau_{ij}^{rk}\} \tag{4.17}$$

The singular part will be integrated analytically, for the regular part we will use a numerical scheme.
It can be shown (Kupradze, 1963) that the actual Green's state shows the same singular behaviour as the Green's state of a homogeneous space with the material parameters of the singular point. Therefore we use the Green's state for a homogeneous space for the singular part $\{u_i^{sk}, \tau_{ij}^{sk}\}$ in (4.17). The regular part can be calculated as the difference of the actual Green's state and the singular part. The regular part is integrated numerically over the boundary segments. Applying a quadrature formula, that uses only internal evaluation points (like the Gauss type integration formulae (Ralston, 1965)) we avoid the singularities located in the boundary grid points. In the implementation of the

formulae we have applied Gauss-Legendre quadrature.

4.3.1. Coefficients involving the Green's stress tensor

Substituting (4.17) into (4.15), we have

$$B_{IJ}^k = \oint_{S_J} \Phi_{iJ}(\tau_{ij}^{sk} + \tau_{ij}^{rk}) n_j \, dA - C_{IJ}^k$$

$$= \oint_{S_J} \Phi_{iJ} \tau_{ij}^{sk} n_j \, dA - C_{IJ}^k + \oint_{S_J} \Phi_{iJ} \tau_{ij}^{rk} n_j \, dA \qquad (4.18)$$

where the first integral in (4.18) denotes the Cauchy principle value. The second term is the contribution from the singular point $\mathbf{x}_I$ (see appendix B) , the term C_{IJ}^k is treated further in section 4.3.1.1.
Substituting

$$\int_{S_J} \Phi_{iJ} \tau_{ij}^{rk} n_j \, dA = \oint_{S_J} \Phi_{iJ} \tau_{ij}^{rk} n_j \, dA$$

into (4.18) we have

$$B_{IJ}^k = \oint_{S_J} \Phi_{iJ} \tau_{ij}^{sk} - C_{IJ}^k + \int_{S_J} \Phi_{iJ}(\tau_{ij}^k - \tau_{ij}^{sk}) n_j \, dA \quad , \mathbf{x}_I \in S_J \qquad (4.19)$$

The first term in (4.19) should be evaluated analytically, (see section 4.4.4 for a treatment of the 2-D scalar case). The third term can be evaluated numerically. The evaluation of the second term is discussed below in section 4.3.1.1

4.3.1.1. The contribution from the singular point

The term

$$C_{IJ}^k = \sum_{i=1}^{3} c_i^k(\mathbf{x}_I) \sum_J \delta_{J\{d(I-1)+i\}}$$

in (4.19) represents the contribution from the singularity in the Green stress to the

boundary integral (4.15). When the boundary is smooth in $\mathbf{x}_I$ it can be shown, that $c_i^k(\mathbf{x}_I) = 1/2\ \delta_{ik}$ (Kupradze, 1963).
However, models built up from grid points connected by straight lines will not be smooth in the boundary grid points. To evaluate the integral equation in the boundary grid points an expression for the contribution from the singular point $\mathbf{x}_I$ for a non smooth boundary is required. For scalar waves described by the Helmholtz equation it can be shown (Kupradze, 1956) that

$$c(\mathbf{x}_I) = \begin{cases} \dfrac{\Omega(\mathbf{x}_I)}{4\pi}, & \text{(3-D)} \\ \dfrac{\Gamma(\mathbf{x}_I)}{2\pi}, & \text{(2-D)} \end{cases} \tag{4.20}$$

where $\Omega(\mathbf{x}_I)$ is the solid angle extended by the boundary surface in the point $\mathbf{x}_I$, $\Gamma(\mathbf{x}_I)$ is the angle extended by the boundary contour in the 2-D case. In both the 2-D and the 3-D case we get $c(\mathbf{x}_I) = 1/2$ for a locally smooth boundary. For the elastodynamic case no simple relations as in (4.20) exist. Here we may use an indirect method to calculate the term $c_i^k(\mathbf{x}_I)$ discussed in appendix B.1.

4.3.2. Coefficients involving the Green's displacement tensor

For the terms in the Green's displacement we get, when $\mathbf{x}_i \in S_J$, where S_J is the cross section $S_J = \partial V \cap s(\phi_J)$ and $s(\phi_J)$ is the support of ϕ_J.

$$A_{IJ}^k = \int_{S_J} \Phi_{iJ} u_i^k dA = \int_{S_J} \Phi_{iJ} u_i^{sk} dA + \int_{S_J} \Phi_{iJ} (u_i^k - u_i^{sk}) dA \tag{4.21}$$

The contribution from the singular point in the Green's displacement can be shown to be zero (Kupradze, 1963). The first term in (4.21) should be evaluated analytically, the second term can be evaluated numerically using Gauss quadrature.

4.3.3. Range of applicability

At this point we can define a range of possible models, for which the integral representations, combined with the evaluation scheme presented in section 4.3.1,2 are applicable. In section 4.3.1,2 it was shown, that the boundary integral involved in the integral equation can be evaluated with a mixed scheme of numerical and analytical quadrature.

The numerical part of this scheme requires the values of the Green's state in tabular (non-analytic) form. Analytical forms of the Green's state occur in the analytical part of the integration scheme - the first term in (4.19) and (4.18) - and it was mentioned in 4.3.1,2, that this analytical part can be expressed as an integral of the singular Green's state for a homogeneous medium. It follows, that the Green's state for the actual medium is required in tabular form only, so that the formalism is applicable to any medium for which the Green's state can be computed numerically. Horizontally layered media, or media built up from concentric spherical shells are the most important examples of applicable models, in seismology. To compute the Green's state for such models numerically one could use a reflectivity matrix formalism (Kennett, 1983) or a mode summation approach (Harvey, 1981; Bastians, 1986)

4.4. Equations for scalar (SH) waves in two dimensions

In this section we discuss in detail the calculation of the coefficients of the algebraic equation (4.12), corresponding to the discretized integral equation (4.2b). The discussion is limited to the case of scalar waves in two dimensions. In section 4.3.3 it was argued, that the results of 4.3.1,2 are valid for elastic media, for which the Green's state can be computed numerically. The same arguments used in 4.3.3 will apply to the 2-D scalar case. As a result the formalism derived in this section will be applicable to those 2-D media, for which the scalar Green's state can be computed numerically. The singular integrals occurring in the discretized integral equations can be treated, dealing only with the singular scalar Green's state of a homogeneous medium, for which simple analytic expressions exist. Analytic expressions will be derived for the singular part of the integrals (4.18,19) in section 4.4.2.1.

4.4.1. The elastodynamic equation for a 2-D configuration

The necessary equations for the 2-D case can be derived from the ones for the general 3-D case. If we assume a 2-D configuration, i.e if both the material parameters and the wave excitation are independent of one of the coordinates, say x_3 , the equation of motion

$$-\partial_j \tau_{ij} - \rho\omega^2 u_i = f_i \tag{4.22}$$

will be invariant in the x_3 direction and so will be the solution $\{u_i, \tau_{ij}\}$. Equation (4.22) can be shown to decouple into equations for inplane (P/SV) motion and antiplane (SH) motion. Writing out equation (4.22), general conditions can be derived for the decoupling of P/SV and SH waves. Following (Tan,1975a) we denote indices with values 1 and 2 by greek symbols, equation (4.22) can then be written as

$$\partial_\beta \tau_{\alpha\beta} + \partial_3 \tau_{\alpha 3} + \rho\omega^2 u_\alpha = -f_\alpha$$

$$\partial_\beta \tau_{3\beta} + \partial_3 \tau_{33} + \rho\omega^2 u_3 = -f_3$$

or

$$\partial_\beta(c_{\alpha\beta\gamma\delta}\partial_\gamma u_\delta + c_{\alpha\beta\gamma 3}\partial_\gamma u_3) + \partial_3(c_{\alpha 3\gamma\delta}\partial_\gamma u_\delta + c_{\alpha 3\gamma 3}\partial_\gamma u_3) + \rho\omega^2 u_\alpha = -f_\alpha \quad (4.23a)$$

$$\partial_\beta(c_{3\beta\gamma\delta}\partial_\gamma u_\delta + c_{3\beta\gamma 3}\partial_\gamma u_3) + \partial_3(c_{33\gamma\delta}\partial_\gamma u_\delta + c_{33\gamma 3}\partial_\gamma u_3) + \rho\omega^2 u_3 = -f_3 \quad (4.23b)$$

In a 2-D configuration all partial derivatives with respect to x_3 vanish, $\partial_3 . = 0$, in that case (4.23a,b) will be decoupled if,

$$c_{\alpha\beta\gamma 3} = c_{3\beta\gamma\delta} = 0 \quad (4.24)$$

In the following we limit ourselves to linear isotropic elastic media with the constitutive relation,

$$c_{ijpq} = \lambda\delta_{ij}\delta_{pq} + \mu(\delta_{ip}\delta_{jq} + \delta_{iq}\delta_{jp}) \quad (4.25)$$

where λ and μ are the Lamé parameters. Verification - using $\alpha,\beta<3$ - shows that the relation (4.24) holds for such a medium.

For true 3-D media no separation occurs even if (4.24) holds, for in that case the solution is no longer a priori invariant in x_3 , so the coupling will occur through the partial derivatives with respect to x_3 in (4.23).

In the following we will deal with 2-D linear isotropic media, for which the u_3 component is a scalar wave field, fully described by the scalar equation. Dropping the index 3 and noting, that the values of the remaining indices are restricted to 1 and 2, we have from (4.23b), (4.24) and (4.25)

$$-\partial_j(\mu\partial_j u) - \rho\omega^2 u = f \quad (4.26)$$

Which shows, that the particle displacement field for SH waves in two dimensions satisfies the scalar 2-D wave equation.

We will denote the Green's state for the 2-D scalar SH case:

$$\{u_3^3(\mathbf{x},\mathbf{x}_s), \tau_{3j}^3(\mathbf{x},\mathbf{x}_s)\}$$

as

$$\{G(\mathbf{x},\mathbf{x}_s), g_j(\mathbf{x},\mathbf{x}_s)\}$$

where $\mathbf{x}_s$ is the singular point of the Green's state and

$$g_j(\mathbf{x},\mathbf{x}_s) = \mu\partial_j G(\mathbf{x},\mathbf{x}_s) \quad (4.27)$$

4.4.2. The integral equation for the 2-D SH case

In appendix B the derivation of an integral equation for the elastodynamic field on the boundary of an inclusion in a 3-D configuration is given. A similar equation can be derived for scalar SH waves in 2-D configurations, from the representation theorem for 2-D scalar waves or indirectly from the 3-D expressions (Tan,1975a). This results in the integral equations

$$\oint_{\partial V} (g_j \mu - G\mu\partial_j u) n_j ds + \int_{V_\infty - V} G f dV = \begin{cases} 0 \ , & \mathbf{x}_p \in V \\ c(\mathbf{x}_p) u(\mathbf{x}_p) \ , & \mathbf{x}_p \in \partial V \\ u(\mathbf{x}_p) \ , & \mathbf{x}_p \in V_\infty - V \end{cases} \tag{4.28}$$

for the field excited by a source distribution $f(\mathbf{x})$, and

$$\oint_{\partial V} (g_j \mu - G\mu\partial_j u) n_j ds = \begin{cases} u^{sc}(\mathbf{x}_p) \ , & \mathbf{x}_p \in V \\ c(\mathbf{x}_p) u(\mathbf{x}_p) - u^0(\mathbf{x}_p) \ , & \mathbf{x}_p \in \partial V \\ -u^0(\mathbf{x}_p) \ , & \mathbf{x}_p \in V_\infty - V \end{cases} \tag{4.29}$$

for the field excited by an incident wave field $u^0(\mathbf{x})$.
In (4.28,29), ∂V is the boundary contour of the 2-D obstacle, with an normal vector $\mathbf{n}$ pointing outward from the 2-D domain V.
Equations (4.28,29) are the 2-D scalar counterparts of equations (4.1,2).

As mentioned in section 4.3.1.1 we have for the coefficients $c(\mathbf{x}_p)$ in the 2-D scalar case

$$c(\mathbf{x}_p) = \frac{\Gamma(\mathbf{x}_p)}{2\pi} \tag{4.30}$$

where $\Gamma(\mathbf{x}_p)$ is the exterior angle spanned by the boundary contour ∂V in the point $\mathbf{x}_p$.

4.4.2.1. Integral coefficients for the 2-D SH case

In section 4.3 we have discussed the discretization of the boundary integral equation for the 3-D elastodynamic case. In this section we present in more detail the equation for the 2-D scalar SH case, using the notations introduced in section 4.4.2. The counterparts of the integral coefficients (4.15,16) for the 2-D scalar case are

$$B_{IJ} = \oint_{S_J} g_j(\mathbf{x},\mathbf{x}_I) \phi_J(\mathbf{x}) n_j ds - C_{IJ} \tag{4.31}$$

$$A_{IJ} = \int_{S_J} G(\mathbf{x},\mathbf{x}_I)\phi_J(\mathbf{x})n_j\,ds \tag{4.32}$$

where the integral is taken over the cross section $S_J = \partial V \cap s(\phi_J)$. The matrix C_{IJ} in (4.31) is derived from the term $c(\mathbf{x}_p)$ in (4.28)

$$c(\mathbf{x}_I)u(\mathbf{x}_I) = \sum_J c(\mathbf{x}_I)\delta_{IJ}U_J = \sum_J C_{IJ}U_J \;\rightarrow\; C_{IJ} = c(\mathbf{x}_I)\delta_{IJ}$$

When $\mathbf{x}_I \notin S_J$ the integrands in (4.31,32) are nonsingular and we may use numerical integration to evaluate the integrals

$$B_{IJ} = \int_{S_J} g_j(\mathbf{x},\mathbf{x}_I)\phi_J(\mathbf{x})n_j\,ds - c(\mathbf{x}_I)\delta_{IJ} = \int_{S_J} g_j(\mathbf{x},\mathbf{x}_I)\phi_J(\mathbf{x})n_j\,ds \tag{4.33}$$

$$A_{IJ} = \int_{S_J} G(\mathbf{x},\mathbf{x}_I)\phi_J(\mathbf{x})n_j\,ds \tag{4.34}$$

When $\mathbf{x}_I \in S_J$ we split up the Green's state as in 4.3 into a singular part - corresponding with the Green's state of a homogeneous 2-D space - and a regular part.

$$\{G, g_j\} = \{G^s + G^r, g_j^s + g_j^r\} \tag{4.35}$$

where $\{G^s, g_j^s\}$ is the Green's state for SH waves in a homogeneous 2-D space

$$G^s(\mathbf{x},\mathbf{x}_s) = \frac{i}{4\mu}H_0^{(1)}(k\,|\,\mathbf{x}-\mathbf{x}_s\,|)$$

(Morse and Fesbach, 1953), where $H_0^{(1)}$ is the zero order Hankel function of the first kind and k is the shear wave number of the homogeneous medium, $k=\omega/\beta$, ω the radial frequency, β the shear wave velocity $\beta=\sqrt{\mu/\rho}$.

The fields in $\{G^s, g_j^s\}$ depend only on the distance between the "field point" $\mathbf{x}$, and the "source point" $\mathbf{x}_s$. In the following a single notation is used for the functions describing the 2-D fields and their 1-D representation.

$$\{G^s(\mathbf{x},\mathbf{x}_s), g_j(\mathbf{x},\mathbf{x}_s)\} = \{G^s(|\,\mathbf{x}-\mathbf{x}_s\,|), g_j(|\,\mathbf{x},\mathbf{x}_s\,|)\}$$

4.4.2.1.1. Coefficients involving the Green's stress

Substitution of (4.35) into (4.31) gives

$$B_{IJ} = \int_{S_J} g_j^s(\mathbf{x},\mathbf{x}_I)\phi_J(\mathbf{x})n_j\,ds - c(\mathbf{x}_I)\delta_{IJ} + \int_{S_J} (g_j - g_j^s)\phi_J(\mathbf{x})n_j\,ds \tag{4.36}$$

The second integral in (4.36) can be calculated using numerical integration.
It is worth-wile mentioning two special cases here.

(1) In case the background medium is a homogeneous unbounded space, the actual Green's state will be identical to the singular part in (4.35) and the integrals of the regular part vanish.

(2) In case of a homogeneous half space, the regular part in (4.35) is the free surface reflection of the halfspace boundary, which can be easily obtained by the method of images (Morse and Fesbach,1953)

In the integration of the first integral two cases can be distinguished

$$\mathbf{x}_I = \mathbf{x}_J \tag{4.37a}$$

$$\mathbf{x}_I\ ,\ \mathbf{x}_J \textit{ are neighbouring nodal points on the boundary} \tag{4.37b}$$

Cases (4.37a,b) will be denoted by 1 and 0 respectively in the following. This refers to the fact, that the singular point $\mathbf{x}_I$ coincides either with the maximum (unit) value (4.37a) or with a zero value (4.37b) of the interpolating function ϕ_J, see figure 4.1.
In case (4.37a) the first integral in (4.36) vanishes since

$$g_j^s n_j = \mu\partial_j G^s n_j = \mu\frac{dG^s}{dR} n_j \partial_j R = 0\ ,\ \mathbf{x}\neq\mathbf{x}_I \tag{4.38}$$

because $\partial_j R n_j = \partial_n R = \partial_n |\mathbf{x}-\mathbf{x}_I| = 0$ along both straight line segments of S_J. In case (4.37b) the singular point coincides with a zero value of the interpolating function ϕ_J, see figure 4.1. Then the contribution to the first integral in (4.36) from the line segment, that contains $\mathbf{x}_I$ again vanishes because of (4.38), but the the other segment will generally give a finite contribution, when $n_j\partial_j R \neq 0$.
This last nonzero contribution from one of the line segments can be evaluated numerically, because the integrand is non singular.

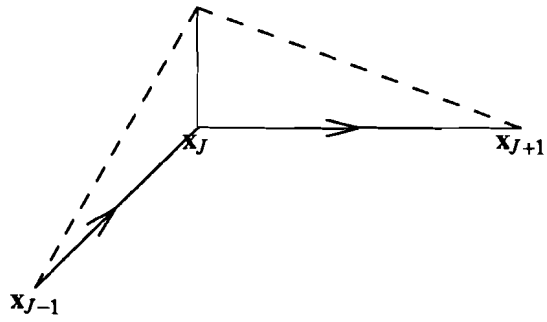

figure 4.1 A piecewise interpolating function $\phi_J(\mathbf{x})$ (dashed line) and the cross section S_J of its support with the boundary (line connecting $\mathbf{x}_{J-1}$,$\mathbf{x}_J$ and $\mathbf{x}_{J+1}$)

4.4.2.1.2. Coefficients involving the Green's displacement

The integral of the Green's displacement (4.32) is - after splitting up the Green's state according to (4.35)

$$A_{IJ} = \int_{S_J} G^s(\mathbf{x},\mathbf{x}_I)\phi_J(\mathbf{x})ds + \int_{S_J} \{G(\mathbf{x},\mathbf{x}_I) - G^s(\mathbf{x},\mathbf{x}_I)\}\phi_J(\mathbf{x})ds$$

$$= A_{IJ}^{(i)} + A_{IJ}^{n} \quad , i=1,0 \tag{4.39}$$

The first integral in (4.39) $A_{IJ}^{(i)}$ contains a singular integrand and will be evaluated analytically below. The second integral A_{IJ}^{n} can be evaluated numerically. In the analytical evaluation of the first term of (4.39) we distinguish as before the two cases (4.37a,b), denoted by $i=1$ resp. $i=0$, where the interpolating functions ϕ_J have a value of one respectively zero in the singular point $\mathbf{x}_I$ (see figure 4.1).

a) $\mathbf{x}_J = \mathbf{x}_I$, $\phi_J(\mathbf{x}_I) = 1$ In this case the first term of (4.39) is

$$A_{II}^{(1)} = \int_{\mathbf{x}_{I-1}}^{\mathbf{x}_I} G^s(\mathbf{x},\mathbf{z}_I)\phi_I(\mathbf{x})ds + \int_{\mathbf{x}_I}^{\mathbf{x}_{I+1}} G^s(\mathbf{x},\mathbf{z}_I)\phi_I(\mathbf{x})ds$$

$$= \int_0^{h_{I-1,I}} G^s(t)(1-\frac{t}{h_{I-1,I}})dt + \int_0^{h_{I,I+1}} G^s(t)(1-\frac{t}{h_{I,I+1}})dt \qquad (4.40)$$

where $h_{K,L} = |\mathbf{x}_L - \mathbf{x}_K|$.

b) $\mathbf{x}_I$ and $\mathbf{x}_J$ are neighbouring points, $\phi_J(\mathbf{x}_I) = 0$. Here the line segment, that does not contain the singular point $\mathbf{x}_I$ will give a contribution $A_{IJ}^{(0)n}$, to the integral $A_{IJ}^{(0)}$, that can be evaluated numerically. The contribution $A_{IJ}^{(0)a}$ of the segment, that contains the singularity will be evaluated analytically below.
Suppose $\mathbf{x}_I$ is on the second segment of S_J , i.e $I=J+1$, we then have to evaluate the integral

$$A_{IJ}^{(0)a} = \int_0^{h_{I,I+1}} G^s(t)\frac{t}{h_{I,I+1}}dt \qquad (4.41)$$

Two types of integrals occur in (4.40,41)

$$I_1 = \int_0^h G^s(t)dt \quad , \quad I_2 = \int_0^h \frac{t}{h}G^s(t)dt \qquad (4.42a,b)$$

inserting the explicit form of the Green's function for a homogeneous 2-D space into (4.42a,b) we get

$$I_1(k,h) = \frac{i}{4\mu}\int_0^h H_0^{(1)}(kt)dt \quad , \quad I_2(k,h) = \frac{i}{4\mu}\int_0^h H_0^{(1)}(kt)\frac{t}{h}dt \qquad (4.43a,b)$$

The integral (4.43a) can be expressed in terms of Hankel functions and Struve functions, (Abramowitz and Stegun,1964 11.1.7).

$$I_1(k,h) = \frac{i}{4\mu k}\int_0^h H_0^{(1)}(kt)dt$$

$$= \frac{ih}{4\mu k}[H_0^{(1)}(kh) + \frac{\pi}{2}\{\mathbf{H}_0(kh)H_1^{(1)}(kh) - \mathbf{H}_1(kh)H_0^{(1)}(kh)\}] \qquad (4.44)$$

The Struve functions $\mathbf{H}_\nu(z)$ of order ν can be evaluated using a series expansion, (Abromowitz and Stegun,1964 12.1.3).
The integral in (4.43b) can be expressed in terms of Hankel functions, (Abramowitz and Stegun,1970 11.3.30,11.3.24).

$$I_2(k,h) = \frac{i}{4\mu k}\int_0^h \frac{t}{h} H_0^{(1)}(kt)dt$$

$$= \frac{i}{4\mu hk^2}\int_0^{kh} \nu H_0^{(1)}(\nu)d\nu = \frac{i}{4\mu k}\{H_1^{(1)}(kh) + i\frac{2}{\pi kh}\} \qquad (4.45)$$

Substituting (4.44) and (4.45) in (4.41) and (4.40) we get

$$A_{IJ}^{(1)} = I_1(k, h_{I-1,I}) + I_1(k, h_{I,I+1}) - I_2(k, h_{I-1,I}) - I_2(k, h_{I,I+1}) \qquad (4.46a)$$

$$A_{IJ}^{(0)a} = I_1(k, h_{I-1,I}) + I_1(k, h_{I,I+1}) - I_2(k, h_{I-1,I}) - I_2(k, h_{I,I+1}) \qquad (4.46b)$$

figure 4.2 shows a plot of the contribution from a single boundary line segment to the singular integrals (4.44,45) as a function of $\frac{kh}{2\pi}$.

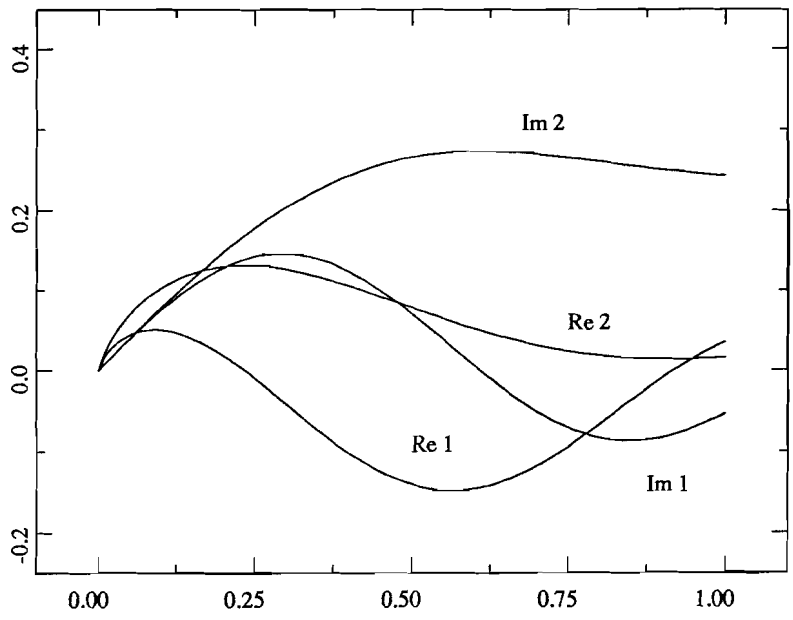

figure 4.2 Real and imaginary parts of the singular integrals I_1 and I_2 (vertical) plotted against $kh/(2\pi)$ (horizontal).

Chapter 5

COUPLED FINITE ELEMENT / BOUNDARY INTEGRAL EQUATIONS

In chapter 3 we have derived a set of linear algebraic finite element equations for the displacement field in a finite volume V and the traction field on its boundary ∂V, (3.11). In chapter 4 a set of linear algebraic equations for both the displacement and the traction field on the boundary ∂V, (4.12) was derived from the discretization of a boundary integral representation. Both the finite element equation and the discretized integral equation are generally underdetermined. However, combining both sets of equations results in a full system, in the unknown field variables. Adding the null field equations will make the resultant set an overdetermined system. The dimensions of the resulting matrix will in practice be large. Assuming a total of N nodal points in the finite element grid, with d unknown displacement components per point, and N_b nodal points on the boundary, with d unknown traction values per boundary point, we have $d(N+N_b)$ unknowns. If we use N_s null field evaluation points we have a total of $d(N+N_b+N_s)$ equations In order to economize the numerical solution procedure of the algebraic equations, we make use of the special structure of the matrix, to derive a new set of equations, with a considerably smaller matrix. A similar approach of matrix reduction is followed in (Berkhoff, 1974; Zienkiewicz et al., 1977; Wilton, 1978).

5.1. A solution scheme for the coupled equations

The finite element equation (3.11) derived in chapter 3 is

$$\sum_K (S_{LK} - \omega^2 M_{LK}) U_K - \sum_J D_{LJ} T_J = F_L \quad , L=1, \cdots, dN \tag{5.1}$$

The discretized integral representation (4.12) for the wave field excited by an incident wave is

$$\sum_{J=1}^{dN_b} B_{IJ}^k U_J - \sum_{L=1}^{dN_b} A_{IL}^k T_L = E_I^k \quad , I=1, \cdots, N_b+N_s \ , \ k=1, \cdots, d \tag{5.2}$$

where N_b is the number of boundary points, N_s the number of null field evaluation

points.
In the following, an abbreviated notation for the dynamic stiffness matrix will be used

$$\mathbf{Z} = \mathbf{S} - \omega^2\mathbf{M} \tag{5.3}$$

Next we partition the vector of unknown quantities

$$(\mathbf{U},\mathbf{T})^T = (\mathbf{U}_I,\mathbf{U}_R,\mathbf{T})^T \tag{5.4}$$

where $\mathbf{U}_I$ is a vector of displacement components of the N_i internal grid points, ($N_b+N_i=N$, the total number of grid points). $\mathbf{T}$ is the vector of traction component values.
Substitution of (5.4) into (5.1) and (5.2) results in:

$$\begin{bmatrix} \mathbf{Z}_{II} & , \mathbf{Z}_{IR} & , \mathbf{0} \\ \mathbf{Z}_{RI} & , \mathbf{Z}_{RR} & , -\mathbf{D} \\ \mathbf{0} & , \mathbf{B} & , -\mathbf{A} \end{bmatrix} \begin{bmatrix} \mathbf{U}_I \\ \mathbf{U}_R \\ \mathbf{T} \end{bmatrix} = \begin{bmatrix} \mathbf{F}_I \\ \mathbf{F}_R \\ \mathbf{E} \end{bmatrix} \tag{5.5}$$

The matrix $\mathbf{Z}$ and the right hand side vector $\mathbf{F}$ in (5.1) have been partitioned according to (5.4). With $n = d(N+N_b+N_s)$ equation (5.5) is a set of n linear algebraic equations in $d(N+N_b)$ unknown field values. For $N_s>0$ the system is overdetermined.
A standard solution of the equations in (5.5), using the full complex matrix would require $2n^2$ locations of computer memory. Supposing $N_s \ll N$ and $n \approx 10^3$, it will take $\approx 2\times10^6$ memory locations to store the matrix.
The number of arithmetic operations required for the solution of the complete system (5.5) depends even stronger on the dimension of the matrix n , $O(n^3)$ versus $O(n^2)$ for the memory requirement.

In order to reduce both the amount of memory and the computation time needed for the solution of (5.5) an alternative solution scheme is used, that exploits the special structure of the matrix in (5.5).
$\mathbf{A}$ and $\mathbf{B}$ are full matrices, whereas the partitions of $\mathbf{Z}$ are sparse. Solving $\mathbf{U}_I$ from the first row of (5.5) we get,

$$\mathbf{U}_I = \mathbf{Z}_{II}^{-1}(\mathbf{F}_I - \mathbf{Z}_{IR}\,\mathbf{U}_R) \tag{5.6}$$

Substituting (5.6) into (5.5) we can express the traction value vector $\mathbf{T}$ as

$$\mathbf{T} = -\mathbf{D}^{-1}(\mathbf{F}_R - \mathbf{Z}_{RI}\,\mathbf{Z}_{II}^{-1}(\mathbf{F}_I - \mathbf{Z}_{IR}\,U_R) - \mathbf{Z}_{RR}\,\mathbf{U}_R)$$

Defining

$$\mathbf{W} = \mathbf{Z}_{RR} - \mathbf{Z}_{RI}\,\mathbf{Z}_{II}^{-1}\mathbf{Z}_{IR}$$

we get

$$\mathbf{T} = \mathbf{D}^{-1}\mathbf{W}\mathbf{U}_R - \mathbf{D}^{-1}(\mathbf{F}_R - \mathbf{Z}_{RI}\,\mathbf{Z}_{II}^{-1}\mathbf{F}_I) \tag{5.7}$$

Substitution of (5.7) into (5.5) finally results in

$$(\mathbf{B} - \mathbf{A}\mathbf{D}^{-1}\mathbf{W})\mathbf{U}_R = \mathbf{E} + \mathbf{A}\mathbf{D}^{-1}(\mathbf{Z}_{RI}\,\mathbf{Z}_{II}^{-1}\mathbf{F}_I - \mathbf{F}_R) \tag{5.8}$$

The matrix in (5.8) is now $d(N_b+N_s)\times dN_b$, whereas the original matrix in (5.5) is $d(N+N_b+N_s)\times d(N+N_b)$.

In general the dimensions of the matrix will be reduced considerably using the reduction scheme leading from (5.5) to (5.8).
The matrix $\mathbf{Z}$ is sparse and symmetric, $\mathbf{Z}_{II}$ may be stored as a band matrix i.e. $(Z_{II})_{IJ} = 0$, $|I-J| > m$, $2m+1$ the bandwidth (Zienkiewicz, 1977). Furthermore $\mathbf{Z}_{IR} = \mathbf{Z}_{RI}^T$.
In the computation of the matrix $\mathbf{W}$ the explicit inversion of $\mathbf{Z}_{II}$ should be avoided (this would lead to a full matrix), instead $\mathbf{W}$ can be computed column wise with the K^{th} column given by

$$\mathbf{W}^K = \mathbf{Z}_{RR}^K - \mathbf{Z}_{RI}\mathbf{X}^K \quad , K=1, \cdots, dN_b \tag{5.9}$$

$$\mathbf{X}^K = \mathbf{Z}_{II}^{-1}\mathbf{Z}_{IR}^K \quad , K=1, \cdots, dN_b \tag{5.10}$$

where $\mathbf{Z}_{RR}^K$ and $\mathbf{Z}_{IR}^K$ are the K^{th} column of $\mathbf{Z}_{RR}$ and $\mathbf{Z}_{IR}$ respectively.
The vector $\mathbf{X}^K$ is obtained solving the equation

$$\mathbf{Z}_{II}\mathbf{X}^K = \mathbf{Z}_{IR}^K \tag{5.11}$$

The advantage of this scheme is, that in order to solve for the dN_b vectors $\mathbf{X}^K$ the band matrix $\mathbf{Z}_{II}$ can be decomposed or reduced to triangular form in place, (without losing its band structure). Furthermore this decomposition has to be performed only once for every frequency ω. Once the matrix decomposition is available the vectors $\mathbf{X}^K, K=1, \cdots, N_b$ can be computed using the same decomposition (Wilkinson, 1965).
The dynamic stiffness matrix $\mathbf{Z}_{II}$ becomes singular for a spectrum of real frequencies ω_j , $j=1, \cdots, N_i$, the eigenvalues of the generalized eigenvalue problem

$$\mathbf{Z}_{II}\mathbf{x} = (\mathbf{S} - \omega^2\mathbf{M}_{II})\mathbf{x} = \mathbf{0} \tag{5.12}$$

This follows from the symmetry of $\mathbf{S}_{II}$ and $\mathbf{M}_{II}$ and the fact, that $\mathbf{M}_{II}$ is positive definite (section 3.2.1), (Wilkinson, 1965).
In order to avoid numerical problems connected with the singular frequencies of $\mathbf{Z}_{II}$ we have introduced damping in the model, (Aki and Richards, 1981). Using complex material parameters to model an anelastic medium, these singular frequencies move from the real ω axis into the lower half complex ω plane.
Consider a slightly anelastic medium with homogeneous damping characteristics $c'_{ijkl} = (1 + i\,\alpha)c_{ijkl}$, $|\alpha| \ll 1$, $\alpha(\mathbf{x})$ a constant.
From the definition of the stiffness matrix in chapter 3

$$S_{KL} = \int_V c_{ijpq}\,\partial_p \Phi_{ql}\,\partial_j \Phi_{iK}\,dV$$

it follows $S'_{KL} = (1+i\,\alpha)S_{KL}$.
The eigenvalue equation then becomes

$$(\mathbf{S}' - \omega'^2\mathbf{M}_{II})\mathbf{x} = \mathbf{0}$$

or

$$(\mathbf{S} - \frac{\omega'^2}{1+i\,\alpha}\mathbf{M}_{II})\mathbf{x} = \mathbf{0}$$

the eigenvalues are

$$\omega_j'^2 = \omega_j^2(1+i\,\alpha)$$

defining $\alpha = -\,sign(\omega)\,|\alpha|$ we have

$$\omega_j' = \omega_j(1 - i\ sign(\omega_j)\frac{|\alpha|}{2} + O(\alpha^2))$$

for $\omega \in \mathbf{R}$, $\alpha \in \mathbf{R}$, $|\alpha| \ll 1$ we have $\omega_j' \in \mathbf{C}_-$

It can be shown that causality requires the elasticity parameters and the quality factor $Q = \alpha^{-1}$ to be frequency dependent, (Aki and Richards, 1981). Since the present formulation is in the frequency domain, this causes no extra problems. However for small damping ($Q \approx 10^{2)}$, and limited frequencies, the effect of the frequency dependence can be neglected (Aki and Richards, 1981; Kennett, 1983). In the numerical experiments we have taken $Q = 10^2$ independent of frequency. Having moved the singularities into the lower half plane, we can integrate our results over the real frequency axis, - in the inverse Fourier transform to the time domain. In the implementation, wave field frequency spectra are computed for a range of discrete equidistant frequencies. The Fast Fourier Transform algorithm (Cooley and Tukey, 1965) is then applied to obtain the time domain results.

Using complex elasticity parameters will result in complex matrices $\mathbf{S}$, $\mathbf{Z}$ For the decomposition of the complex matrix $\mathbf{Z}_{II}$ we have used a standard Gauss elimination algorithm with partial pivoting (Stoer, 1972) for complex band matrices from the LINPACK library (Dongarra et al., 1979).

The matrix $\mathbf{D}$ in (5.8) is sparse, real, symmetric and positive definite (see chapter 3), which implies $\mathbf{D}$ is nonsingular. Since the matrix is positive definite, no pivoting is required in the numerical solution (Wilkinson, 1965) and we may economize the storage of the matrix using an equation solver for a profile matrix - a matrix with a row dependent bandwidth (Zienkiewicz, 1977). As before we do not compute $\mathbf{D}^{-1}$ explicitly, instead the matrix can be decomposed,

$$\mathbf{D} = \mathbf{L}\mathbf{Q}\mathbf{L}^T \tag{5.13}$$

with $\mathbf{L}$ a lower triangular matrix with unit diagonal, $\mathbf{Q}$ a diagonal matrix, thereby preserving the sparse nature of $\mathbf{D}$ in the matrix $\mathbf{L}$, (Wilkinson, 1965). The decomposition (5.13) has to be carried out only once in a complete program run, because $\mathbf{D}$ is independent of frequency. Once the decomposition (5.13) is available, the matrix multiplication with $\mathbf{D}^{-1}$ can be computed column wise, solving the related equation

$$\mathbf{X}^K = \mathbf{D}^{-1}\mathbf{W}^K \quad , K = 1, \cdots, dN_b$$

$$\mathbf{D}\mathbf{X}^K = \mathbf{W}^K \quad , K = 1, \cdots, dN_b \tag{5.14}$$

The solution of (5.14) is readily obtained from (5.13).

Having computed $\mathbf{D}^{-1}\mathbf{W}$ the result can be substituted in (5.8), giving a generally overdetermined system of equations in the unknown boundary displacements $\mathbf{U}_R$

$$\mathbf{C}\mathbf{U}_R = \mathbf{R} \tag{5.15}$$

with

$$\mathbf{C} = \mathbf{B} - \mathbf{A}\mathbf{D}^{-1}\mathbf{W}$$

$$\mathbf{R} = \mathbf{E} + \mathbf{A}\mathbf{D}^{-1}(\mathbf{Z}_{RI}\mathbf{Z}_{II}^{-1}\mathbf{F}_I - \mathbf{F}_R)$$

where $\mathbf{C}$ is a complex $d(N_b+N_s)\times dN_b$ matrix.
To compute a least squares solution of the overdetermined system (5.15), we have used a QR decomposition method (Wilkinson, 1965; Stoer, 1972) from the LINPACK library (Dongarra, 1979).

5.2. Computation of field values in points off the boundary

Once the field values for the boundary grid points are obtained from (5.15), values for internal grid points can be computed solving the related Dirichlet boundary value problem. From (5.6) the equation for internal field values becomes

$$\mathbf{Z}_{II}\mathbf{U}_I = \mathbf{F}_I - \mathbf{Z}_{IR}\mathbf{U}_R \tag{5.16}$$

This equation is solved in a similar manner as equation (5.11) using Gauss elimination. The components of the resulting vector $\mathbf{U}_I$ are the multiplexed field values in internal finite element grid points. When an evaluation point does not coincide with a grid point, the corresponding field value can be obtained by interpolation, using formula (3.4).

$$\bar{u}_i(\mathbf{x}) = \sum_{k=1}^{dN} U_K \Phi_{iK}(\mathbf{x}) \tag{5.17}$$

Field values for, say N_e evaluation points in the exterior domain can be computed from the boundary values, using a discretization of the integral representation (4.2a) for the scattered field.
Discretization produces the explicit form

$$\mathbf{U}^{sc} = \mathbf{B}^{(e)}\mathbf{U}_R - \mathbf{A}^{(e)}\mathbf{T}_R \tag{5.18}$$

where $\mathbf{U}^{sc}$ is the vector of N_e multiplexed scattered field values for the external evaluation points, $\mathbf{U}_R$ and $\mathbf{T}$ as defined in (5.4). Note, that the $dN_e\times dN_b$ propagation matrices $\mathbf{B}^{(e)}$ and $\mathbf{A}^{(e)}$ differ from the matrices $\mathbf{B}$ and $\mathbf{A}$ in (5.5) (see also (4.14).
The boundary traction value vector in (5.18) can also be expressed in terms of $\mathbf{U}_R$ using (5.7).
Total field values in exterior points can be computed from the results of (5.18) by adding the incident field values for the evaluation points

$$\mathbf{u}(\mathbf{x}_{ext}) = \mathbf{u}^{sc}(\mathbf{x}_{ext}) + \mathbf{u}^0(\mathbf{x}_{ext}) \tag{5.19}$$

An outline of a program package, developed as an implementation of the solution procedures discussed in this chapter is given in appendix D. Numerical results of several modeling experiments are presented in chapter 6.

Chapter 6

DIFFRACTION OF SH WAVES BY AN ANOMALY IN A HOMOGENEOUS 2-D SPACE (NUMERICAL RESULTS)

In this chapter numerical results will be presented of an implementation of the hybrid method, presented in the previous chapters.
The method has been applied to a number of diffraction problems for SH waves in a homogeneous 2-D space with an inclusion of finite extent.
In section 6.1 the problem of the diffraction of a plane wave by an obstacle with circular cross section is solved numerically using the theory of the preceding chapters. The results are compared with a series solution for the same problem.
Section 6.2 contains results for a scatterer of rectangular cross section. In section 6.3 we present results for a model of a halfspace with a canyon topography and a low velocity fill at the free surface.

6.1. Diffraction of a plane wave by a circular cylinder

Let a plane SH wave be incident on a circular cylinder of radius a and let the wave normal be perpendicular to the axis of the cylinder, resulting in a 2-D configuration (see figure 6.1).
The wave field can be found as the solution of the equation of motion (4.26) specialized for a homogeneous medium.

$$-\mu\partial_j\partial_j u - \rho\omega^2 u = f \tag{6.1}$$

In the absence of a body force field f we obtain the homogeneous Helmholtz equation

$$\nabla^2 u + k^2 u = 0 \tag{6.2}$$

where ∇^2 is the Laplace operator and k is the wave number of the medium, $k = \omega/\beta$, β is the shear wave velocity, $\beta = (\mu/\rho)^{1/2}$, μ and ρ are the rigidity and mass density. The solution of (6.2) supplemented with suitable boundary conditions (see chapter 2) can be obtained by a series solution (Eringen and Suhubi, 1975).

The total field u in the medium surrounding the cylinder is split up into an incident field u^0 and a scattered field u^{sc} as in section 4.1 $u = u^0 + u^{sc}$.

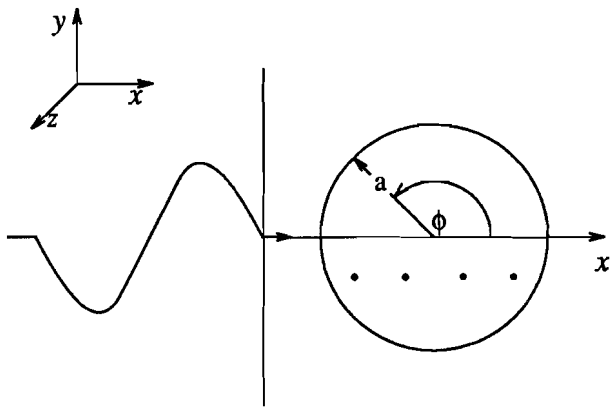

figure 6.1 Plane wave traveling parallel to the x axis, incident on a cylinder with axis parallel to the z axis. Dots in lower half circle denote one of two rows of null field evaluation points, symmetric in y.

Both fields satisfy the equation (6.2) and the scattered field u^{sc} also satisfies a radiation condition.
Using separation of variables in the cylindrical coordinates r,ϕ we get

$$u^{sc}(r,\phi) = \sum_{n=0}^{\infty} W_n H_n(kr)\cos(n\phi) \tag{6.3}$$

where the n^{th} order Hankel function of the first kind $H_n = H_n^{(1)}$, combined with the implicit time dependence $e^{-i\omega t}$ introduced by the sign convention in the Fourier transform (2.4a,b) corresponds with an outward travelling wave, as can be seen from the asymptotic expansion for large arguments (Abramowitz, 1964)

$$H_n^{(1)}(z) \sim \sqrt{2/(\pi z)}\, e^{i(z - \frac{1}{2}n\pi - \frac{1}{4}\pi)}$$

The incident field u^0 is plane wave of unit amplitude, traveling in the direction of the x axis (see figure 6.1)

$$u^0(\mathbf{x}) = e^{ikx} \quad , k=\omega/\beta$$

Using an expansion in Bessel functions (Eringen and Suhubi, 1975) we have

$$u^0(r,\phi) = \sum_{n=0}^{\infty} C_n J_n(kr)\cos(n\phi) \tag{6.4}$$

where J_n is the Bessel function of order n and $C_n = \varepsilon_n i^n$ with

$$\varepsilon_n = \begin{cases} 1 & , n=0 \\ 2 & , n>0 \end{cases}$$

In the following, quantities relating to the interior domain will be denoted by a superscript i. As for the incident wave, we may write for the total field in the interior

$$u^i(r,\phi) = \sum_{n=0}^{\infty} A_n J_n(k^i r)\cos(n\phi) \tag{6.5}$$

Applying the boundary conditions - continuity of displacement and traction - for $r=a$

$$u^0 + u^{sc} = u^i \tag{6.6a}$$

$$\mu \frac{\partial}{\partial r}(u^0 + u^{sc}) = \mu^i \frac{\partial}{\partial r} u^i \tag{6.6b}$$

to (6.3,4,5), the excitation coefficients W_n and A_n can be expressed in the coefficients C_n of the incident field

$$\begin{bmatrix} W_n \\ A_n \end{bmatrix} = \frac{C_n}{D_n} \begin{bmatrix} \rho^i \beta^i J_n'(k^i a) & , -\rho\beta J_n(k^i a) \\ \rho\beta H_n'(ka) & , -\rho\beta H_n(ka) \end{bmatrix} \begin{bmatrix} J_n(ka) \\ J_n'(ka) \end{bmatrix} \tag{6.7}$$

where J_n', H_n' denote the derivatives of the Bessel and Hankel functions and the determinant D_n is given by

$$D_n = \rho\beta H_n'(ka) J_n(k^i a) - \rho^i \beta^i J_n'(k^i a) H_n(ka) \tag{6.8}$$

The solution $W_n^{(s)}$ for the "soft" case of a hollow cylinder follows from (6.7) as the limiting case

$$\frac{\rho^i \beta^i}{\rho\beta} \to 0$$

$$W_n^{(s)} = -C_n \frac{J_n'(ka)}{H_n'(ka)} \tag{6.9}$$

From (6.7) and (6.9) it follows that the amplitudes of the diffracted wave fields depend linearly on the amplitude of the incident wave field. Writing the total field in the exterior domain corresponding to (6.9) as

$$u(r,\phi) = u^0 + u^{sc} = \sum_{n=0}^{\infty} C_n \left[J_n(kr) - \frac{J_n'(ka)}{H_n'(ka)} H_n(kr) \right] \cos(n\phi)$$

it follows that the total field amplitude also depends linearly on the incident field u^0. A similar argument can be given for the transparent boundary case. The linear dependence between the computed response and the incident wave allows a straight forward generalization of the results for a unit amplitude incident wave field presented in the following.

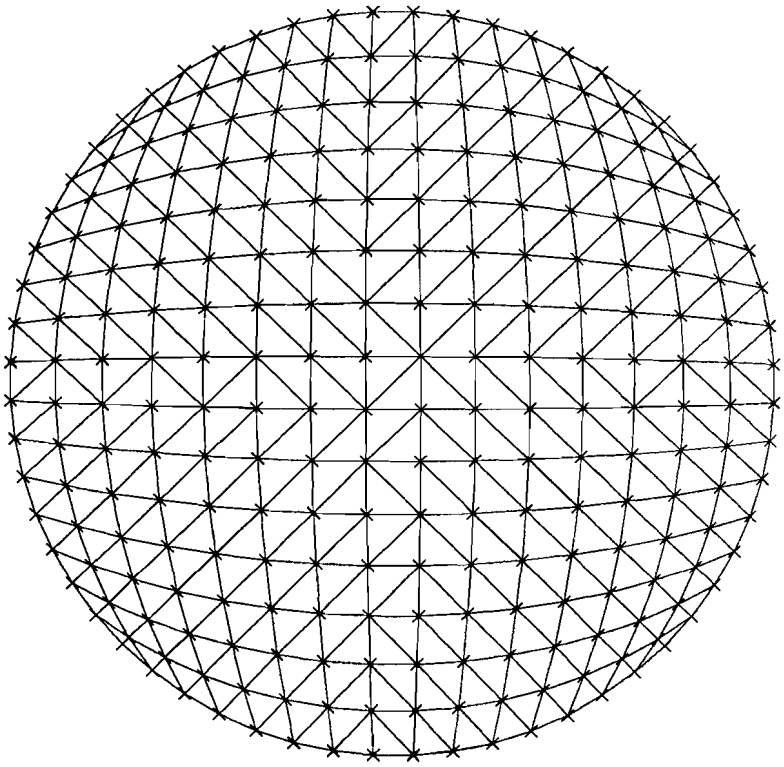

figure 6.2 Finite element discretization of a circular cylinder using 256 nodal points (60 boundary points) and 450 elements.

As a test of the accuracy of the numerical solution obtained by the hybrid method, the

diffraction problem for the cylinder for both the cases of transparent and soft boundary conditions has been solved by evaluation of the series solution (6.3).
In the computations the radius of the cylinder was taken 100 m, the shear wave velocities β^i and β for the interior respectively the exterior were 4000 and 3000 m/s. A uniform mass density of 2750 kg/m^3 was used throughout. The interior V was divided into 450 triangular elements (with piecewise linear interpolation), with 60 nodal points on the boundary and 196 in the interior, see figure 6.2. The total displacement field in the nodal points of the cylinder boundary was obtained in the frequency domain, both by the hybrid method and evaluation of the series solution.
The spectra were computed for a finite number of equidistant frequencies $0<f_i \leq 50$ Hz , where $f_i = i\Delta f$ and $\Delta f = .2$ Hz and .5 Hz for the series solution and the hybrid solution respectively. For the dimensionless wavenumber $ka = 2\pi a/\lambda$ in this experiment we have $0<ka \leq 10.47$.

The soft boundary case is considered first. Figure 6.3 shows the result of computations for the soft boundary condition of a hollow cylinder.

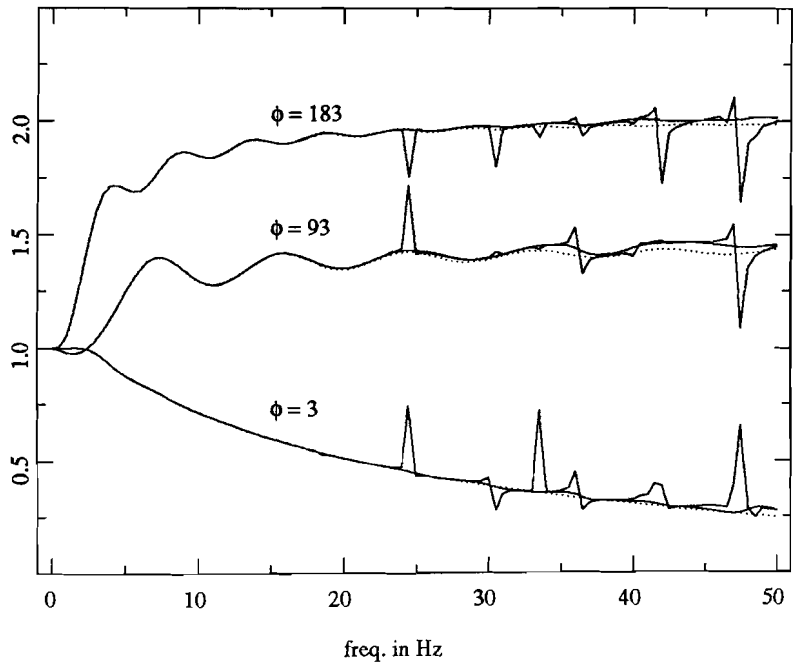

figure 6.3 Overlay plots of amplitude spectra for 3 evaluation points (ϕ=3°,93°,183°) from the hybrid method and the series solution - soft boundary case. The dented solid lines correspond to the solution obtained without using null field equations. Using eight null field equations results in the smooth solid curves. The dotted lines correspond to the series solution.

In this overlay plot amplitude spectra are plotted, evaluated in three points on the cylinder boundary, ϕ_1=3° (forward scattering), ϕ_2=93° and ϕ_3=183° (back scattering). The curves with the sharp indentations correspond to the result obtained without using

null field evaluation points. The frequency values of these indentations correspond with the characteristic frequencies of the cylinder listed in table 6.1, (see also appendix C).

(n,s)	$j_{n,s}=2\pi f_{n,s}\frac{a}{\beta}$	$f_{n,s}$	(n,s)	$j_{n,s}$	$f_{n,s}$
0,1	2.40482	11.48	1,1	3.83171	18.30
2,1	5.13562	24.52	0,2	5.52008	26.36
3,1	6.38016	30.46	1,2	7.01559	33.50
4,1	7.58834	36.23	2,2	8.41724	40.19
0,3	8.65373	41.32	5,1	8.77148	41.88
3,2	9.76102	46.61	6,1	9.93611	47.44
1,3	10.17347	48.57			

table 6.1 Characteristic frequencies - $f_{n,s}<50$ Hz - of a cylinder of radius $a=100$ m and wave velocity $\beta=3000$ m , $j_{n,s}$ is the s^{th} root of the n^{th} order Bessel function associated with an eigenvibration of angular order n.

The smooth curves closest to the previous ones result from adding eight null field evaluation points, the locations of which are defined in figure 6.1. Apparently the null field equations change the solution only near the characteristic frequencies.
The other smooth curves are derived from the series solution. It is clear from this figure, that adding the null field equations completely eliminates the erratic behaviour of the numerical solution near the characteristic frequencies. The remaining difference between the numerical and the series solution grows with the wave frequency and depends on several factors, namely:

(1) the discretization of the model geometry.

(2) the piecewise approximation of the solution on the boundary by means of linear interpolating functions (see appendix A).

(3) the use of numerical quadrature to compute the integral coefficients of the discretized integral equation.

The frequency spectra have been transformed to the time domain using the Fast Fourier Transform algorithm (Cooley and Tukey, 1965). The spectra were multiplied with a smooth waveform spectrum, tapering the response spectrum to zero at the limits and effectively limiting the frequency band to $0\leq f\leq 30$ Hz, $0\leq ka\leq 2\pi$, where the errors in the numerical results of the hybrid method are small (see figure 6.3). The equivalent time domain filter is one of a class of pulse forms, introduced in (Kuepper, 1958), defined as

$$f(t)=\begin{cases}\sin(\delta t)-\dfrac{1}{m}\sin(m\,\delta t)\ , t\in[0,T]\\ 0\ , t\notin[0,T]\end{cases}$$

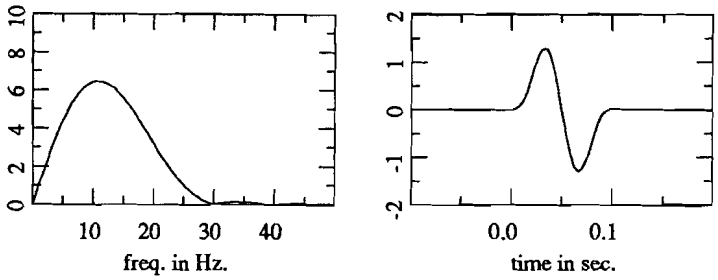

figure 6.4 Amplitude spectrum (left) and time pulse form (right) of the Kuepper filter $N=2$, $T=.1$ sec. The bandwith is effectively limited to $0\leq f\leq 30$ Hz, ($0\leq ka\leq 2\pi$ in the modeling experiment).

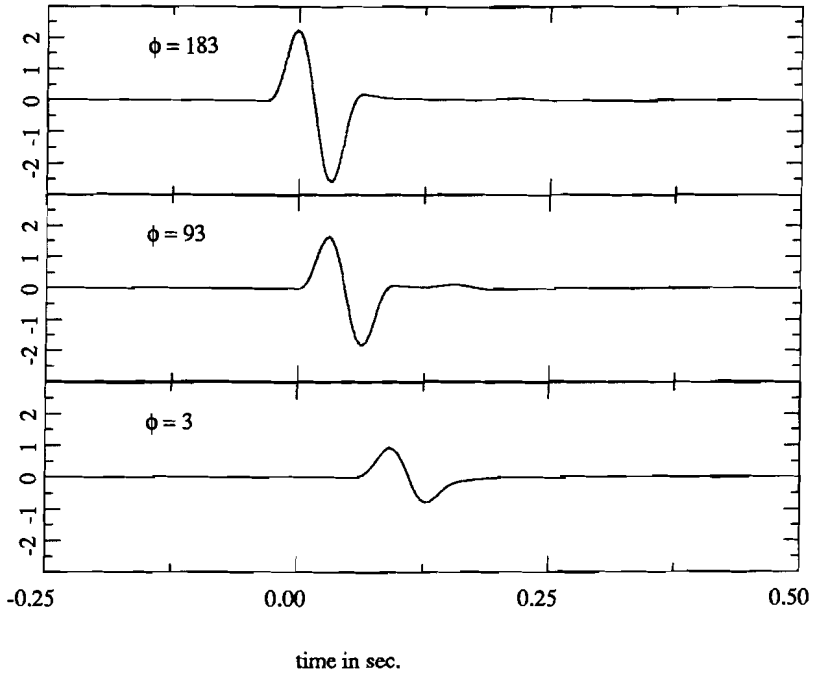

figure 6.5 Overlay plots of time domain responses corresponding with the amplitude spectra of fig. 6.3 after applying the Kuepper filter (fig. 6.4) ($0\leq ka\leq 2\pi$) - soft boundary.

where $\delta = \frac{N\pi}{T}$ and $m = (N+2)/N$.

In the results $N = 2$, $T = .1$ sec have been used. The pulse form and corresponding amplitude spectrum are plotted in figure 6.4. Figure 6.5 displays the displacements against time, corresponding with the amplitude spectra in figure 6.3, after application of the Kuepper filter. The figure is an overlay plot of results of the hybrid method - using eight null field points - and the series solution. The results agree to within a line thickness of the plots. Time domain results for a larger set of evaluation points, from $\phi=3^0$ to $\phi=183^0$ are given in figure 6.6.

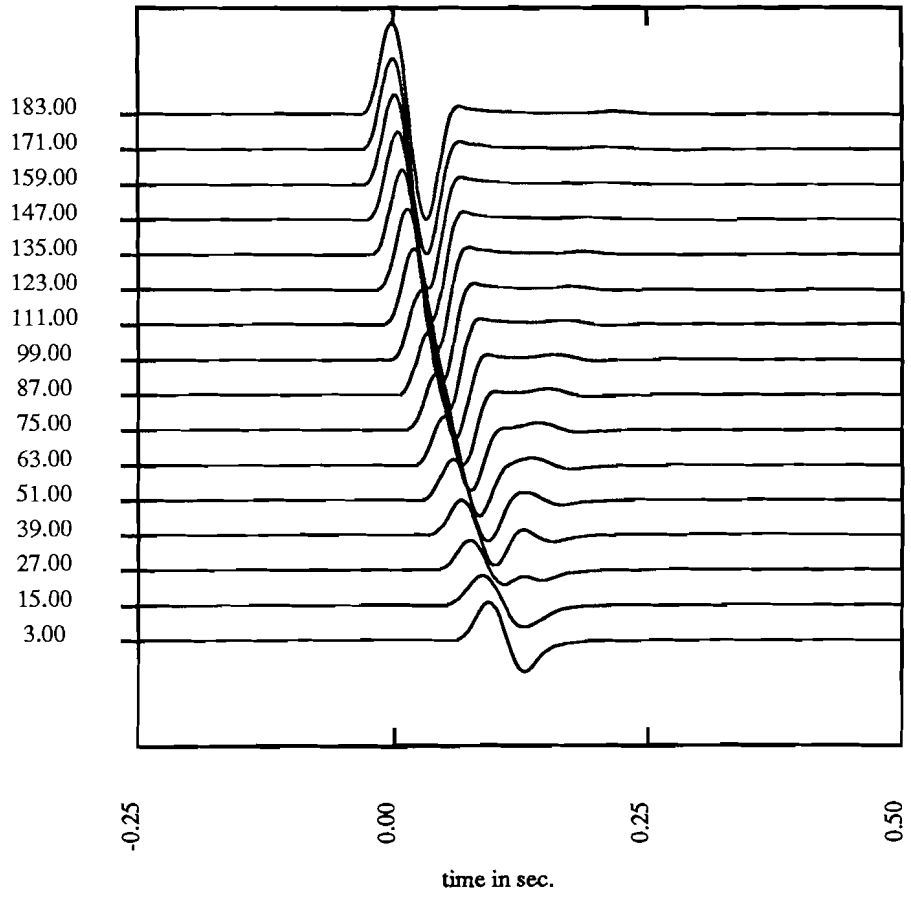

figure 6.6 Time domain response for evaluation points along the boundary ∂V after applying the Kuepper filter (fig. 6.4) ($0 \le ka \le 2\pi$) - soft boundary. Horizontal: time in seconds. Vertical: angular coordinate ϕ (in degrees) of the evaluation points. The traces for ϕ=3,93,183 correspond to the traces in fig. 6.5.

The displacement response in figure 6.6 is dominated by the incident field, although the amplitude of the primary pulse varies strongly, along the boundary, with low amplitudes in the shadow at the backside of the cylinder. A weak secondary pulse can be seen, travelling along the circumference of the cylinder.

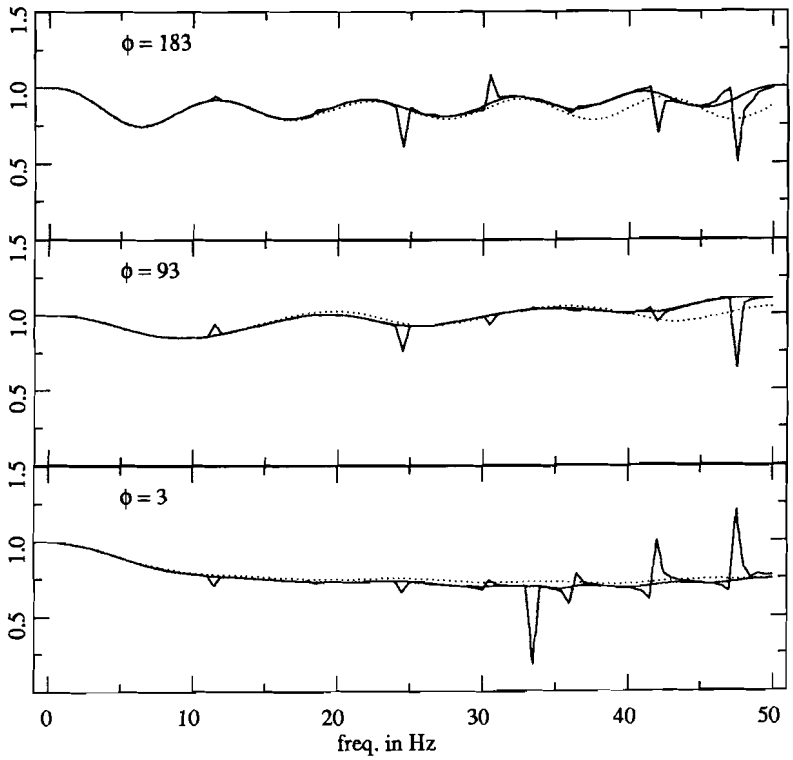

figure 6.7 Overlay plots of amplitude spectra for 3 evaluation points (ϕ=3°,93°,183°) from the hybrid method and the series solution - transparent boundary case. The dented solid lines correspond to the solution obtained without using null field equations. Using eight null field equations results in the smooth solid curves. The dotted lines correspond to the series solution.

In the following the transparent boundary case is treated. Figure 6.7 presents overlay plots of amplitude spectra as in figure 6.3, this time for the transparent case, where the cylinder is filled with high velocity material, β=4000 m/s. The results of the hybrid method without null field equations, obtained by solving the coupled finite element - integral equations are equally affected by the presence of the characteristic frequencies as shown by the curves with the indentations.
Using the same null field evaluation points as before (figure 6.1) in the soft boundary case, the large errors at the characteristic frequencies are eliminated. The remaining

error is a growing function of frequency.

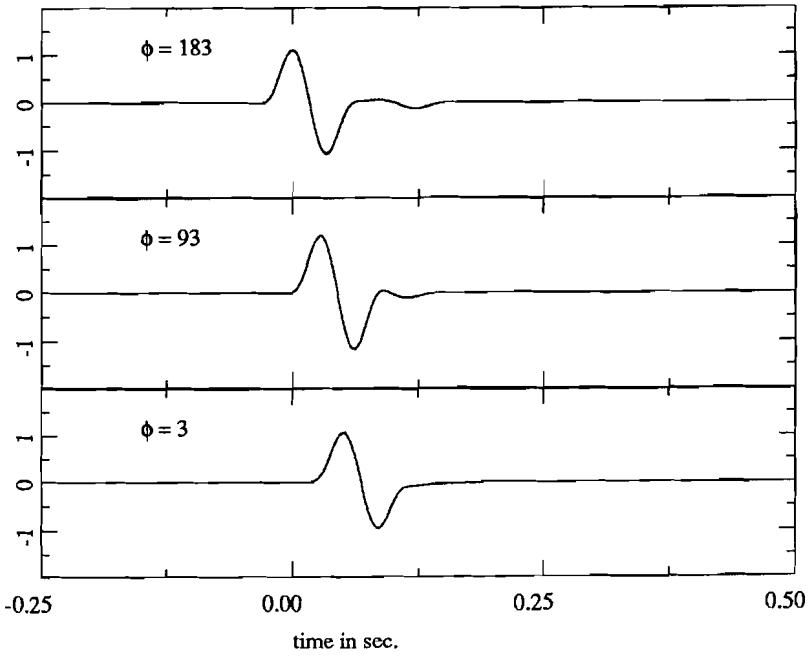

figure 6.8 Overlay plots of time domain responses corresponding with the amplitude spectra of fig. 6.7 after applying the Kuepper filter (fig. 6.4) ($0 \leq ka \leq 2\pi$) - transparent boundary.

Time domain results were computed using the same Kuepper filter as before. Figure 6.8 shows an overlay plot of displacement against time for three evaluation points from both the hybrid method and the series solution. As before the results agree to within a line thickness of the plot. In figure 6.9 results from the hybrid method for the same set of evaluation points as in figure 6.6 are plotted. The response is dominated by the incident pulse, the effect of the anomaly is most clearly visible on the trace with $\phi=183^0$ (back scattering), where a reflected/refracted pulse with an altered pulse form arrives at about .1 second after the first motion.

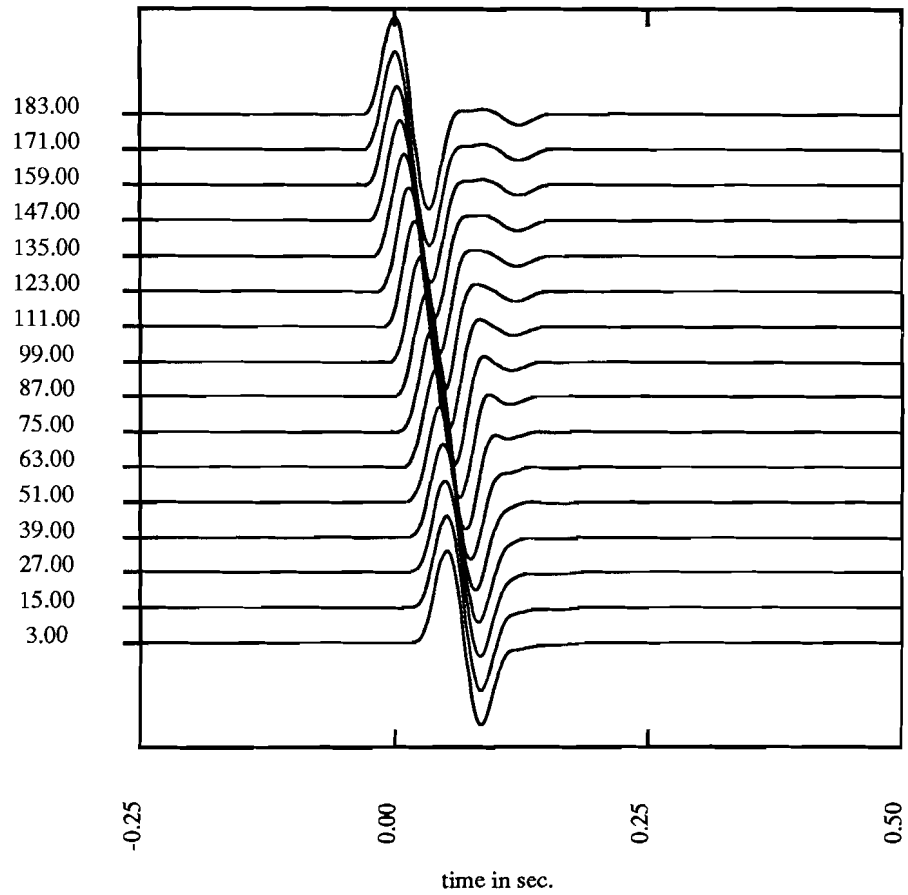

figure 6.9 Time domain response for evaluation points along the boundary ∂V after applying the Kuepper filter (fig. 6.4) ($0 \leq ka \leq 2\pi$) - transparent boundary. Horizontal: time in seconds. Vertical: angular coordinate ϕ (in degrees) of the evaluation points. The traces for ϕ=3,93,183 correspond to the traces in fig. 6.8.

An indication of the accuracy of a solution method for general problems of diffraction by transparent obstacles can be obtained by a zero-contrast experiment (Berkhoff,

1976). In a zero-contrast configuration, the scattering volume V is replaced by material with the the same parameters as in the exterior medium, such that the incident field u^0 satisfies the wave equation in the whole medium V_∞. For a homogeneous exterior medium used here, this means defining a scattering volume with homogeneous material parameters identical to the ones of the exterior domain $\rho^i=\rho$, $\beta^i=\beta$
The response to an incident plane wave for the cylindrical scatterer with zero-contrast parameters ρ=2750 kg/m^3 , β=3000 m/s was computed for the nodal points on the boundary ∂V, see figure 6.2. Using the incident field u^0 as a reference a relative error norm can be defined as

$$e = \left[\frac{\sum_J |u_J - u_J^{ref}|^2}{\sum_J |u_J^{ref}|^2} \right]^{\frac{1}{2}} \tag{6.10}$$

where the summation is over all the boundary grid points.
The available series solution for the finite contrast diffraction problem can also be used as a reference value in (6.10).

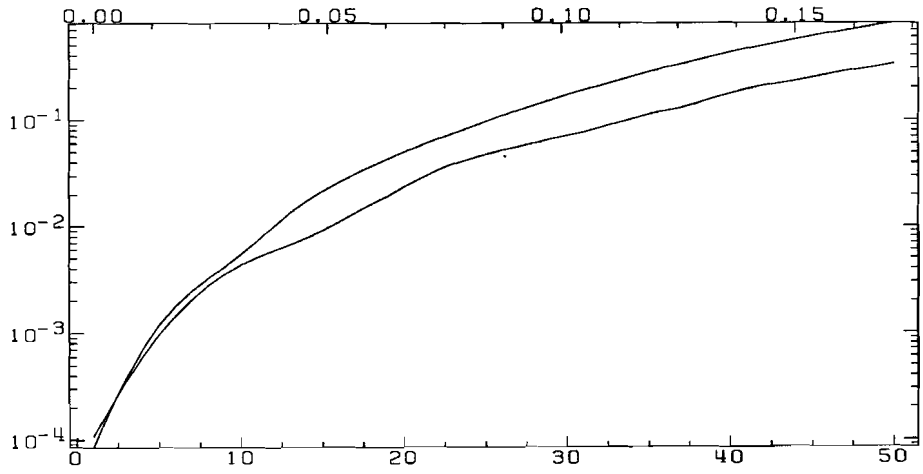

figure 6.10 Relative error versus frequency in Hz (bottom) and wave lengths per element - β=3000 m/s - (top) from the zero contrast test (upper) and comparison with the series solution (lower).

In figure 6.10 both error curves are plotted as a function of the frequency of the incident wave. The error depends strongly on the discretization of the model, in particular on the number of elements per wavelength. This can explain the difference between the two curves: in the zero-contrast test, the cylinder is filled with low velocity material,

resulting in a shorter wavelength and a smaller number of elements per wave length, compared with the finite contrast case. In addition to this, in the finite contrast case only part of the wave energy penetrates into the cylinder and therefore the total response depends less strongly on the characteristics of the finite element grid.
From the error curves it can be seen, that for the frequency domain tapering used the error at the predominant frequency of 10 Hz is in the order of 1% , while the error at the 30 Hz effective upper band limit is 7% . It can also be concluded, that in order to keep the error norm below 10% , a minimum of 10 elements per wavelength is required. The admissible error in the numerical solution depends on the type of problem to be solved. For instance in the computation of time domain results, as displayed in figure 6.6 the error depends mainly on the dominant frequency f_d of the incident wave, so that an error of 10% at the maximum frequency $f_{\max}$ is acceptable.

6.2. Wave diffraction by rectangular obstacles

In this section some results of modeling experiments with scatterers of rectangular geometry are presented.
A scatterer with a non smooth boundary generates diffracted waves, that can be thought of as originating from boundary points with a discontinuity in the normal vector. The integral equation for the boundary field (4.29b) accounts for deviations from the smooth boundary case.
In section 6.2.1 results of an experiment with a plane wave incident on a square high impedance obstacle in a homogeneous whole space are presented. In section 6.2.2, modeling of a zero offset reflection seismic experiment is discussed illustrating the flexibility in the definition of the model excitation.

6.2.1. Effect of a square obstacle on a plane wave

In this experiment a plane wave in a whole space is normally incident on one of the sides of a square obstacle of 200 m×200 m. The geometry of the experiment is depicted in figure 6.11.

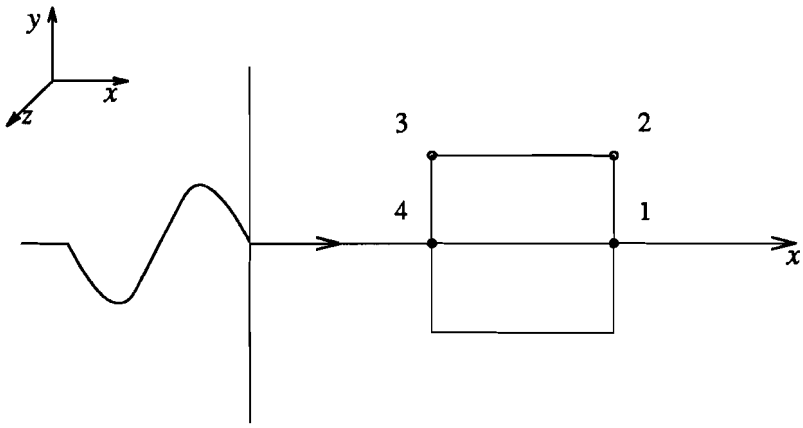

figure 6.11 Plane wave traveling parallel to the x axis, incident on a square cylinder with axis parallel to the z axis, circles denote evaluation points, referred to in the text.

The material parameters for the background medium were $\rho = 2750\ \mathrm{kg/m^3}$, $\beta = 3000\ \mathrm{m/s}$ and for the homogeneous inclusion $\rho^i = 2225\ \mathrm{kg/m^3}$, $\beta^i = 4000\ \mathrm{m/s}$.

The model response was computed for frequencies $0<f_i \leq 50$ Hz, $f_i = i\Delta f$, $i=1,\cdots,100$, $\Delta f = .5$ Hz. Defining the characteristic dimension $a=L/2$, L the length of the sides of the square, we have for for the dimensionless wavenumber $ka = 2\pi a/\lambda$ in this modeling experiment, $0<ka \leq 10.47$. The model was discretized using a 16×16 uniform grid with 450 triangular elements and piecewise linear interpolation.

As for the cylindrical model in section 6.1 a number of null field evaluation points were defined to deal with the non-uniqueness problems of the integral equations for the characteristic frequencies of the obstacle. As shown in appendix C, the characteristic frequencies are the eigenfrequencies of the interior homogeneous Dirichlet problem. The interior Dirichlet problem can be solved analytically (in contrast to the exterior problem), using separation of variables in Cartesian coordinates. This leads to the expression for the eigenfrequencies

$$\omega_{nm} = \frac{\beta\pi}{L}(n^2+m^2)^{1/2} \quad , n,m = 0,1,\cdots \tag{6.11}$$

The corresponding dimensionless wavenumbers are

$$(ka)_{nm} = \frac{\omega_{nm} a}{\beta} = \frac{\pi}{2}(n^2+m^2)^{1/2} \tag{6.12}$$

In table 6.2, the dimensionless wavenumbers and corresponding characteristic frequencies below 50 Hz are given, together with the order numbers n, m.

(n,m)	ka	$f_{n,m}$	(n,m)	ka	$f_{n,m}$
0,1	1.57	7.5	1,1	2.22	10.6
0,2	3.14	15.0	1,2	3.51	16.8
2,2	4.44	21.2	0,3	4.71	22.5
1,3	4.97	23.7	2,3	5.66	27.0
3,3	6.66	31.8	0,4	6.28	30.0
1,4	6.48	30.9	2,4	7.02	33.5
3,4	7.85	37.5	0,5	7.85	37.5
1,5	8.01	38.2	2,5	8.46	40.4
4,4	8.89	42.4	3,5	9.16	43.7
0,6	9.42	45.0	1,6	9.55	45.6
2,6	9.93	47.4	4,5	10.06	48.0
3,6	10.54	50.3			

table 6.2 Characteristic frequencies, of a square model associated with eigenvibrations of order numbers n, m.

The eigenvibrations corresponding, with the characteristic frequencies are

$$u_{nm}(x,y) = \sin(n\pi\frac{x}{L})\sin(m\pi\frac{y}{L}) \tag{6.13}$$

The explicit form (6.13) can be used in the choice of the null field evaluation points. The eigenvibrations of the square model are completely defined by (6.13). This in contrast with the situation for the circular model of section 6.1, where there is a rotational indeterminacy in the eigenfunctions.
In figure 6.12 the nodal lines of the eigenvibrations of order numbers $n, m < 6$ are plotted.
As shown in appendix C , it is necessary to choose the evaluation points of the null field equations away from the nodal lines of an eigenvibration. In the computations eight null field evaluation points have been used, denoted by the small circles in figure 6.12.

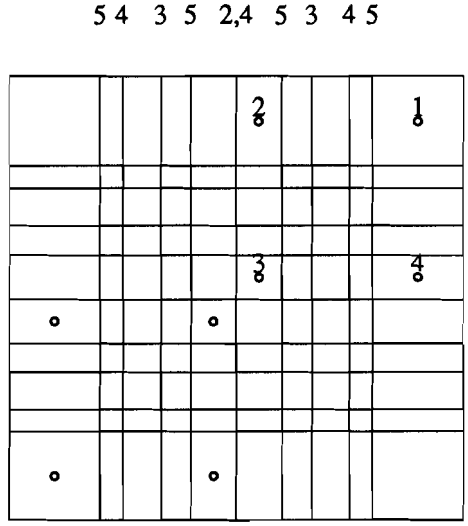

figure 6.12 Location of the null field evaluation points (circles) in the interior of the square obstacle - coordinates in meters $(x_i,y_i), i=1,\cdots,4$ (80,80),(10,80),(10,10), (80,10) - relative to the nodal lines of the first few internal Dirichlet eigenvibrations (order $n, m \leq 5$ - numbers along the top boundary).

Amplitude spectra of the boundary displacement field were computed for the four points denoted by circles in figure 6.11 , both with and without using the null field equations mentioned. Overlay plots of the results are given in figure 6.13. Clearly the solutions are improved using the null field equations, although some irregularities in the

spectra persist for characteristic frequencies corresponding with higher order vibrations (f =37.5,40.4 Hz, ka=7.85,8.46 see table 6.2).

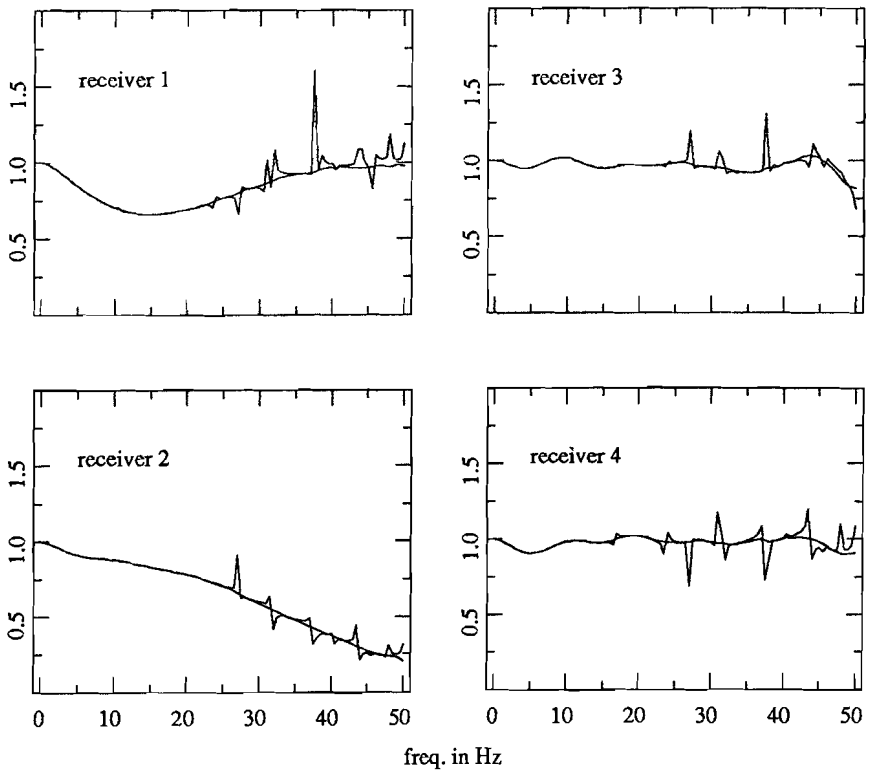

figure 6.13 Overlay plots of amplitude spectra for 5 evaluation points see fig. 6.11. No null field equations were used to obtain the dented curves. For the smooth curves, eight nullfield points (plotted in fig. 6.12) were used.

Time domain results, for the same four recording points along the boundary contour are displayed in figure 6.14 . The same Kuepper filter as in section 6.1 has been applied to the computed spectra. Clearly the response is largely dominated by the incident wave (see also figure 6.8, due to the small contrast between the material parameters of the obstacle and the background medium.

Using the field values computed for the boundary grid points, the displacement spectra for several off-boundary points were computed, using (5.16) with $\mathbf{F}_I = \mathbf{0}$ for points in the interior and (5.18,19) for external evaluation points. Figure 6.15 shows the location of the evaluation points. The total displacement in the time domain, for this array of receivers is plotted in figure 6.16.

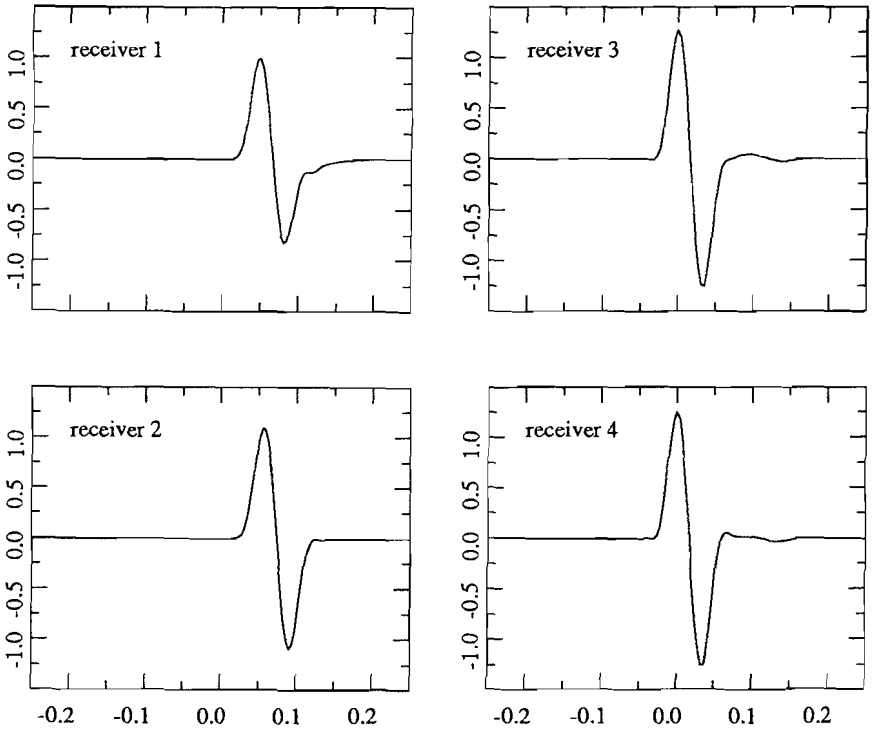

figure 6.14 Time domain results for the same evaluation points as in fig. 6.13.

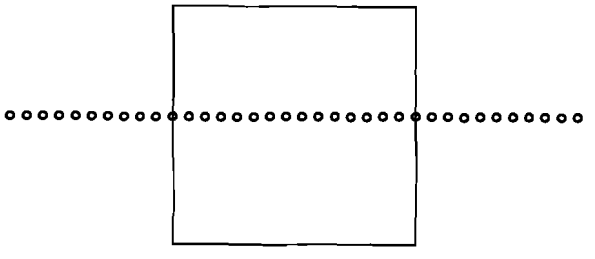

figure 6.15 Array of receivers (circles) at 13.3 m intervals corresponding to the traces plotted in fig. 6.16. Internal receivers are located in adjacent finite element grid points. Model configuration as in fig. 6.11.

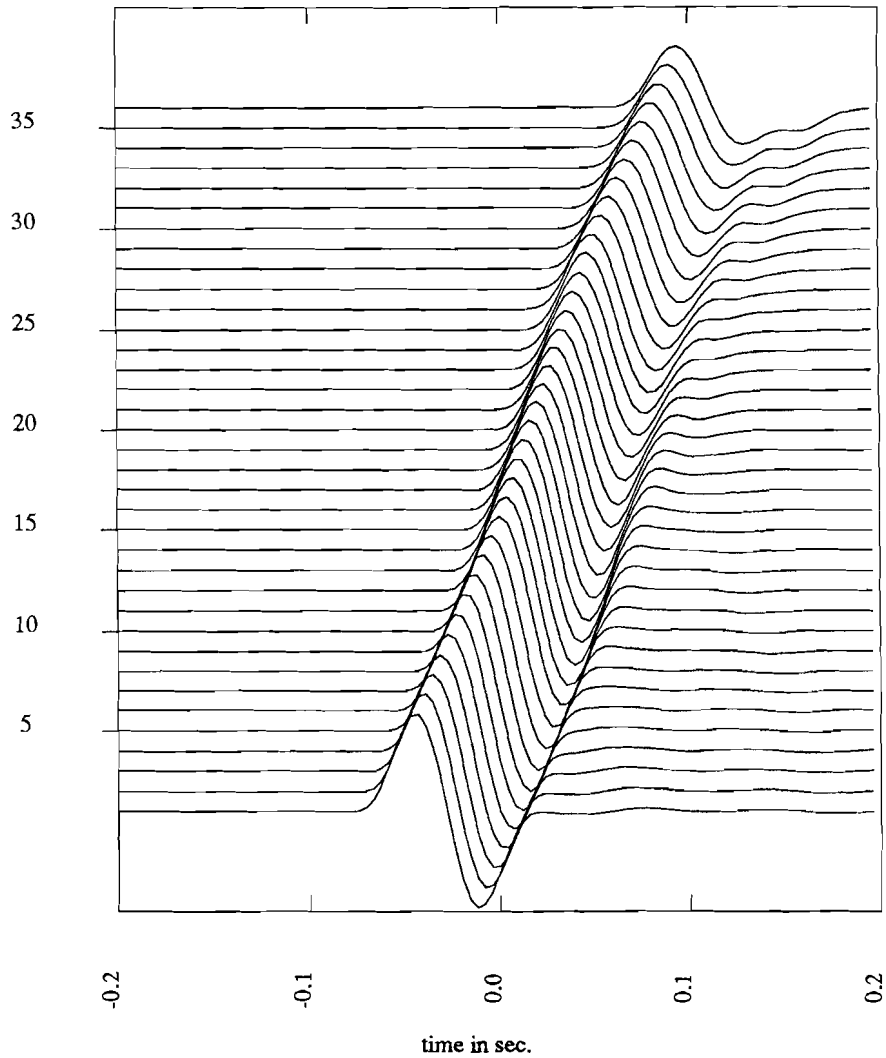

figure 6.16 Time domain results for the receivers of fig. 6.15. Traces from bottom upwards correspond to receivers from left to right. Traces 11 and 26 corespond to the receiver signals 4 and 1 respectivelly of figure 6.14. Vertical scale 1. units/cm.

As in figure 6.14 the response in figure 6.16 is dominated by the incident field. The times of maximum amplitude show a difference in moveout between interior and exterior points, corresponding to the higher internal wave velocity. There is an amplitude reduction of about 30 % at the backside of the obstacle, due to energy lost in back scattering. A first weak reflection of negative polarity can be seen on the lower traces at about .05 sec, followed .1 sec later by a positive reflection from the backside wall of

the the obstacle. On the uppermost traces the weakened primary pulses are followed by a diffracted wave. In figure 6.17 the scattered field alone is plotted, for the receivers in front of the obstacle. The vertical scale differs a factor 25 between figures 6.16 and 6.17. The two reflected pulses are now clearly visible, at .1 second interval, corresponding to the two way travel time in the obstacle.

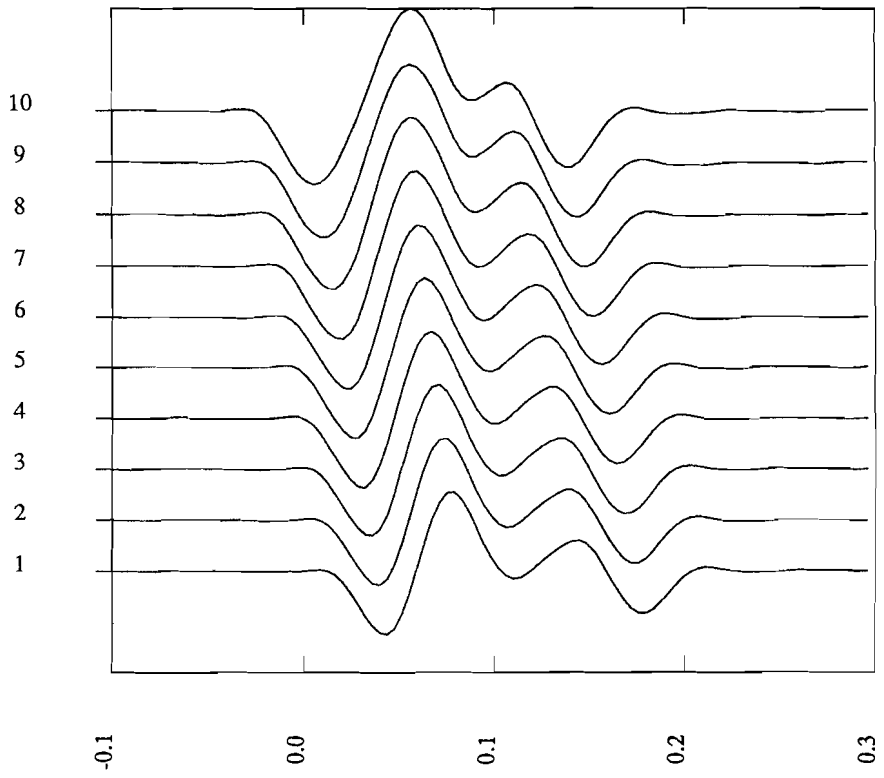

figure 6.17 Scattered field for the receiver points left of the obstacle in fig. 6.15. Receivers from left to right correspond to traces from bottom upward. Vertical scale .04 units/cm.

For the same model geometry, wave excitation and receiver layout as before, we have modeled the diffraction effects of a cavity. Figure 6.18 shows the scattered wave in the same 10 receivers in front of the square cavity. The primary reflection is now of positive polarity and much stronger than in the transparent boundary case of figure 6.17. The vertical scale differs a factor 37.5 between figures 6.17 an 6.18. Instead of a back wall reflection, there is now a negative low frequency bulge in the traces, suggesting a more complicated interaction between the obstacle of the cavity and the incident plane wave than before in the transparent boundary case.

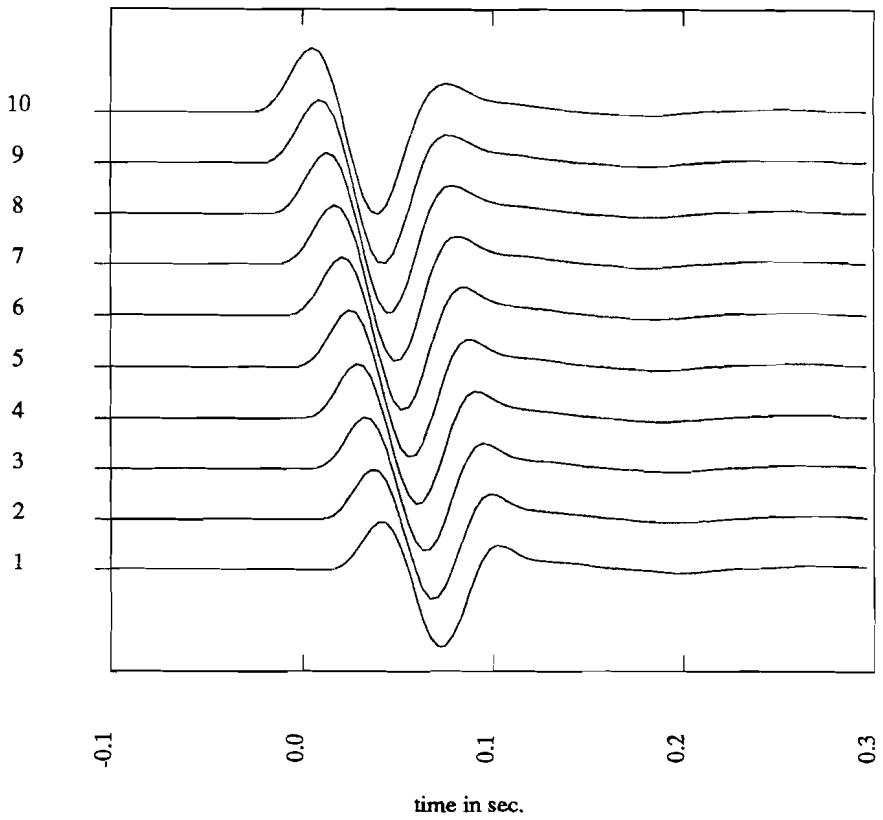

figure 6.18 Scattered field from a cavity for the same receiver points as in fig. 6.17. Vertical scale 1.5 units/cm.

6.2.2. A zero offset reflection experiment

As an illustration of the flexibility of the hybrid method in the definition of the wave field excitation of the model, a zero offset measurement from reflection seismology was simulated. In reflection seismology the wave field is often treated as an acoustic pressure field in a fluid (Waters, 1978), described by a scalar wave equation for the excess pressure p. For a homogeneous medium without sources this equation is given by Morse and Ingard (1968)

$$\nabla^2 p + k^2 p = 0$$

where $k=\omega/c$, $c=\frac{1}{\sqrt{\kappa\rho}}$ is the acoustic wave speed and κ is the compressibility of the medium. Since the pressure field satisfies the same (Helmholtz) equation as the horizontally polarized shear waves in a 2-D medium (6.2) we can use the implementation of the hybrid method for 2-D SH waves to solve acoustic 2-D modeling problems.

Figure 6.19 shows the layout of an array of coincident sources / receivers relative to the same square obstacle used in 6.2.1.

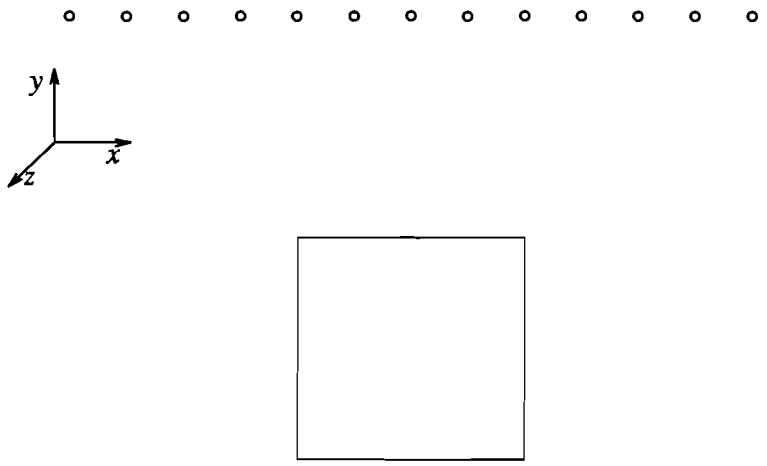

figure 6.19 Zero offset model configuration: array of coincident sources / receivers (circles) at 50 m intervals above a square anomaly (200 m × 200 m) centered 300 m below the array.

The zero offset section is an important way of data representation used in the interpretation of reflection seismic data. Idealy a zero offset section would be obtained from a series of measurements for coincident source / receiver pairs, spaced at regular intervals. In practice common midpoint stacks of seismograms are used as an

approximation of a zero offset section (Waters, 1978). To simulate an explosive source with an isotropic radiation pattern in a 2-D whole space, we have used in our 2-D SH implementation, a unit force in the z direction, concentrated at the source point $\mathbf{x}_s$. The incident field $u^0(\mathbf{x})$ in that case equals the Green's displacement field $G(\mathbf{x},\mathbf{x}_s) = \frac{i}{4\mu} H_0(k \mid \mathbf{x}-\mathbf{x}_s \mid)$, ($H_0$ the Hankel function of the first kind of zero order).

In response computations in cases like these, where we have multiple wave excitations, a substantial economization in the computation time can be obtained. The first and most time consuming step ($O(n^3)$ operations, n the dimension of the matrix) in the solution for the boundary field is the reduction of the matrix $\mathbf{C}$ of the algebraic equation (5.15), (see chapter 5). Since the incident wave field occurs only in the right hand side of the equations the matrix reduction can be kept outside the program loop over the different incident wave fields. Only the second (back-substitution) part - ($O(n^2)$ operations) has to be performed inside the inner program loop over the different incident wave fields.

In figure 6.20 the scattered field at the receiver locations is plotted, the primary arrivals consist of reflections from the front wall of the obstacle for the central receivers, gradually transforming into diffractions from the edges of the scatterer towards the end of the receiver array.

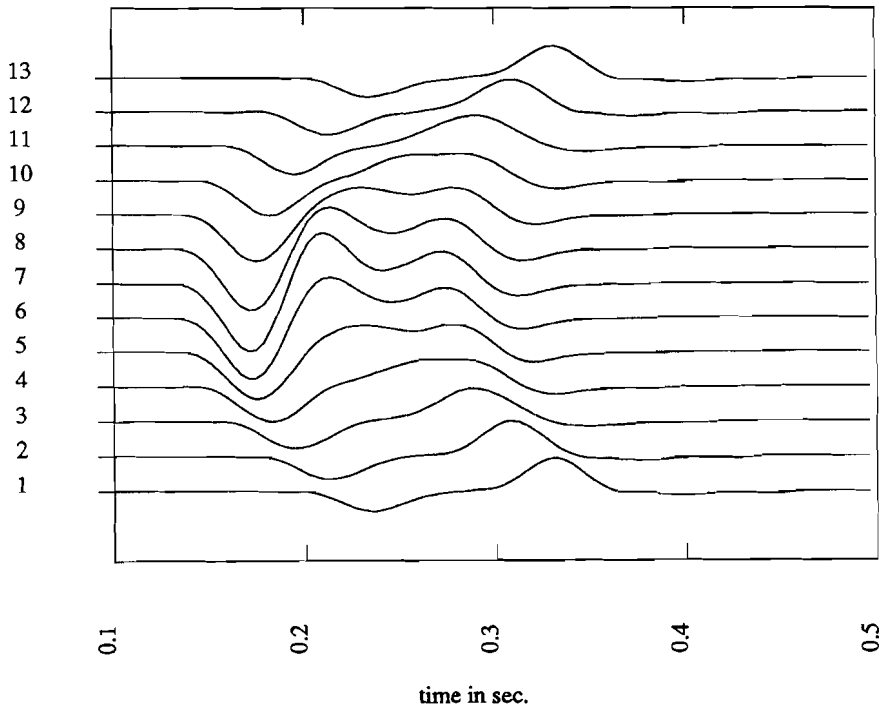

figure 6.20 Zero offset results. Scattered field in the receivers of fig. 6.19.

6.3. Effects of an anomaly at the free boundary of a halfspace

In this section some results will be presented of modeling wave propagation phenomena for an anomaly near the surface of a halfspace. In case the anomaly can be modeled as an irregularity of finite volume in an otherwise regular halfspace, the problem can be solved by the hybrid finite element / boundary integral equation method.
The problem of modeling the effects of anomalies near a halfspace boundary has been addressed in the seismological literature by several authors. Aki and Larner developed a method to compute SH wave fields based on a discrete wavenumber expansion of the field, excited by a plane incident wave, (Aki and Larner, 1970; Aki and Richards, 1981). The method was extended to include P-SV problems and excitation by earthquake sources within the model, (Bouchon and Aki, 1977). Bard and Bouchon further extended the method to produce time domain results, (Bard and Bouchon, 1980). Several authors have applied the finite difference method to the problem (Boore et al., 1971; Kelly, 1983; Zahradnik, 1984; Levander and Hill, 1985; Hong and Bond, 1986). The finite element method was applied in (Lysmer and Drake, 1971; Smith, 1975; Day, 1977; Crichlow, 1982). Wong and Jennings (1975) and Sills (1978) applied an integral equation technique related to the one included in the present hybrid method to the study of diffraction of plane SH waves by a surface topography in the free surface of a homogeneous 2-D halfspace. Sanchez-Sesma (1982, 1983) used a boundary integral technique based on a plane wave expansion of the field and a least squares approximation of the boundary conditions of an anomaly.

6.3.1. Diffraction by a 2-D canyon topography

In this section the effect of surface topography upon an incident wave field is modeled. In the assessment of seismic risk of a certain location it is important to know the amplification and de-amplification effects that the surface structure may have on an incident wave field (Wong and Jennings, 1975; Sanchez-Sesma, 1983).
A surface topography forms a special case in which the hybrid method reduces to a single integral equation on the irregular part of the free surface of a halfspace. Thus the dimension of the problem to be solved is reduced by one. This means, that only the boundary surface of the anomaly has to discretized in stead of the whole volume of the domain of interest. This greatly reduces the number of unknowns in the problem to be solved.
This follows directly from the matrix equation (5.5), when the traction value vector $\mathbf{T}$ is set to zero, corresponding with a free boundary.
The resulting equation to be solved for the surface displacements $\mathbf{U}_R$ is,

$$\mathbf{B}\mathbf{U}_R = \mathbf{E} \tag{6.14}$$

The matrix **B** is defined in section 4.4.2.1, where in particular the application to media other than homogeneous whole spaces is discussed. The required Green's state for scalar waves in a homogeneous halfspace can be easily constructed using the principle of image sources (Morse and Fesbach, 1953).

The effect of a canyon topography in a 2-D halfspace on an incident plane SH wave has been modeled. The wave propagates in a direction perpendicular to the canyon axis, resulting in a 2-D configuration, see figure 6.21.

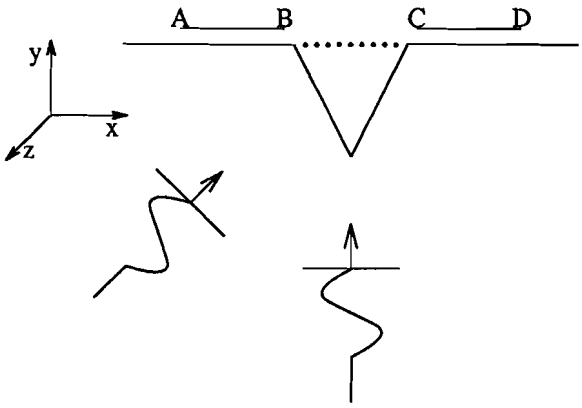

figure 6.21 Model configuration, plane waves - normal vectors in the x,y plane - incident on an empty triangular canyon, with axis parallel to the z axis. Receivers are placed in arrays AB,CD and along both canyon walls. Dots denote null field evaluation points along $y=0$.

The canyon is 300 m wide and deep. Both the walls were discretized with 41 equidistant nodal points. The location of 9 null field evaluation points used in the response computations (see appendix C) are depicted by the dots in figure 6.21. The shear velocity of the halfspace is 3000 m/s, the mass density is 2750 kg/m^3.

The model response was calculated for equidistant frequencies $0<f_i\leq 75$ Hz, $f_i=i\,\Delta f$, $i=1,\cdots,75$, $\Delta f=1$. Hz. The characteristic dimension of the wave obstacle is defined equal to the width and depth of the canyon, $a=300$ m. Thus we have for the dimensionless wave number $ka\leq 15\pi$. Plane waves with incidence angles of 0^0 (vertical incidence) and 45^0 (oblique incidence) were used for the model excitation, see figure 6.21.

Two arrays of 40 receivers each have been modeled along the halfspace boundary on both sides of the canyon (lines AB and CD in figure 6.21). The array sensor spacing is 7.5 m. In addition to the receiver arrays AB and CD, receiver points were located at every second grid point along the canyon walls, resulting in another 39 receivers, spaced 7.5 m apart in the x direction. Figures 6.22a,b give the displacement amplitudes for the receivers along the surface and on the canyon walls, for five frequencies f_i = 1,3,5,7,9 Hz, from the top downwards.

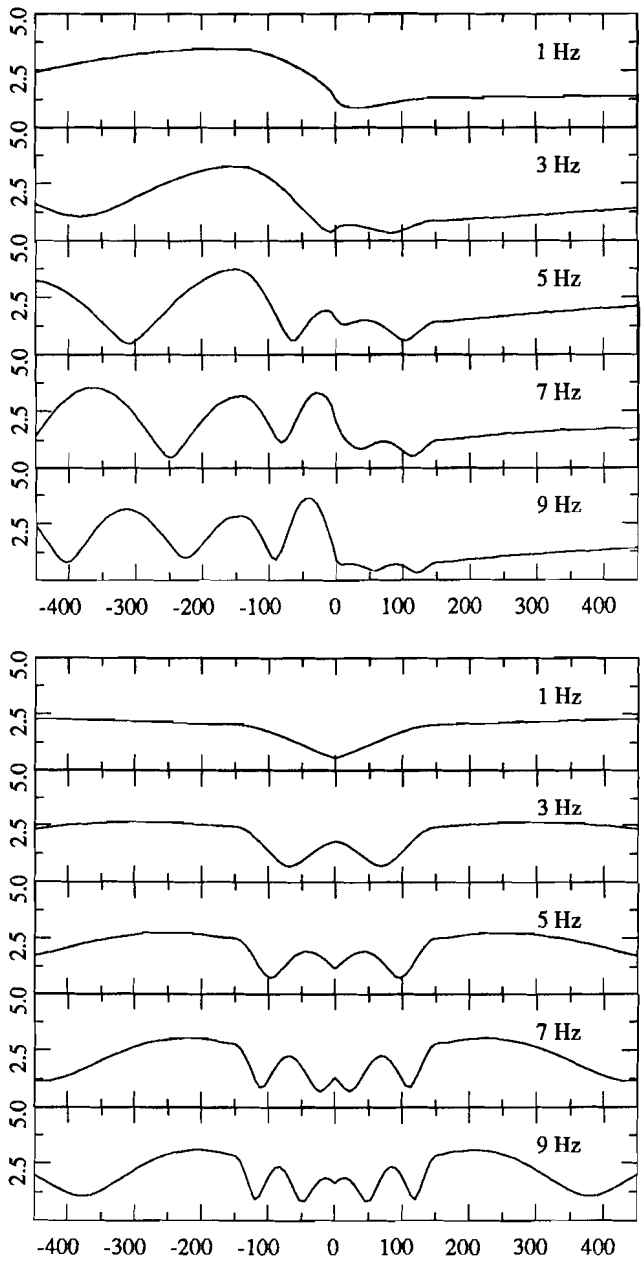

figure 6.22a,b Displacement amplitude versus x, for frequencies 1,3,5,7,9 Hz. Receivers along the free surface and both walls of the empty canyon. a) top : oblique incidence. b) bottom: vertical incidence.

The figures correspond to incidence angles of 45^0 and 0^0 respectively. The low frequency curves in the three plots approach the limit 2, that would be observed without the topography in the surface - corresponding to a unit amplitude incident wave field and a unit reflection coefficient of the halfspace surface.
For $\theta = 45^0$ there is a strong amplification effect in the left-hand (lit) side of the model, with a corresponding de-amplification on the right-hand (shadow) side, see figure 6.22a. In the vertical incidence case $\theta = 0^0$ in figure 6.22b, the maximum amplification of 1.5 - within the frequency band 0.,10. Hz - occurs at $|x|$=200 m , just outside the canyon. On the canyon walls the amplitude fluctuates more rapidly than outside the canyon. Strong fluctuations of amplitudes over short distances along the canyon walls result in large strains, which may for instance enlarge the risk of instabilities in the topography.

In order to study the time dependence of the model response, the frequency spectra have been transformed to the time domain. As in 6.2 multiplication with an excitation spectrum was applied in the frequency domain, to taper the frequency response and to obtain a simple time domain pulse form. The resulting pulse form and amplitude spectrum are shown in figure 6.23.

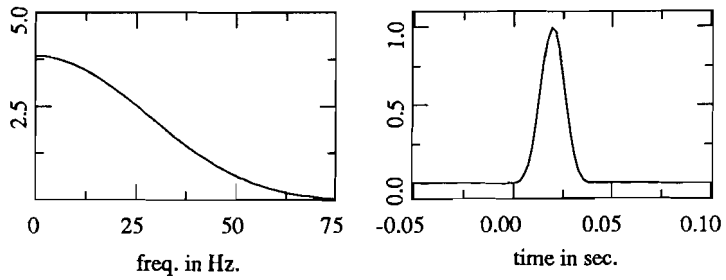

figure 6.23 Amplitude spectrum (left) and time pulse form (right) used for the incident field waveform.

In figure 6.24a the displacements of 161 points located along the free surface are plotted (2×40 array sensors, 81 nodal points on the canyon walls) .
The incidence angle of the plane wave is 45^0, and the right-hand side wall is in the geometrical shadow of the canyon. The response of the left-hand side - traces 1 to 81 - is dominated by the incident wave field including a free surface reflection. A weak diffraction from the canyon tip (trace 81) - with reversed polarity and smaller apparent velocity - can be distinguished following the primary onsets. The strong later arrivals are the waves that have been reflected at the left-hand side canyon wall - arrivals on traces 1 to 40 - or at the free surface - arrivals on traces 40 to 81 .
The receivers located on the right-hand side wall can only receive energy diffracted around the canyon tip. The diffracted wave arriving at the surface generates a weak secondary diffraction.

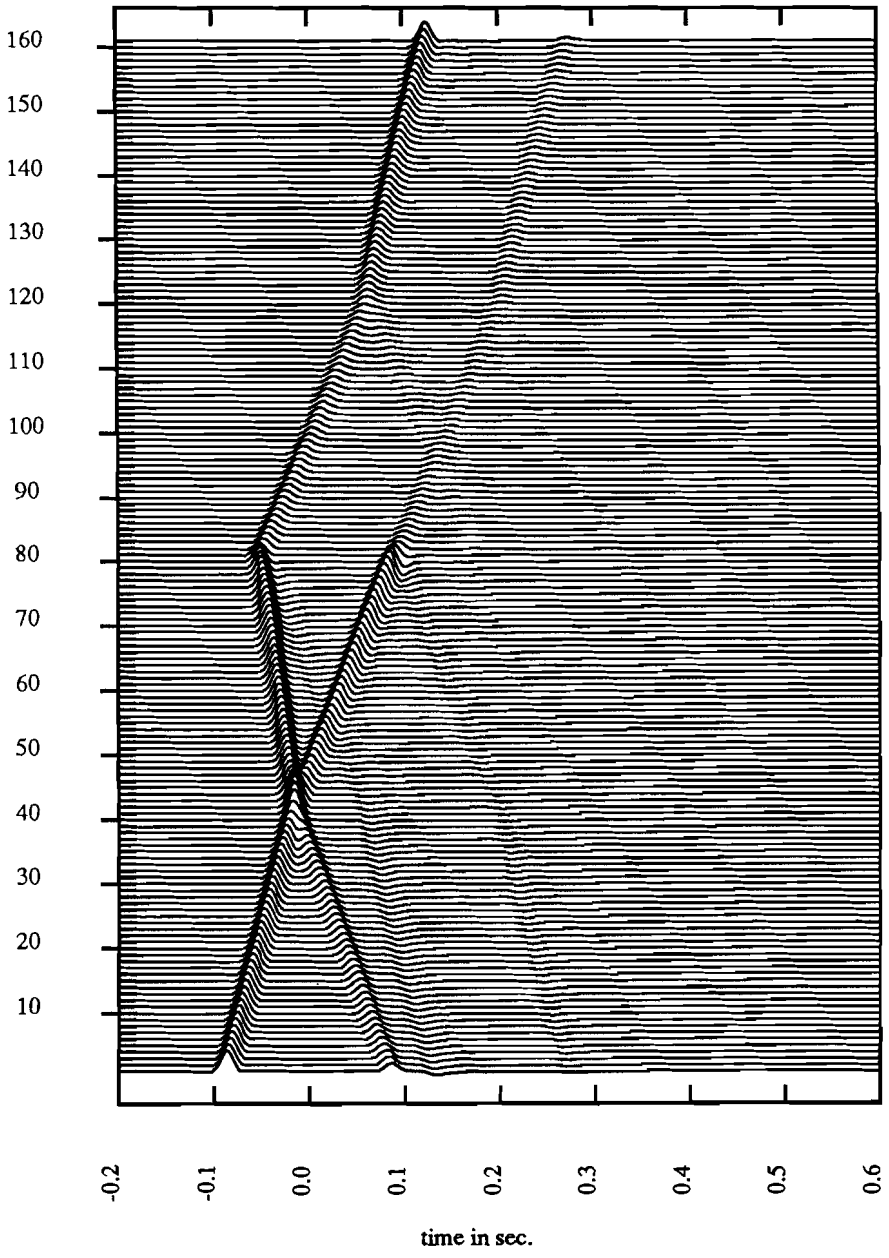

figure 6.24a Time domain displacement field for two sets of receivers: 1) 2×40 receivers in arrays AB and CD of fig. 6.21 (traces 1-40,122-161) and 2) 81 receivers along both canyon walls (traces 41-121). Oblique incidence case.

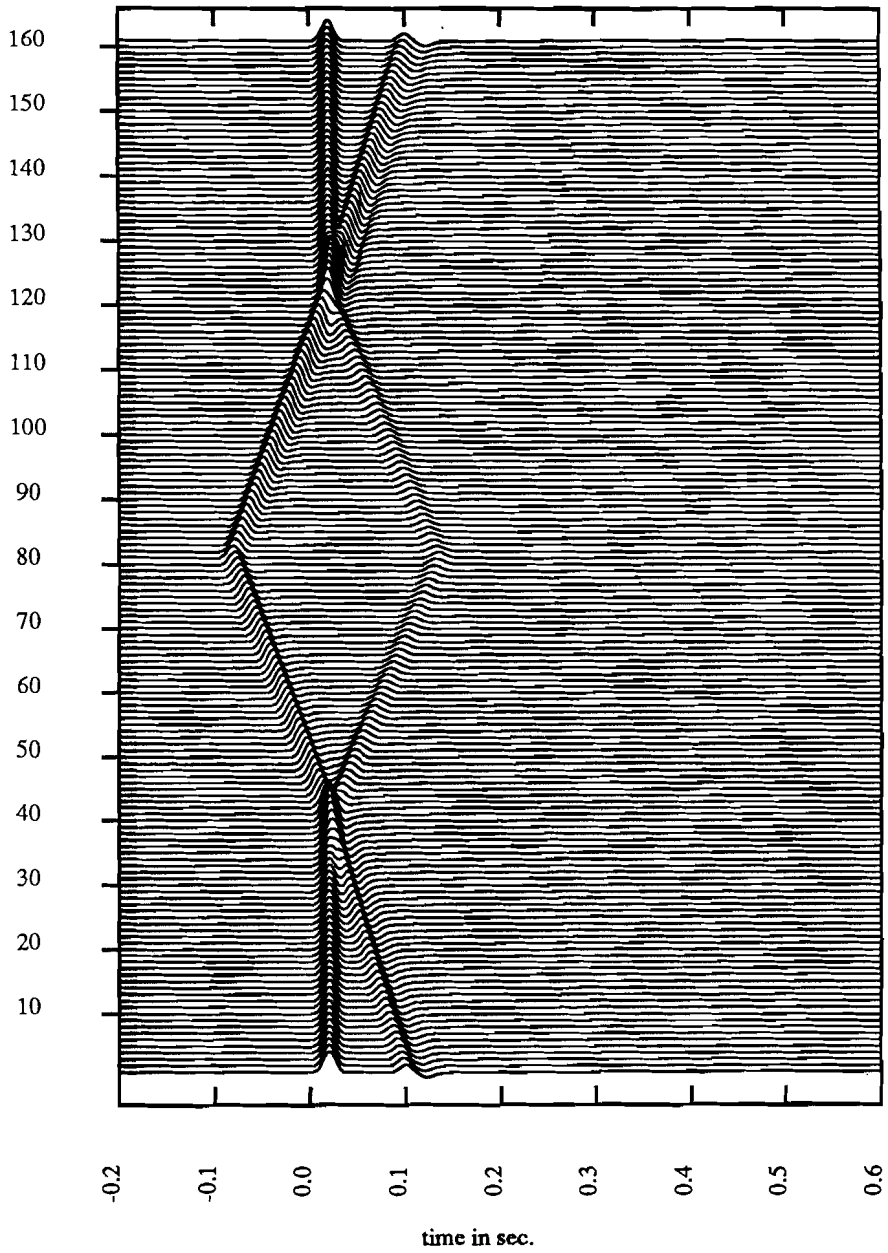

figure 6.24b Time domain displacement field for two sets of receivers: 1) 2x40 receivers in arrays AB and CD of fig. 6.21 (traces 1-40,122-161) and 2) 81 receivers along both canyon walls (traces 41-121). Vertical incidence case.

Figure 6.24b displays the displacement response for the same configuration for a plane wave of 0^0 incidence angle. The primary arrivals correspond to the vertically incident plane wave. The secondary arrivals in the receiver array arise from the canyon wall reflection and the diffraction at the canyon edges. The secondary arrival in the boundary nodal points correspond with energy diffracted at the canyon edges.

In order to check their validity, the results have been compared with computational results obtained by Zahradnik, who used a finite difference method in the time domain, with difference approximations of second order accuracy in space and time. For details of this method see (Boore, 1972; Alford et al., 1974; Zahradnik, 1978). The discretization used a time step of .002 sec and a grid of square cells sized 10 m.
As a rule of thumb, the grid spacing h, i.e, the dimension of the largest grid cell and the maximum frequency in the bandwidth f_{max} should satisfy the constraint $f_{max} = \beta_{min}/(10\,h)$, where β_{min} is the minimum shear velocity in the model.
This corresponds with a minimum of 10 grid cells per wavelength in the wave field and will limit the numerical dispersion and damping to a few percent for model sizes not exceeding a few wavelenghts (Alford et al., 1974; Zahradnik and Urban, 1984). In practice f_{max} can be replaced by an effective upper limit of the source bandwidth, for instance the upper half power frequency of the source spectrum (Alford, 1974). For the present model the discretization criterion is $f_{max} = 30$ Hz. The results of the two different methods are shown in figure 6.25, where the solid and the dotted curves correspond to the results of the hybrid method and the finite difference method respectively.
The plot shows the displacements for 14 receivers located along the right-hand side canyon wall and along the surface of the halfspace as displayed in figure 6.26. The results are for vertical incidence. The plot shows the arrival of the incident wave, interfering with the canyon tip diffraction along the wall. The reflection of the canyon wall interfering with the edge diffractions results in the secondary arrivals on the surface receivers.
The results agree well, although some differences remain. The pulse form of the finite difference results is changed as the wave travels through the grid, resulting in an oscillatory wave tail. This is most clearly visible on the traces from the receivers along the surface of the halfspace.
In the hybrid method, the primary arrivals on the surface traces correspond to the incident field u^0 (including the surface reflection) - the total field is defined as $u = u^0 + u^{sc}$ - where the scattered field u^{sc} is the solution of an integral equation, while u^0 is prescribed analytically. Therefore the incident field wave pulses obtained from the hybrid method serve as an exact reference.
The finite difference pulse on the other hand was excited below the canyon tip and has been propagated numerically through the grid. Furthermore the finite difference pulse energy maxima are systematically delayed, the delay increases with the travel distance of the pulses, whereas the onset of the pulses agree well. These phenomena can be explained by the dispersion and damping characteristic for discretization methods like the finite element and finite difference method (Boore, 1972; Alford et al., 1974; Smith, 1975; Kelly, 1976; Marfurt, 1984; Chin et al., 1984).

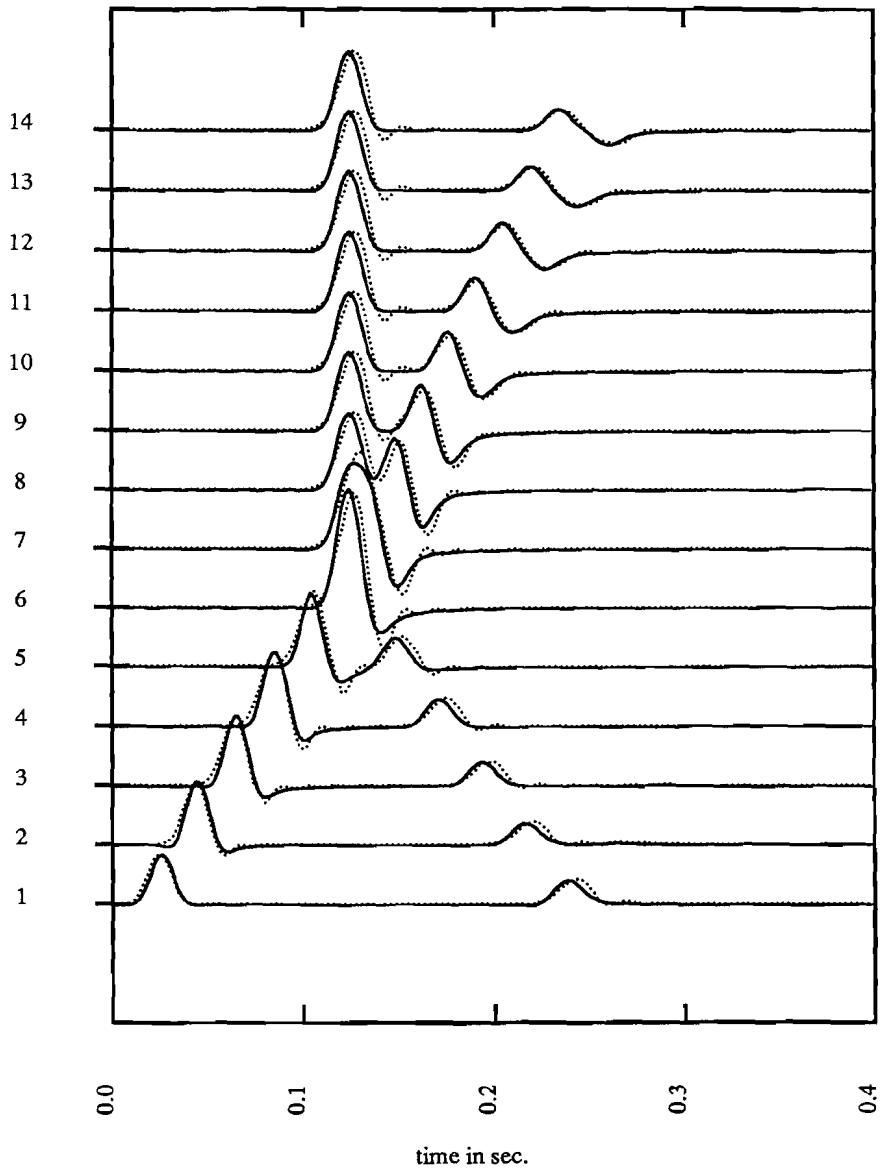

figure 6.25 Overlay plot of results of the hybrid method (solid lines) and finite difference results (dotted) for the receivers of fig. 6.26.

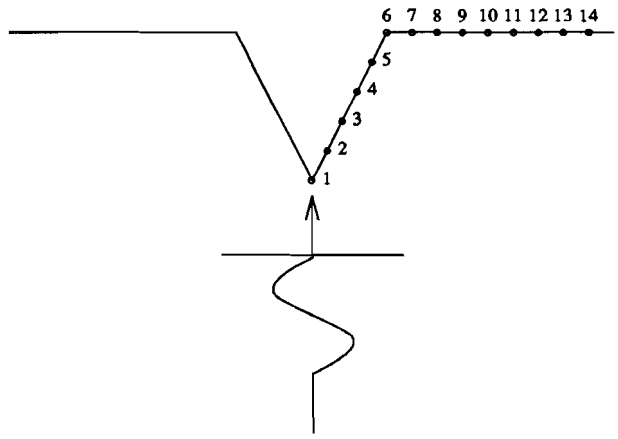

figure 6.26 Layout of the receivers (dots) for the hybrid method / finite difference method comparison, for the empty canyon model.

6.3.2. Effects of a low velocity sedimentary wedge on an incident wave

In this section the effect of a sedimentary wedge in the free surface of an otherwise homogeneous halfspace on an incident plane wave is modeled. This problem is relevant for the assessment of seismic risk of sites at or near low velocity fills. The modeling results also illustrate the complicating effect of low velocity fills on the waveform signal registered in a receiver located near such a structure. This effect may complicate the interpretation of recorded seismograms and as such it is important both in global seismology and seismic exploration. Kelly has studied the effect of similar surface structures on Love waves in a horizontally layered halfspace, using a finite difference method (Kelly, 1983).

The geometry of the model of the medium is the same as in section 6.3.1. It consists of a triangular indentation in a halfspace boundary 300 m wide and deep, see figure 6.27. The indentation is filled with low velocity material β=1500 m/s , ρ=2225 kg/m^3. The material parameters in the halfspace are the same as in the previous section ρ=2750 kg/m^3 , β=3000 m/s. The frequency range of the computations was defined as in 6.3.1, $f_i = i \times \Delta f$, $i = 1, \cdots, 75$, $\Delta f = 1$. Hz.

The triangular fill was discretized with a regular grid of 861 nodal points - 41 points along all three sides - and 1600 triangular elements with piecewise linear interpolation. The elements were geometrically similar to the shape of the fill, with heigth and width

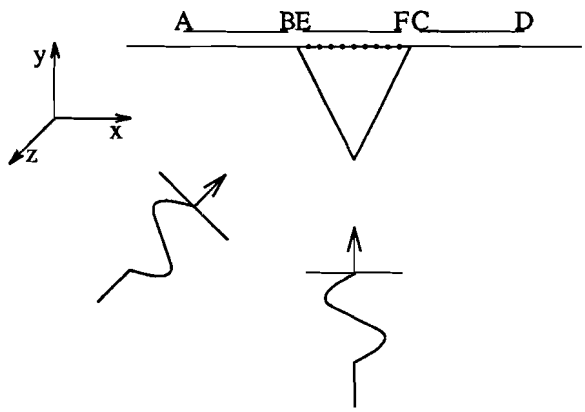

figure 6.27 Model configuration, plane waves - normal vectors in the x ,y plane - incident on triangular low velocity fill in a halfspace, with axis parallel to the z axis. Three line arrays of receivers - AB,EF,CD - are used. Dots denote null field points at the surface of the fill.

equal to $h = 7.5$ m. For waves of 75 Hz in the low velocity fill, this results in a number of elements per wave length, $\nu = \lambda/h = 2.67$. Using this discretization, the previously mentioned number of 10 elements per wavelength inside the low velocity fill reduces the admissible frequency band of the seismic signals to $f_{10} = \beta/(10\,h) = 20$ Hz , h=7.5 m.

As in 6.3.1 two incident waves of incident angles 45^0 and 0^0 were used as input. The same two receiver arrays as in 6.3.1 (AB, CD in figure 6.27.) were used. A third array of sensors, spaced at 7.5 m intervals was located along the surface of the fill, coinciding with the free surface points of the finite element grid (figure 6.27). Including the two boundary edge points of the wedge, the total number of equidistant receivers is 121. Displacement amplitude spectra for the 121 receivers are plotted versus the horizontal coordinate x in figure 6.28a for a plane wave incident at 45^0 and in figure 6.28b for the vertical incidence case.

Note that the amplification effects are stronger than in the previous case of the empty canyon, figure 6.22a,b. For the oblique incidence case, figure 6.28a a strong amplification occurs at the far side of the fill. For the vertical incidence case, figure 6.28b there is a pronounced focusing of energy in the center of the fill.

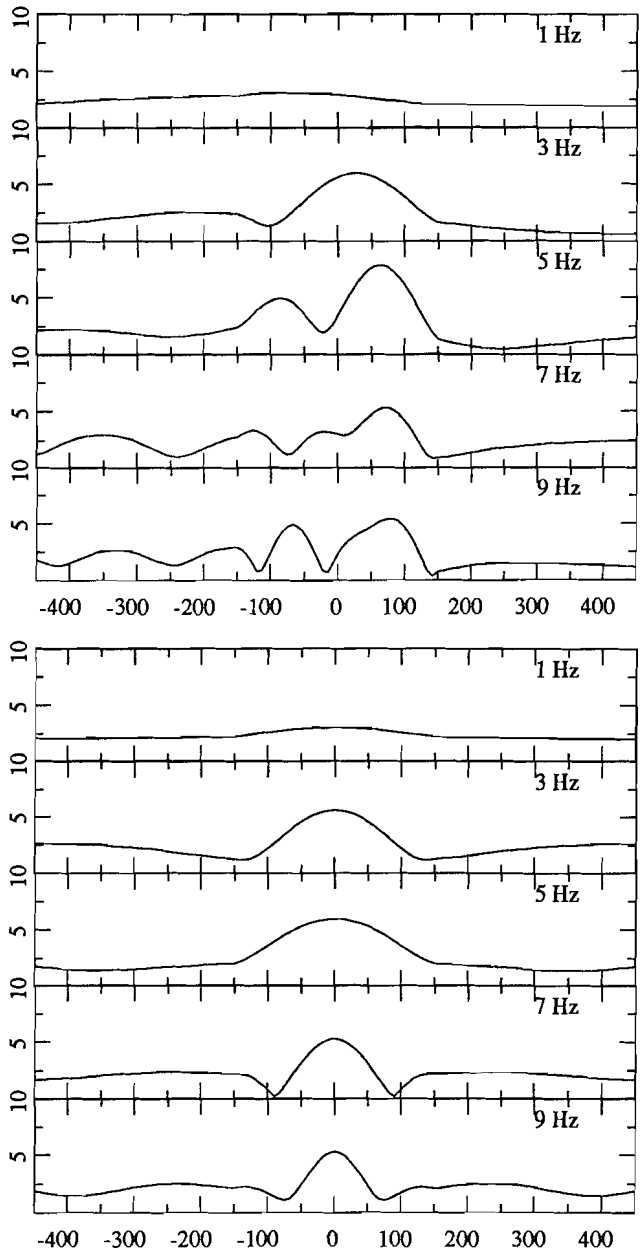

figure 6.28a,b Displacement amplitude versus x, for frequencies 1,3,5,7,9 Hz. Notice the vertical scale difference of a factor 2 with fig. 6.22ab. Receivers along the free surface of the halfspace and the sediment fill. a) top : oblique incidence. b) bottom: vertical incidence.

Using the signal waveform filter displayed in figure 6.23, the computed frequency spectra were transformed to the time domain. Figures 6.29a,b display the resulting time traces for the same set of receivers as in figures 6.24a,b, along the free surface and the walls of the fill. The figures correspond to incidence angles of 45^0 and 0^0 respectively. Comparing figure 6.29a and figure 6.24a one can see the same features. Strong primary arrivals on the left-hand side of the model, corresponding to the incident plane wave and its reflection from the left-hand side wall of the triangle (traces 1-41). Note that the reflected wave in figure 6.29a is weaker than the one in 6.24a since the reflection coefficient of the filled wedge is now smaller than one (the reflection coefficient of a plane SH wave at a free boundary). The diffracted waves originating from the tip of the triangle are much weaker in figure 6.29a than in 6.24a because of the smaller contrast at the tip for the filled wedge. The wave diffracted from the tip along the right hand side wall into the shadow zone is followed in figure 6.29a by a wave traveling at a lower speed, inside the wedge fill.

Similar observations can be made from figure 6.24b and 6.29b. Later arrivals in figures 6.29a,b clearly show some dispersive signals that can be attributed to the increasing effect of the numerical grid dispersion for the higher frequencies in the bandwidth on the later arrivals, that have traversed a longer path length through the grid. Note for instance the oscillatory late arrivals near trace 120 of figure 6.29a,b.

Spectral analysis of the oscillatory arrivals shows a concentration of energy in the frequency interval (30,50) Hz. For the wave velocity of 1500 m/s and an element size h=7.5 m, this frequency range corresponds to a grid density range of (6.67,4.29) elements per wavelenght. Dispersion curves for plane waves in a homogeneous unbounded medium, for several finite element discretizations - different element types and mass matrices - have been presented by Belytschko et al (1978) and by Marfurt (1984). For the constant strain elements and mass matrix defined in chapter 3, in the frequency domain formulation used here, dispersion curves are given in (Marfurt, 1984). Both phase and group velocity curves show a rapid decrease for $\nu = \lambda/h < 8$ (number of elements per wavelength) or equivalently $f > 25$ Hz, which explains the arrivals of dispersive oscillatory wave trains.
Reducing the bandwidth of the computed response with $f_{max} \approx 30$ Hz will eliminate the spurious arrivals. To this end the wave form filter defined in figure 6.4 with an effective bandwidth less than 30 Hz was applied to the data. The results are displayed in figure 6.29c,d for incidence angles 45^0 and 0^0.
Comparing figure 6.29a with 6.29c and figure 6.29b with 6.29d, one can see that the main features have remained unchanged, apart from a decreased resolution in time all individual phases present in figures 6.29a,b can be identified in 6.29c,d. The spurious oscillations however have been removed.

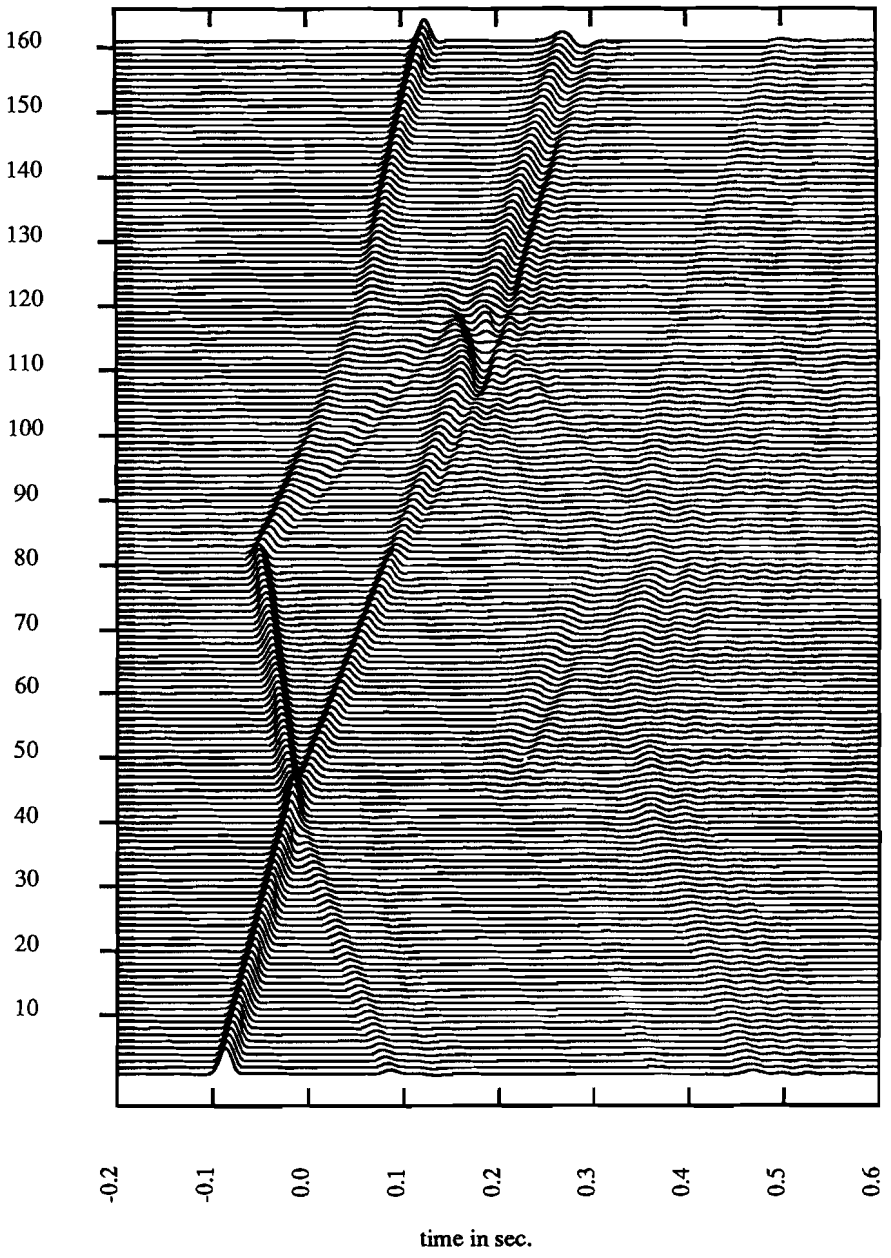

figure 6.29a Time domain displacement field along the walls of the fill (traces 41-121) and the surface of the halfspace (traces 1-40,122-161) - oblique incidence.

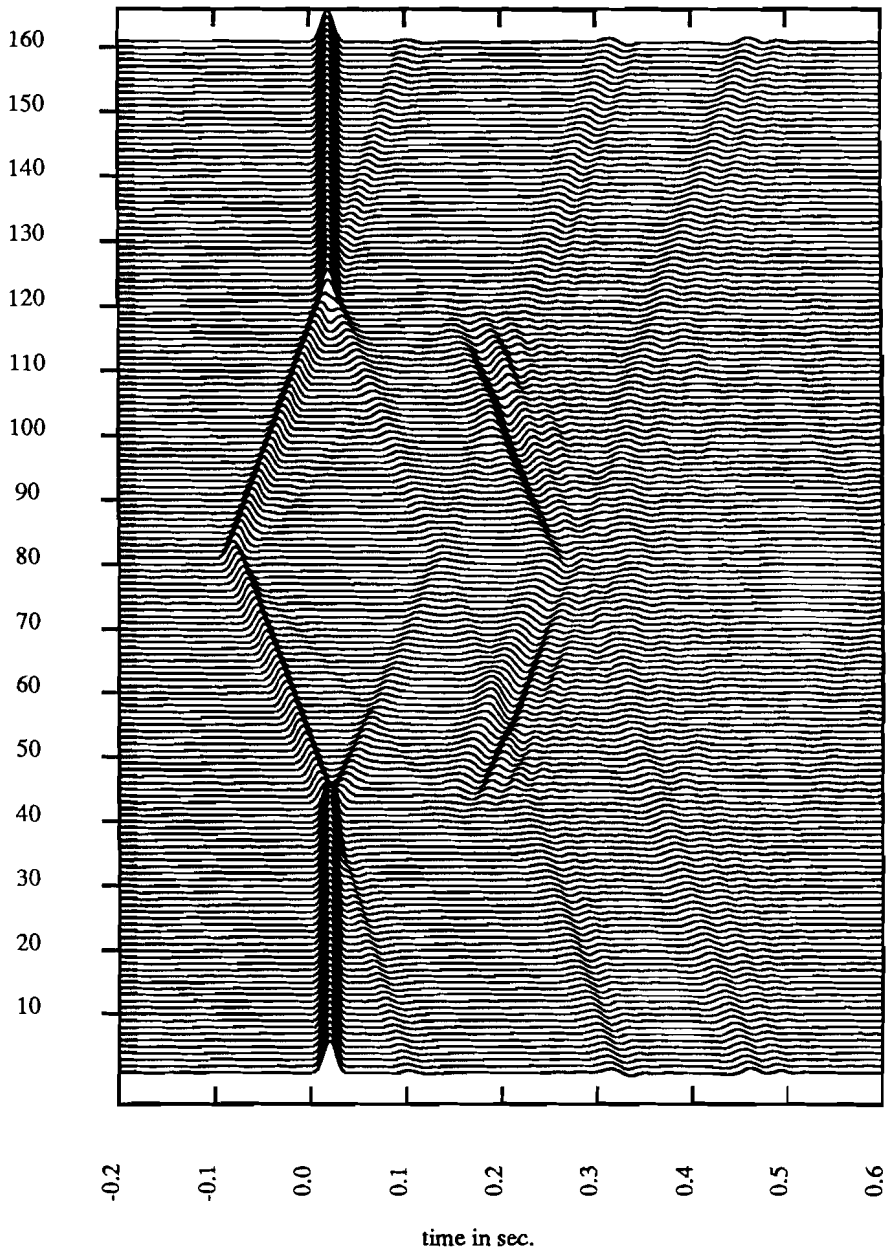

figure 6.29b Time domain displacement field along the walls of the fill (traces 41-121) and the surface of the halfspace (traces 1-40,122-161) - vertical incidence.

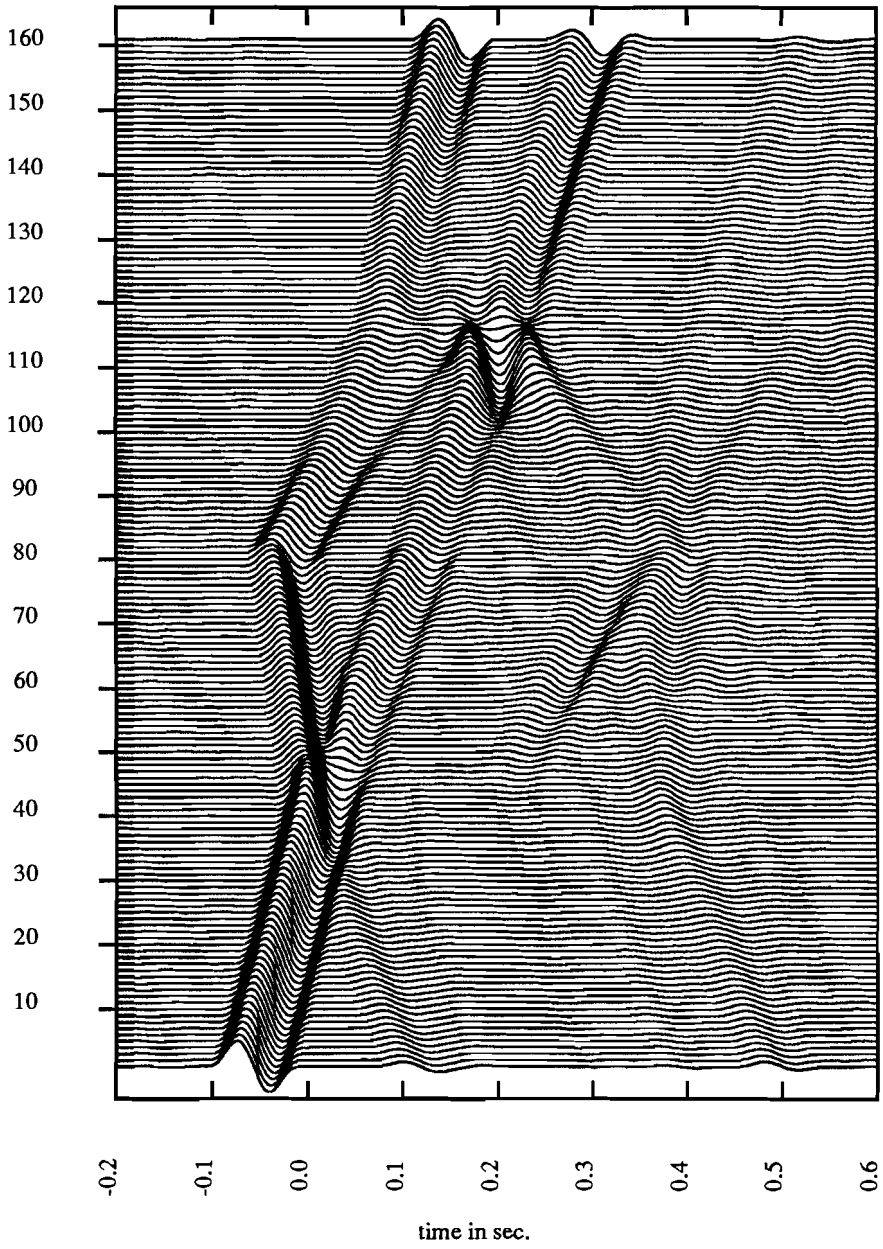

figure 6.29c Low pass filtered displacement field along the walls of the fill (traces 41-121) and the surface of the halfspace (traces 1-40,122-161) - oblique incidence.

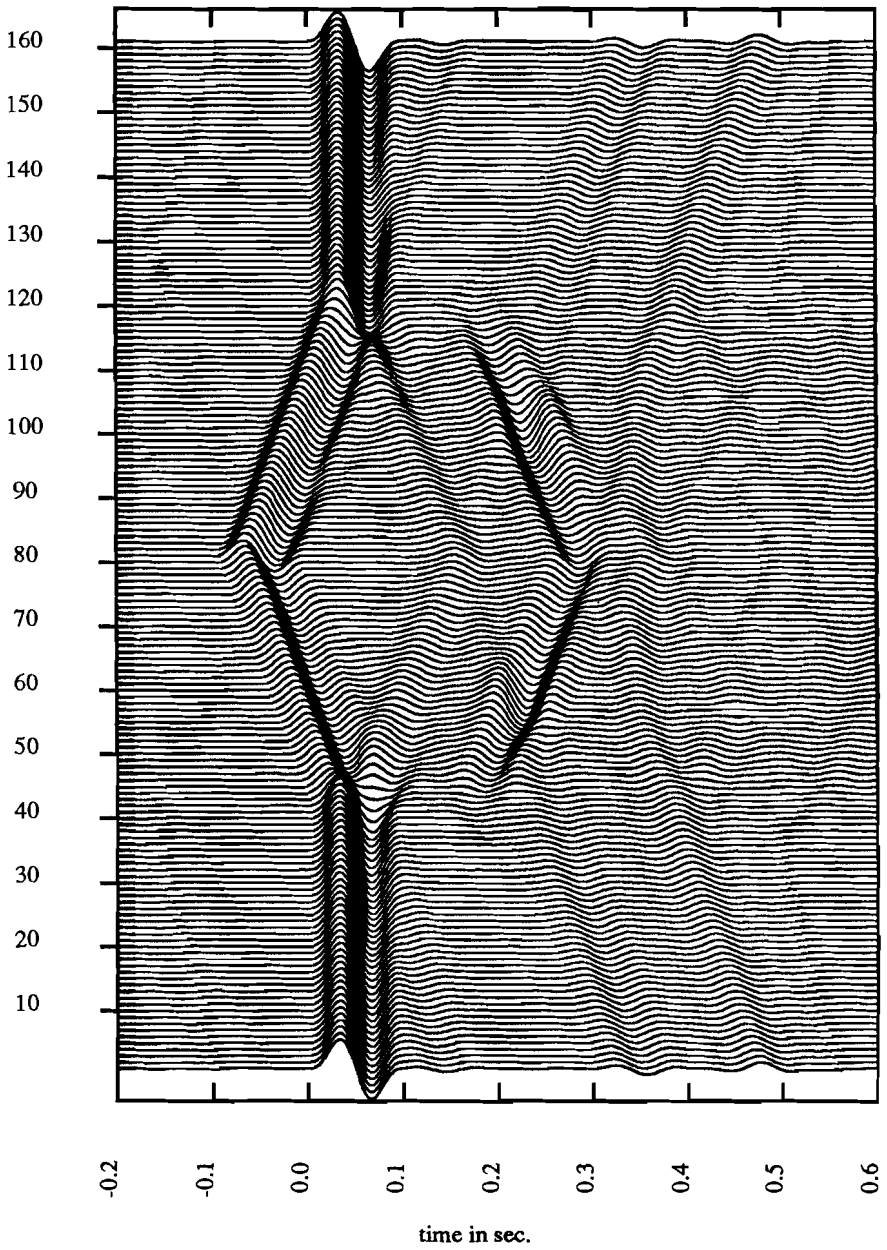

figure 6.29d Low pass filtered displacement field along the walls of the fill (traces 41-121) and the surface of the halfspace (traces 1-40,122-161) - vertical incidence.

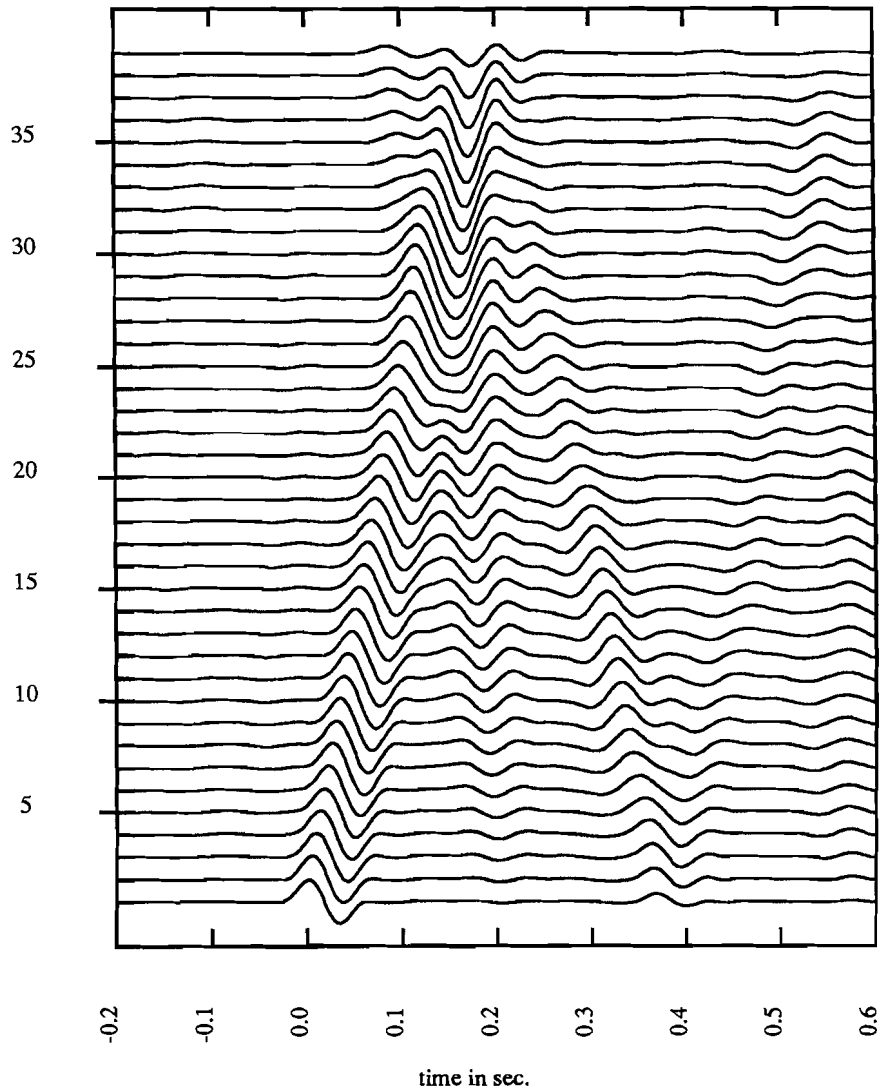

figure 6.30a Low pass filtered displacement field in the array EF (fig. 6.27) along the free surface of the fill - oblique incidence.

Figures 6.30a,b display the response along the free surface of the fill (array EF). The same low pass filter as in figures 6.29c,d has been applied to the data. Note the primary arrivals in traces 32-39 of figure 6.30a, that correspond to waves diffracted around the tip of the wedge that leaked into the fill through the right-hand side wall.
Some of the phases in the sections of figures 6.30a,b allow a ray-geometrical interpretation. Note the wave that traverses the fill from left to right, starting at trace 1 of figure 6.30a at $t \approx 0$, then in the opposite direction arriving on trace 1 at $t \approx .35$.

The second arrival on traces 1-20 of figure 6.30a (symmetric in the offset direction) corresponds to a diffraction of the incident wave at the tip of the fill. The arrival time of the incident wave at the origin of an undisturbed halfspace is $t = 0$. Figure 6.30b (vertical incidence) shows primary arrivals, corresponding to waves refracted into the low velocity fill.

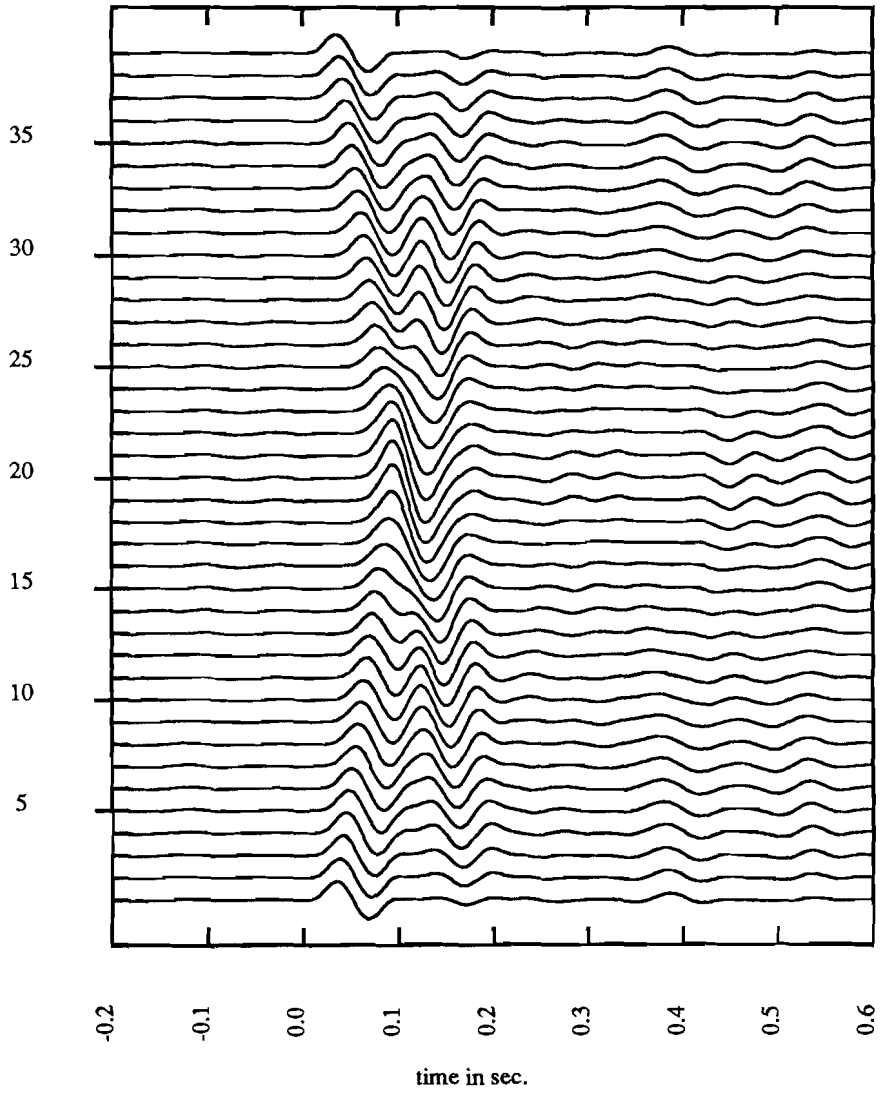

figure 6.30b Low pass filtered displacement field in the array EF (fig. 6.27) along the free surface of the fill - vertical incidence.

A comparison was made for a small number of receivers and a short time window with corresponding finite difference results (Zahradnik ,1978,1984). The original filter of figure 6.23 was applied, retaining the complete frequency band available (0,75) Hz. The locations of the receivers at the free surface are depicted in figure 6.31.

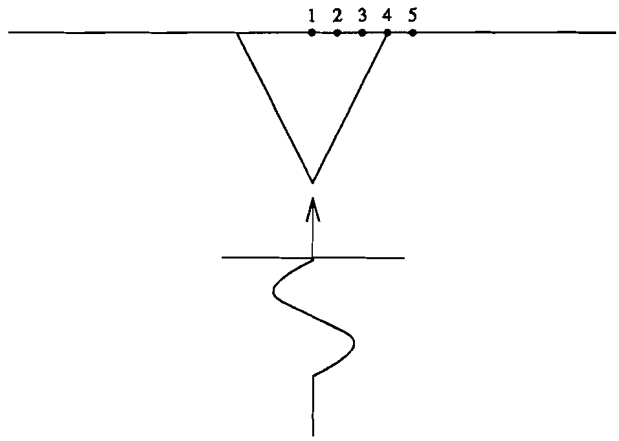

figure 6.31 Layout of the receivers (dots) for the hybrid method / finite difference method comparison (fig. 6.32).

An overlay plot of the results is shown in figure 6.32. For the receivers inside the fill the results of both methods have suffered dispersion. In the top two traces only the finite difference results display the dispersion effect. Apart from these small differences the results agree well.

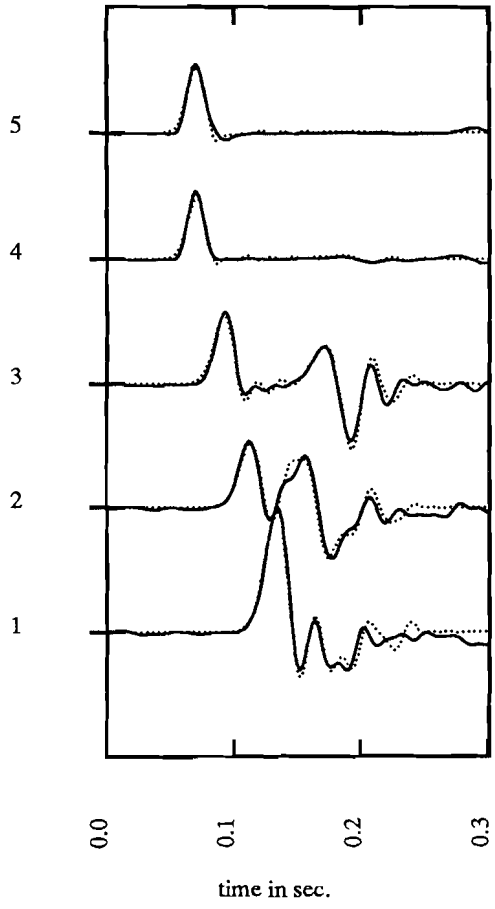

figure 6.32 Overlay plot of results of the hybrid method (solid lines) and finite difference results (dotted) for the receivers of fig. 6.31.

Chapter 7

CONCLUSIONS

The hybrid finite element / boundary integral equation method presented in this thesis has a number of advantages over pure discretization methods such as the finite element and finite difference method, namely

(1) Only the anomalous region has to be discretized. The background medium effects are accounted for by the integral representation. This greatly reduces the computer memory required by the program. It also eliminates the effects of numerical dispersion caused by a discretization of the background medium.
This was clearly demonstrated in the comparison with finite difference results for the canyon model in section 6.3.1.

(2) Because we do not have to truncate the model, as in a pure discretization method, there are no artificial boundary effects such as spurious reflections to be dealt with.

(3) A greater flexibility in the wave field excitation of the model is available, because one can either include a source in the discretized part of the model, using the finite element formalism or formulate the response in terms of an incident wave field in the back ground medium, using the integral representation.

(4) A greater flexibility is provided in modeling experiments. The computation of the model response can be split up in several independent stages as described in appendix D. Thus one can change part of the modeling parameters and obtain new results for the modified configuration, without repeating all the initial calculations. This makes modeling experiments with a trial an error strategy or parameter estimation using non-linear optimization techniques more feasible.

It has been shown, that the numerical inaccuracies in the computed results for the characteristic frequencies of the scattering obstacle, related to the type of integral equation used, can be effectively eliminated using a small number of additional null field equations.
The implementation for 2-D scalar problems has been applied in the computation of the response of a number of models, including different types of wave field excitations.
In section 6.1 results for a model with a smooth boundary were shown to agree well with a series solution for the same model. It was also shown, from an analysis of the frequency dependence of the error in the solution, that - for the given type of finite elements used and a predominant frequency at 1/3 of the bandwidth ($f_d \approx 1/3 f_{max}$) a number of 10 elements per wavelength at the maximum frequency f_{max} gives excellent results.

In section 6.3 results for a model containing boundary edges agreed favorably with independent results from a finite difference method. Velocity dispersion, well known for finite element and finite difference solutions was observed. It was shown, that the dispersion effects were eliminated by application of a low pass filter, that increases the number of elements per wavelength at the maximum frequency f_{max} to 8. This agrees with discretization criteria for full discretization methods (Alford et al.,1974 ; Smith,1975) It can be concluded, that the discretization requirements for the finite element part of the hybrid method are the same as those for a full discretization method.
It has been shown in the modeling experiments, that Schenck's method of additional null field equations gives good results for the range of wave numbers ($ka < 10$) studied.

The results presented are for the simple case of 2-D scalar wave propagation with a homogeneous background medium. Possible future developments include,

(1) Extension of the implementation to the P-SV case. This would allow modeling PS and SP conversions in the medium.

(2) Implementation of more general background media, such as a horizontally layered medium. This would allow the non-linear analysis of surface waves in laterally varying media.

(3) Extension to the 3-D case. This is essential for the study of the effects of incident waves on 3-D structures, such as for example buildings and off-shore constructions.

Appendix A

APPROXIMATION OF A VECTOR FIELD BY MEANS OF INTERPOLATION

In both the finite element and the integral equation formulation of the elastodynamic problem, the displacement vector field can be approximated using interpolation. Let $\mathbf{u}$ be a vector field defined on a domain $V \in \mathbf{R}^n$.
Define a space grid $\mathbf{G}$ in V as a set of N connected nodal points,
$\mathbf{x}_M \in \mathbf{R}^n$, $M=1,2,\cdots,N$, $n=1,2,3$.

$$\mathbf{G} = \bigcup_M \mathbf{x}_M$$

The nodal points of the space grid can be connected by straight lines in such a way, that for the induced division in to open space elements $\mathbf{e}_K$ we have

$$\mathbf{e}_K \cap \mathbf{e}_J = \emptyset \ , K \neq J$$

Closing the elements - including the element boundaries - we will have

$$V' = \bigcup_K \bar{\mathbf{e}}_K$$

Where the volume V' will approximate V in a manner depending on the choice of the grid $\mathbf{G}$. In the following I will drop the distinction between V and V', assuming that in particular, ∂V can be built up from a finite number of plane segments (in $\mathbf{R}^3$) or straight line segments (in $\mathbf{R}^2$).

Define scalar interpolating functions $\phi_M(\mathbf{x}) \in \mathbf{R}$ in a piece wise manner on the elements of V, so that

$$\begin{aligned} \phi_M(\mathbf{x}_J) &= \delta_{MJ} \quad , \mathbf{x}_J \in \mathbf{G} \\ \phi_M(\mathbf{x}) &= 0 \quad , \mathbf{x} \notin s(\phi_M) \\ \phi_M(\mathbf{x}) &= f_K(\mathbf{x}) \quad , \mathbf{x} \in \bar{\mathbf{e}}_K \ , \bar{\mathbf{e}}_K \subset s(\phi_M) \end{aligned} \tag{A.1}$$

where δ_{MJ} is the Kronecker delta symbol and $f_K(\mathbf{x})$ is an interpolating function defined on $\mathbf{e}_K$, and the support $s(\phi_M)$ of the function $\phi_M(\mathbf{x})$ is defined as the union of all (closed) elements, that contain the nodal point $\mathbf{x}_M \in \mathbf{G}$.
The second property of (A.1) implies, that the interpolating functions are local, i.e they are zero outside a support of finite extent.

As a consequence most matrix elements occurring in the coefficient matrices of the finite element treatment in chapter 3 are zero, because they can be expressed as integrals of products of the interpolating functions, these matrices are sparse.

In the following interpolated quantities will be denoted with an over bar. With (A.1) we can define a piecewise interpolating expression for a complex scalar field $w(\mathbf{x})$ on V

$$\bar{w}(\mathbf{x}) = \sum_{M=1}^{N} w(\mathbf{x}_M)\phi_M(\mathbf{x}) \tag{A.2}$$

Figure A.1 shows an example of an interpolating function $\phi_M(\mathbf{x})$ on a two dimensional region divided in triangular elements.

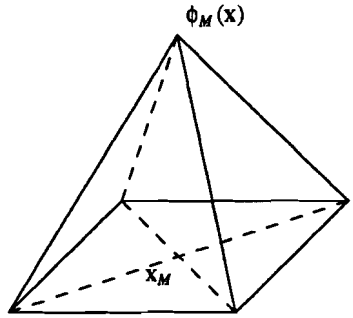

figure A.1 Piece wise linear interpolating function ϕ_M on a regular 2-D grid

The displayed function is defined piece wise and is of first order. Examples of higher order interpolating functions and elements different from the triangular ones in figure A.1 can be found in (Zienkiewicz, 1977).

Using (A.2) with triangular elements and piece wise linear interpolation, the real and imaginary parts of a complex scalar field on $\mathbf{R}^2$, represented by smooth surfaces in three dimensional space will be replaced by surfaces coinciding with the smooth surfaces in the nodal points $\mathbf{x}_M$, and built up of planar triangles.

As for scalar fields we can interpolate a vector field component wise

$$\bar{u}_i(\mathbf{x}) = \sum_{M=1}^{N} u_i(\mathbf{x}_M)\phi_M(\mathbf{x}) \tag{A.3}$$

or using a matrix notation

$$\bar{\mathbf{u}}(\mathbf{x}) = \mathbf{\Phi}(\mathbf{x})\mathbf{U}$$

where

$$\bar{\mathbf{u}}(\mathbf{x}) = (\bar{u}_1(\mathbf{x}), \bar{u}_2(\mathbf{x}), \bar{u}_3(\mathbf{x}))^{\mathrm{T}}$$

and

$$\Phi(\mathbf{x}) = \begin{bmatrix} \phi_1(\mathbf{x}) & 0 & 0 & \cdots & \phi_N(\mathbf{x}) & 0 & 0 \\ 0 & \phi_1(\mathbf{x}) & 0 & \cdots & 0 & \phi_N(\mathbf{x}) & 0 \\ 0 & 0 & \phi_1(\mathbf{x}) & \cdots & 0 & 0 & \phi_N(\mathbf{x}) \end{bmatrix} \tag{A.4}$$

Φ is a $d \times dN$ matrix, with d the number of components of the vector field, (d =3 in (A.4)) and

$$\mathbf{U} = (U_1, U_2, \cdots, U_{dN})^{\mathrm{T}}$$

is the dN vector of multiplexed nodal point values of the vector field.
In general for a vector field with d components we have

$$U_{d(I-1)+i} = u_i(\mathbf{x}_I) \tag{A.5}$$

Defining the K^{th} column vector in Φ as $\Phi_K = (\Phi_{1K}, \cdots, \Phi_{dK})^{\mathrm{T}}$ we have for (A.3),

$$u_i(\mathbf{x}) = \sum_{K=1}^{dN} \Phi_{iK}(\mathbf{x}) U_K \tag{A.6}$$

The dN column vectors are linear independent elements of a linear space over $\mathbf{C}$ (the complex numbers) of vector fields on V. This can be shown as follows; let

$$\mathbf{I}(\mathbf{x}) = \sum_{K=1}^{dN} A_K \Phi_K(\mathbf{x}) = \mathbf{0} \tag{A.7}$$

with scalar coefficients A_K.
The Φ_k are independent if (A.7) implies $A_K = 0$, K=1, $\cdots$, dN (Mostow,Sampson and Meyer, 1963).

We can identify

$$A_K = a_i(\mathbf{x}_J), K = d(J-1)+i$$

and considering a single component of (A.7) and rearranging into a sum over the nodal point contributions

$$I_i(\mathbf{x}) = \sum_{J=1}^{N} a_i(\mathbf{x}_J)\phi_J(\mathbf{x}), \; i = 1, \cdots, d$$

and using (A.1)

$$I_i(\mathbf{x}_M) = \sum_{J=1}^{N} a_i(\mathbf{x}_J)\phi_J(\mathbf{x}_M) = \sum_{J=1}^{N} a_i(\mathbf{x}_J)\delta_{JM}$$

$$= a_i(\mathbf{x}_M) = A_L = 0\,,\; i = 1,2,3\;\;,\; L = d(M-1)+i = 1,2,\cdots,dN$$

so that the Φ_K are linear independent. The dN independent column vectors Φ_K span a dN dimensional subspace $\mathbf{B}^h$ of vector fields on V.

In the hybrid method presented in this thesis, the wave field is approximated using interpolation on a space grid. A solution of the field equation is then constructed within the subspace $\mathbf{B}^h$, that satisfies both Galerkin's principle for the elastodynamic equation (see chapter 3) and the discretized integral equation (see chapter 4).

Appendix B

DERIVATION OF THE BOUNDARY INTEGRAL REPRESENTATION

1. A representation theorem for the elastodynamic field

The integral equation used in the present hybrid method is related to the classical Betti-Rayleigh relation of elastodynamics (Kupradze, 1956,1963; De Hoop, 1958; Tan, 1975a; Ben-Menahem and Singh, 1981).
In order to clarify the notation used and to provide a basis for applications in other chapters we will give a short derivation of the classical results.
Let $\{u_i^{A,B},\tau_{ij}^{A,B}\}$ be two elastodynamic states, satisfying the elastodynamic equation in the region V_R, see figure B.1.

$$-\partial_j \tau_{ij}^{A,B} - \rho\omega^2 u_i^{A,B} = f_i^{A,B} \tag{B.1}$$

Then we may evaluate the form

$$f_i^B u_i^A - f_i^A u_i^B = \partial_j (u_i^B \tau_{ij}^A - u_i^A \tau_{ij}^B) + (\tau_{ij}^B \partial_j u_i^A - \tau_{ij}^A \partial_j u_i^B) \tag{B.2}$$

For a linearly elastic medium we have for the stress tensor $\tau_{ij}=c_{ijpq}\,\varepsilon_{pq}$ where the strain tensor ε_{pq} is defined as

$$\varepsilon_{pq}=1/2(\partial_p u_q+\partial_q u_p)$$

Using the symmetry of both stress and strain tensors, the last two terms in (B.2) can be rewritten,

$$\tau_{ij}^A \partial_j u_i^B = \varepsilon_{pq}^A c_{ijpq} \varepsilon_{ij}^B \tag{B.3}$$

Substitution of the symmetry relation $c_{ijpq}=c_{pqij}$ (Aki and Richards, 1981), shows that (B.3) is symmetric in A and B so the last term in brackets in (B.2) will vanish.
Integrating (B.2) over the volume V_R-V - see figure B.1 - and applying the Gauss divergence theorem we get the Betti-Rayleigh theorem

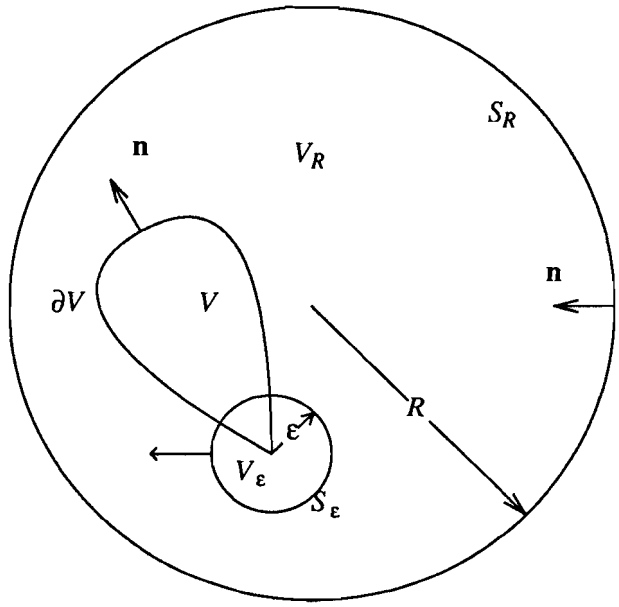

figure B.1 Spherical domain V_R of the integral representation with an embedded scatterer V, and a small sphere of radius ε surrounding a point on the boundary surface ∂V.

$$\int_{V_R-V} (f_i^B u_i^A - f_i^A u_i^B) dV = \tag{B.4}$$

$$-\int_{\partial V} (u_i^B \tau_{ij}^A - u_i^A \tau_{ij}^B) n_j \, dA - \int_{S_R} (u_i^B \tau_{ij}^A - u_i^A \tau_{ij}^B) n_j \, dA$$

where the normal vector $\mathbf{n}$ is the inward normal of the volume $V_R - V$.
The representation theorem follows from (B.4) when the fields A and B are specified by

$$A) \quad -\partial_j \tau_{ij}^k(\mathbf{x},\mathbf{x}_p) - \rho\omega^2 u_i^k(\mathbf{x},\mathbf{x}_p) = \delta_{ik}\delta(\mathbf{x}-\mathbf{x}_p) \tag{B.5}$$

$$B) \quad -\partial_j \tau_{ij}(\mathbf{x}) - \rho\omega^2 u_i(\mathbf{x}) = f_i(\mathbf{x}) \tag{B.6}$$

where δ_{ik} is the Kronecker delta symbol and $\delta(\mathbf{x})$ is the Dirac delta function in three dimensional space.
The elastodynamic state $\{u_i^k, \tau_{ij}^k\}$ is the Green's state of the medium, the field excited

by a single force in the direction of the k axis, concentrated in $\mathbf{x}_p$.
The contribution from the surface S_R to the surface integral in (B.4) can be shown to vanish in the limit $R \to \infty$ when the Green's state represents a diverging wave and a radiation condition is imposed on the unknown field, prescribing the asymptotic behaviour at large distances. Proofs are given by Kupradze (1963) and Tan (1975a).
Substitution of (B.5) and (B.6) into (B.4) and assuming that a radiation condition holds, we have

$$\oint_{\partial V} (\tau_{ij}^k u_i - u_i^k \tau_{ij}) n_j \, dA + \int_{V_R - V} u_i^k f_i \, dV = \begin{cases} 0 & , \mathbf{x}_p \in V \\ c_i^k(\mathbf{x}_p) u_i(\mathbf{x}_p) & , \mathbf{x}_p \in \partial V \\ u_k(\mathbf{x}_p) & , \mathbf{x}_p \in V_R - V \end{cases} \quad \text{(B.7a,b,c)}$$

In case $\mathbf{x}_p \in \partial V$, the Green's state kernels of the surface integral are singular and the surface integral is defined by its Cauchy principal value.
In the application of Gauss' theorem, the volume $V_R - V$ - containing the singular point $\mathbf{x}_p$ - is replaced by the volume $V_R - V - V_\varepsilon$, where V_ε is the intersection of a small sphere of radius ε centered in $\mathbf{x}_p$ and the exterior domain $V_R - V$ - see figure B.1. The surface integral is then taken over the surface ∂V, minus the part cut off by the ε sphere - defining the the Cauchy principal value - and the surface S_ε of V_ε, with normal vector pointing into $V_R - V - V_\varepsilon$.
Kupradze (1963) has shown the limiting value

$$\lim_{\varepsilon \to 0} \int_{S_\varepsilon} u_i^k(\mathbf{x}, \mathbf{x}_p) dA$$

to be zero.
The term $c_i^k(\mathbf{x}_p)$ in (B.7b) is the finite contribution of the singular stress term $\tau_{ij}^k(\mathbf{x}, \mathbf{x}_p)$, integrated over S_ε, in the limit $\varepsilon \to 0$.

$$\lim_{\varepsilon \to 0} - \int_{S_\varepsilon} \tau_{ij}^k(\mathbf{x}, \mathbf{x}_p) u_i n_j \, dA = \lim_{\varepsilon \to 0} - \int_{S_\varepsilon} \tau_{ij}^k(\mathbf{x}, \mathbf{x}_p) n_j \, dA \; u_i(\mathbf{x}_p) = c_i^k(\mathbf{x}_p) u_i(\mathbf{x}_p)$$

for a continuous displacement field $\mathbf{u}(\mathbf{x})$.
This defines the tensor $c_i^k(\mathbf{x}_p)$

$$c_i^k(\mathbf{x}_p) = \lim_{\varepsilon \to 0} - \int_{S_\varepsilon} \tau_{ij}^k(\mathbf{x}, \mathbf{x}_p) n_j \, dA \qquad \text{(B.8)}$$

For a locally smooth boundary it can be shown ∂V, $c_i^k(\mathbf{x}_p) = \frac{1}{2} \delta_{ik}$ (Kupradze, 1963).
For the general case, including non smooth boundaries we can derive an expression for the tensor $c_i^k(\mathbf{x}_p)$, independent of the frequency ω, that can be evaluated numerically, for a given boundary geometry.
To this end we split up the Green's state as in section 4.3 into a singular part and a regular part. For the singular part we take the Green's state of a homogeneous medium with the material parameters of the evaluation point. Only the singular part will contribute to the integral in (B.8).

Furthermore, Kupradze (1963) has shown, that the singular behaviour of the dynamic Green's state for a homogeneous medium is the same as for the static Green's state, $\{u_i^{0k},\tau_{ij}^{0k}\}$ or

$$c_i^k(\mathbf{x}_p) = \lim_{\varepsilon\to 0} -\int_{S_\varepsilon} \tau_{ij}^{0k}(\mathbf{x},\mathbf{x}_p)n_j dA$$

An expression for c_i^k can now be derived using a procedure comparable to one used in (Brebbia, 1978). Consider an arbitrary uniform displacement field $\mathbf{u}(\mathbf{x}) = \mathbf{a}$, $\tau_{ij}[\mathbf{u}] = 0$, this field satisfies the homogeneous elastostatic equation,

$$\partial_j \tau_{ij} = 0$$

We can substitute this field into the elastostatic counterpart of the integral equation (B.7b),

$$\oint_{\partial(V_R-V)} (\tau_{ij}^{0k}u_i - u_i^{0k}\tau_{ij})n_j dA + \int_{V_R-V} u_i^{0k} f_i dV = c_i^k(\mathbf{x}_p)u_i(\mathbf{x}_p) \ , \ \mathbf{x}_p \in \partial V \quad \text{(B.9)}$$

where $\{u_i^{0k},\tau_{ij}^{0k}\}$ is the elastostatic Green's state.
Because of the choice of the uniform displacement u_i in (B.9) there will be a finite contribution from the outer boundary S_R.
Substituting the uniform displacement field with $u_i = a_i$, $\tau_{ij} = 0$, $f_i = 0$ in (B.9) we have

$$\left\{ \oint_{\partial(V_R-V)} \tau_{ij}^{0k} n_j dA - c_i^k(\mathbf{x}_p) \right\} a_i = 0$$

and since a_i is arbitrary we have

$$c_i^k(\mathbf{x}_p) = \oint_{\partial(V_R-V)} \tau_{ij}^{0k} n_j dA = \oint_{\partial V} \tau_{ij}^{0k} n_j dA + \int_{S_R} \tau_{ij}^{0k} n_j dA \quad \text{(B.10)}$$

The contribution from S_R to (B.10) can be calculated directly

$$\int_{S_R} \tau_{ij}^{0k} n_j dA = -\int_{V_R} \partial_j \tau_{ij}^{0k} dV = \int_{V_R} \delta_{ik}\delta(\mathbf{x}-\mathbf{x}_p)dV = \delta_{ik} \quad \text{(B.11)}$$

where the normal vector $\mathbf{n}$ is defined pointing inward in V_R as in (B.4).
Substitution of (B.11) in (B.10) gives

$$c_i^k(\mathbf{x}_p) = \oint_{\partial V} \tau_{ij}^{0k} n_j dA + \delta_{ik} \quad \text{(B.12)}$$

The integral in the right-hand side of (B.12) can be evaluated numerically, using the

discretization procedure, introduced in section 4.2. Replacing the dynamic Green's state by its static counterpart, we define the static analogue of the frequency dependent matrix in (4.9)

$$\bar{B}_{IJ}^{0k} = \int_{\partial V} \tau_{ij}^{0k}(\mathbf{x},\mathbf{x}_I) n_j \Phi_{iJ}(\mathbf{x}) dA(\mathbf{x}) \tag{B.13}$$

Taking $\mathbf{x}_p = \mathbf{x}_I$ a boundary grid point and substituting (B.13) in (B.12) we have the approximate result

$$c_i^k(\mathbf{x}_I) \approx \sum_{J=1}^{dN_b} \bar{B}_{IJ}^{0k} + \delta_{ik} \tag{B.14}$$

The quantities c_i^k are completely defined by the model parameters and need to be calculated only once for a given model, independent of the frequency range of the wave propagation calculations in which they are used.

The integral equation (B.7b) can be used to solve for the wave field on the boundary of a scattering inclusion, either in combination with a finite element equation for the inclusion - see chapter 5 - or on its own in the decoupled problems of scattering by a rigid or void inclusion - see section 4.1.
Once the field on the boundary ∂V has been calculated, the field outside the inclusion can be obtained evaluating (B.7c), which propagates the boundary field into the surrounding medium.

2. Excitation by an incident wave field

In this section we will consider the case of a wave field excited by an incident wave in the absence of body forces. We will derive an inhomogeneous integral equation for the field on the boundary ∂V, where the inhomogeneous term will contain the incident wave field.
Tan derived a similar result for the case of obstacles with smooth boundaries (Tan, 1975a). We will consider the general case of non-smooth boundaries as encountered in the present hybrid method.
We split up the total wave field into an incident field $\mathbf{u}^0$, (which would be observed if no obstacle were present) and a scattered field $\mathbf{u}^{sc}$, caused by the presence of the scatterer, satisfying a radiation condition.

$$\mathbf{u} = \mathbf{u}^0 + \mathbf{u}^{sc} \tag{B.15}$$

The scattered field satisfies both the elastodynamic equation and a radiation condition therefore we can apply the representation theorem (B.7) to the scattered field on the volume $V_R - V$ and take the limit $R \to \infty$, $V_R \to V_\infty$.
In the following we will denote the Green's state for the medium inside V with the

suffix v and for the exterior medium with the suffix ∞.
Applying the representation theorem (B.7) to the scattered field on $V_\infty - V$, the exterior domain, we have

$$\oint_{\partial V} (\tau_{ij}^{k\infty} u_i^{sc} - u_i^{k\infty} \tau_{ij}^{sc}) n_j \, dA = \begin{cases} u_k^{sc}(\mathbf{x}_p) & , \mathbf{x}_p \in \mathbf{V}_\infty - \mathbf{V} \\ c_i^{k\infty} u_i^{sc}(\mathbf{x}_p) & , \mathbf{x}_p \in \partial \mathbf{V} \\ 0 & , \mathbf{x}_p \in \mathbf{V} \end{cases} \qquad \text{(B.16a.b.c)}$$

The term $c_i^{k\infty} u_i^{sc}(\mathbf{x}_p)$ results from the integration of the singular stress term $\tau_{ij}^{k\infty}$ over the part of the surface of an infinitesimal sphere S_ε^∞ centered at $\mathbf{x}_p$, with an outward pointing normal vector, that is exterior to V (figure B.2).

$$c_i^{k\infty} = \lim_{\varepsilon \to 0} - \int_{S_\varepsilon^\infty} \tau_{ij}^{\infty} n_j \, dA \qquad \text{(B.17)}$$

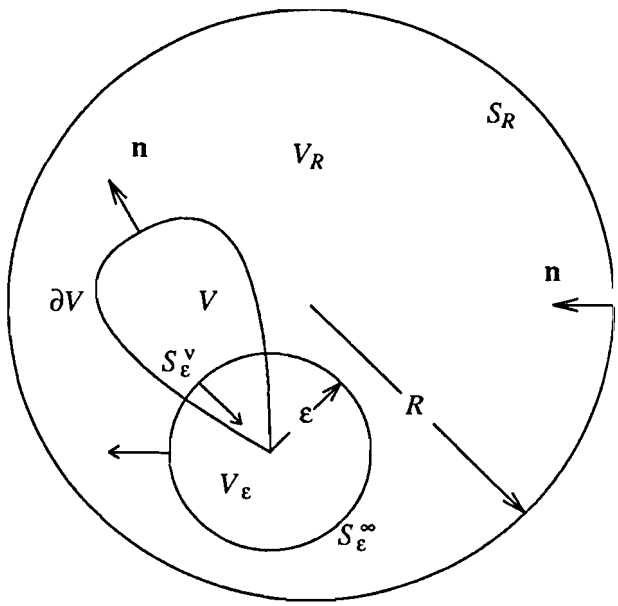

figure B.2 Spherical domain V_R of the integral representation with an embedded scatterer V, and a small ε sphere surrounding a point on the boundary surface ∂V, divided in S_ε^v (inside V) and S_ε^∞ (outside V).

Next we apply the representation theorem to the incident field $\mathbf{u}^0$ on the volume V, using the Green's state for the exterior medium.
This reflects the definition of the incident field as the field observed in the absence of the obstacle.

$$-\oint_{\partial V}(\tau_{ij}^{k\infty}u_i^0-u_i^{k\infty}\tau_{ij}^0)n_j\,dA=\begin{cases}0 & ,\mathbf{x}_p\in\mathbf{V}_\infty-\mathbf{V}\\ -c_i^{kv}u_i^0(\mathbf{x}_p) & ,\mathbf{x}_p\in\partial\mathbf{V}\\ u_k^0(\mathbf{x}_p) & ,\mathbf{x}_p\in\mathbf{V}\end{cases}\qquad\text{(B.18a,b,c)}$$

The term $c_i^{kv}u_i^0(\mathbf{x}_p)$ in (B.18b) results from integrating the singular stress term $\tau_{ij}^{k\infty}$ over the part S_ε^v of the spherical surface with radius ε, centered at $\mathbf{x}_p$, with inward pointing normal vector, that is interior to V (figure B.2).

$$c_i^{kv}(\mathbf{x}_p)=\lim_{\varepsilon\to0}-\int_{S_\varepsilon^v}\tau_{ij}^{k\infty}n_j\,dA\qquad\text{(B.19)}$$

Subtracting (B.18) from (B.16), we get

$$\oint_{\partial V}(\tau_{ij}^{k\infty}u_i-u_i^{k\infty}\tau_{ij})n_j\,dA=\begin{cases}u_k^{sc}(\mathbf{x}_p) & ,\mathbf{x}_p\in\mathbf{V}_\infty-\mathbf{V}\\ c_i^{k\infty}u_i^{sc}(\mathbf{x}_p)+c_i^{kv}u_i^0(\mathbf{x}_p) & ,\mathbf{x}_p\in\partial\mathbf{V}\\ -u_k^0(\mathbf{x}_p) & ,\mathbf{x}_p\in\mathbf{V}\end{cases}\qquad\text{(B.20a,b,c)}$$

Using (B.15), the right hand side of (B.20b) becomes

$$c_i^{k\infty}u_i-(c_i^{k\infty}-c_i^{kv})u_i^0=c_i^{k\infty}u_i-c_i^{k\varepsilon}u_i^0$$

where

$$c_i^{k\varepsilon}=\lim_{\varepsilon\to0}-\int_{S_\varepsilon}\tau_{ij}^{k\infty}n_j\,dA$$

is a surface integral over the closed sphere S_ε with outward pointing normal vector.
It can be shown, that $c_i^{k\varepsilon}(\mathbf{x}_p)=\delta_{ik}$ (Kupradze, 1963).
This results in the integral representation describing the excitation by an incident wave field.

$$\oint_{\partial V}(\tau_{ij}^{k\infty}u_i-u_i^{k\infty}\tau_{ij})n_j\,dA=\begin{cases}u_k^{sc}(\mathbf{x}_p) & ,\mathbf{x}_p\in\mathbf{V}_\infty-\mathbf{V}\\ c_i^{k}u_i(\mathbf{x}_p)-u_k^0(\mathbf{x}_p) & ,\mathbf{x}_p\in\partial\mathbf{V}\\ -u_k^0(\mathbf{x}_p) & ,\mathbf{x}_p\in\mathbf{V}\end{cases}\qquad\text{(B.21a,b,c)}$$

Appendix C

A SOLUTION FOR THE NON-UNIQUENESS PROBLEMS FOR THE INTEGRAL EQUATION

In this appendix problems, related with the non-uniqueness of the solution of boundary integral equations of the type presented in chapter four will be investigated. It is shown in this appendix, that the solutions of the integral equations for the exterior Dirichlet and Neumann problems are non-unique, for certain frequencies. As a consequence, the numerical solution, of the discretized integral equation may be inaccurate, depending on the frequency. The same problems will occur in the solution of the diffraction problem for a transparent boundary, when using the solution scheme of chapter five.
Following (Schenck, 1968) I have used additional null field equations, to overcome these problems, (see chapter 4). It will be shown, that supplementing the integral equation with a null field equation, will eliminate the mentioned problems.
In the following I shall extend Schenck's results from the acoustic, to the elastodynamic case. In the derivations some fundamental results are used, derived by Kupradze (1956,1963) regarding integral equations for elastodynamic diffraction problems.
Since Kupradze's results were derived for smooth boundary surfaces ∂V, the following results are limited to the same class of surfaces.

1. The equation of the first kind for the Dirichlet problem

The integral equation for the exterior Dirichlet problem is, from (4.2)

$$\oint_{\partial V} u_i^k(\mathbf{y},\mathbf{x}) t_i(\mathbf{y}) dA(\mathbf{y}) = u_k^0(\mathbf{x}) \ , \ \mathbf{x} \in \partial V \tag{C.1}$$

The homogeneous equation

$$\int_{\partial V} u_i^k(\mathbf{y},\mathbf{x}) t_i(\mathbf{y}) dA(\mathbf{y}) = 0 \ , \ \mathbf{x} \in \partial V \tag{C.2}$$

can be identified directly as the homogeneous equation for the interior Dirichlet problem.
It follows, that the homogeneous equation (C.2) has nontrivial solutions, the internal "Dirichlet eigenvibrations", for frequencies, coinciding with the discrete spectrum of real eigenfrequencies, of the volume V.
As a consequence, the solution of the inhomogeneous equation (C.1) is not unique, for the internal eigenfrequencies.

2. The equation of the second kind for the Neumann problem

The integral equation for the exterior Neumann problem, for a smooth boundary surface ∂V follows from (4.2), with $c_i^k(\mathbf{x}) = \frac{1}{2}\delta_{ik}$

$$\int_{\partial V} u_i(\mathbf{y}) \tau_{ij}^k(\mathbf{y},\mathbf{x}) n_j(\mathbf{y}) dA(\mathbf{y}) = \frac{1}{2} u_k(\mathbf{x}) - u_k^0(\mathbf{x}) \ , \ \mathbf{x} \in \partial V \tag{C.3}$$

It will be shown, that non trivial solutions exist of the homogeneous version of (C.3) ($u_k^0(\mathbf{x}) = 0$). Copley (1968) derived an expression for the solution of the homogeneous integral equation for the exterior acoustic Neumann problem, for frequencies coinciding with an internal Dirichlet eigenfrequency. A similar construction can be applied to the elastodynamic case.
The homogeneous integral equation is

$$\int_{\partial V} u_i(\mathbf{y}) \tau_{ij}^k(\mathbf{y},\mathbf{x}) n_j(\mathbf{y}) dA(\mathbf{y}) = \frac{1}{2} u_k(\mathbf{x}) \ , \ \mathbf{x} \in \partial V \tag{C.4}$$

Let $\mathbf{e}_m$ be the m^{th} Dirichlet eigenvibration of the domain V, for frequency ω_m.

$$-\partial_j \tau_{ij}[\mathbf{e}_m(\mathbf{x})] - \rho \omega_m^2 e_{mi}(\mathbf{x}) = 0 \ , \ \mathbf{x} \in V \tag{C.5a}$$

$$\mathbf{e}_m(\mathbf{x}) = \mathbf{0} \ , \ \mathbf{x} \in \partial V \tag{C.5b}$$

$\mathbf{e}_m$ defines the following Neumann boundary value problem for a field $\mathbf{g}_m$

$$-\partial_j \tau_{ij}[\mathbf{g}_m(\mathbf{x})] - \rho \omega_m^2 g_{mi}(\mathbf{x}) = 0 \ , \ \mathbf{x} \in V_\infty - V \tag{C.6a}$$

$$\tau_{ij}[g_m(\mathbf{x}_0^+)]n_j = \tau_{ij}[e_m(\mathbf{x}_0^-)]n_j \quad , \mathbf{x}_0 \in \partial V \tag{C.6b}$$

$\mathbf{g}_m$ *satisfies a radiation condition* (C.6c)

where $\mathbf{x}_0^{\pm} = \lim_{h \downarrow 0} \mathbf{x}_0 \pm h\,\mathbf{n}$ and $\mathbf{n}$ is the outward pointing normal vector on ∂V.
From the uniqueness theorem for the exterior Neumann problem (Kupradze,1963) it follows, that $\mathbf{g}_m$ is uniquely defined by (C.4a,b,c).
Applying the representation theorem (B.7) to $\mathbf{g}_m$ we have

$$\int_{\partial V} \{\, g_{mi}(\mathbf{y})\tau_{ij}^k(\mathbf{y},\mathbf{x})n_j(\mathbf{y}) - \tau_{ij}[\mathbf{g}_m(\mathbf{y})]n_j(\mathbf{y})u_i^k(\mathbf{y},\mathbf{x})\}\, dA(\mathbf{y}) = \begin{cases} g_{mk}(\mathbf{x}) & , \mathbf{x} \in V_\infty - V \\ \frac{1}{2} g_{mk}(\mathbf{x}) & , \mathbf{x} \in \partial V \\ 0 & , \mathbf{x} \in V \end{cases} \tag{C.7a,b,c}$$

the second term in the surface integral

$$I_k(\mathbf{x}) = \int_{\partial V} \tau_{ij}[\mathbf{g}_m(\mathbf{y})]n_j(\mathbf{y})u_i^k(\mathbf{y},\mathbf{x})dA(\mathbf{y})$$

can be related to the integral representation of the internal Dirichlet eigenvibration $\mathbf{e}_m$

$$\int_{\partial V} \tau_{ij}[\mathbf{e}_m(\mathbf{y})]n_j(\mathbf{y})u_i^k(\mathbf{y},\mathbf{x})dA(\mathbf{y}) = \begin{cases} 0 & , \mathbf{x} \in V_\infty - V \\ 0 & , \mathbf{x} \in \partial V \\ e_{mk}(\mathbf{x}) & , \mathbf{x} \in V \end{cases} \tag{C.8a,b,c}$$

from (C.8b) it follows that $I_k(\mathbf{x}) = 0$, k=1,2,3.
From (C.7b) and $I_k = 0$, k=1,2,3 it follows, that $\mathbf{g}_m$ is a solution of the homogeneous integral equation for the exterior Neumann problem.

3. An integral equation of the second kind for the interior Dirichlet problem

In this section an alternative integral representation on the interior domain will be derived, for a field satisfying homogeneous Dirichlet boundary conditions. The jump condition of the surface integral involved is used in section C.4.1 in a proof of the uniqueness of the solutions of the null field equations.

The integral representation for the interior domain V with homogeneous Dirichlet boundary conditions $u_i(\mathbf{x})=0$, $\mathbf{x}\in\partial V$ is

$$\int_{\partial V} u_i^k(\mathbf{y},\mathbf{x})t_i(\mathbf{y})dA(\mathbf{y}) = \begin{cases} -u_k^0(\mathbf{x}) & , \mathbf{x}\in V_\infty - V \\ u_k(\mathbf{x}) - u_k^0(\mathbf{x}) & , \mathbf{x}\in V \end{cases} \qquad \text{(C.9a,b)}$$

Next we apply a traction operator on (C.9), using the traction $t_l(\mathbf{x}) = c_{lmjk}\partial_j^{(\mathbf{x})}u_k(\mathbf{x})n_m(\mathbf{x})$, resulting in

$$\int_{\partial V} c_{lmjk}\partial_j^{(\mathbf{x})}u_i^k(\mathbf{y},\mathbf{x})n_m(\mathbf{x})t_i(\mathbf{y})dA(\mathbf{y}) =$$

$$\int_{\partial V} D_{li}^{(2)}(\mathbf{y},\mathbf{x})t_i(\mathbf{y})dA(\mathbf{y}) = \begin{cases} -t_l^0(\mathbf{x}) & , \mathbf{x}\in V_\infty - V \\ t_l(\mathbf{x}) - t_l^0(\mathbf{x}) & , \mathbf{x}\in V \end{cases} \qquad \text{(C.10a,b)}$$

The limiting case $h\downarrow 0$, $\mathbf{x}=\mathbf{x}_0 \pm h\,\mathbf{n}(\mathbf{x}_0)$, $\mathbf{x}_0\in\partial V$ has been derived (Kupradze, 1956) as

$$\lim_{h\downarrow 0}\int_{\partial V} D_{li}^{(2)}(\mathbf{y},\mathbf{x})t_i(\mathbf{y})dA(\mathbf{y}) = \oint_{\partial V} D_{li}^{(2)}(\mathbf{y},\mathbf{x}_0)t_i(\mathbf{y})dA(\mathbf{y}) \mp \frac{1}{2}t_l(\mathbf{x}_0) \qquad \text{(C.11)}$$

this extends (C.10), with an integral equation of the second kind for the interior Dirichlet problem.

$$\oint_{\partial V} D_{li}^{(2)}(\mathbf{y},\mathbf{x})t_i(\mathbf{y})dA(\mathbf{y}) = \begin{cases} -t_l^0(\mathbf{x}) & , \mathbf{x}\in V_\infty - V \\ \frac{1}{2}t_l(\mathbf{x}) - t_l^0(\mathbf{x}) & , \mathbf{x}\in \partial V \\ t_l(\mathbf{x}) - t_l^0(\mathbf{x}) & , \mathbf{x}\in V \end{cases} \qquad \text{(C.12a,b,c)}$$

4. Uniqueness of the solutions of the null field equations

Copley (1967) and Schenck (1968) gave a proof of the uniqueness of the solution of the null field equation for the Neumann boundary value problem for scalar (acoustic) waves.
A proof - similar to Copley's - for both the Dirichlet and Neumann acoustic problems

was given by Colton and Kress (1983b).
The proof of Colton and Kress is based on some fundamental results for integral representations for scalar problems and the uniqueness theorem for the exterior boundary value problems for the scalar (Helmholtz) equation.
Kupradze (1956,1963), derived equivalent results , jump conditions of the integral representation at the boundary and uniqueness theorems for the exterior Dirichlet and Neumann problems for the elastodynamic equation. Using Kupradze's results we can extend the result of Colton and Kress from the acoustic, to the elastodynamic case.

The importance of the uniqueness proof for the solution of the null field equation in this context is, that it also results in a unique solution of the combined integral/null field equations introduced in chapter 4. This in its turn can be used to resolve the problems with the numerical solution scheme for the coupled finite element / integral equation, introduced in chapter 5.
In practice , the result of this proof is somewhat weakened by the fact, that the null field equation requires a potential field from a surface source density to vanish, throughout the interior domain V. In implementations however one uses a finite set of discrete evaluation points of this potential. In case all evaluation points coincide with a root of the (non zero) potential, the requirements of the null field equation will not be met.
In applications, the locations of the evaluation points of the null field equation have to be chosen carefully.

4.1. The null field equation for the Dirichlet problem

The null field equation follows from the integral representation for the exterior domain, (4.2), applying the boundary condition $u_i(\mathbf{x}) = 0$, $\mathbf{x} \in \partial V$

$$-\int_{\partial V} u_i^k(\mathbf{y},\mathbf{x}) t_i(\mathbf{y}) dA(\mathbf{y}) = -u_k^0(\mathbf{x}) \quad , \mathbf{x} \in V \tag{C.13}$$

Suppose the null field equation has more than one solution. Then there exists a non-trivial solution ϕ of the homogeneous equation.

$$\int_{\partial V} u_i^k(\mathbf{y},\mathbf{x}) \phi_i(\mathbf{y}) dA(\mathbf{y}) = 0 \quad , \mathbf{x} \in V \tag{C.14}$$

Now consider the integral representation

$$\int_{\partial V} u_i^k(\mathbf{y},\mathbf{x}) \phi_i(\mathbf{y}) dA(\mathbf{y}) = w_k(\mathbf{x}) \tag{C.15}$$

a single layer potential which satisfies the elastodynamic equation plus radiation condition in the exterior domain $V_\infty - V$ and from (C.14), $\mathbf{w}(\mathbf{x}) = \mathbf{0}$, $\mathbf{x} \in V$.
Furthermore from the continuity of (C.15) at the boundary (Kupradze, 1956), it follows that $\mathbf{w}(\mathbf{x})$ satisfies the homogeneous Dirichlet condition on ∂V.

From the uniqueness theorem for the Dirichlet boundary value problem (Kupradze, 1956,1963), it follows $\mathbf{w}(\mathbf{x}) = \mathbf{0}$, $\mathbf{x} \in V_\infty - V$
Next we apply the traction operator to (C.15)

$$t_l(\mathbf{x}) = c_{lmjk}\partial_j w_k(\mathbf{x}) n_m(\mathbf{x}) = \int_{\partial V} D_{li}^{(2)}(\mathbf{y},\mathbf{x})\phi_i(\mathbf{y}) dA(\mathbf{y}) \tag{C.16}$$

In the limit from both sides of the boundary surface , $\mathbf{x} = \mathbf{x}_0 \pm h\,\mathbf{n}(\mathbf{x}_0)$, $\mathbf{x}_0 \in \partial V$ we have

$$\lim_{h \downarrow 0} t_l(\mathbf{x}) = \int_{\partial V} D_{li}^{(2)}(\mathbf{y},\mathbf{x}_0)\phi_i(\mathbf{y}) dA(\mathbf{y}) \mp \frac{1}{2}\phi_l(\mathbf{x}_0)$$

(see also (C.11)) , or $[t_l(\mathbf{x}_0)]^{\pm} = -\phi_l(\mathbf{x}_0)$.
Since $\mathbf{w}(\mathbf{x}) = 0$, $\forall \mathbf{x}$ we have $t_l(\mathbf{x}) = 0$ and consequently $\phi(\mathbf{x}_0) = \mathbf{0}$, the trivial solution.
Therefore the solution of the null field equation for the Dirichlet problem is unique.

4.2. The null field equation for the Neumann problem

The null field equation follows from the integral representation for the exterior domain, (4.2), applying the boundary condition $t_i(\mathbf{x}) = \tau_{ij}(\mathbf{x}) n_j(\mathbf{x}) = 0$, $\mathbf{x} \in \partial V$

$$\int_{\partial V} \tau_{ij}^k(\mathbf{y},\mathbf{x}) u_i(\mathbf{y}) n_j(\mathbf{y}) dA(\mathbf{y}) = -u_k^0(\mathbf{x}) \quad , \mathbf{x} \in V \tag{C.17}$$

Suppose the solution of (C.17) is not unique, then there exists a nontrivial solution ψ of the homogeneous equation

$$\int_{\partial V} \tau_{ij}^k(\mathbf{y},\mathbf{x}) \psi_i(\mathbf{y}) n_j(\mathbf{y}) dA(\mathbf{y}) = 0 \quad , \mathbf{x} \in V \tag{C.18}$$

Now consider the integral representation

$$\int_{\partial V} \tau_{ij}^k(\mathbf{y},\mathbf{x}) \psi_i(\mathbf{y}) n_j(\mathbf{y}) dA(\mathbf{y}) = w_k(\mathbf{x}) \tag{C.19}$$

This double layer potential $\mathbf{w}$ satisfies the elastodynamic equation in $V_\infty - V$ and from (C.18) we have $\mathbf{w}(\mathbf{x}) = \mathbf{0}$, $\mathbf{x} \in V$. Kupradze (1956,1963) that the traction vector $t_i[\mathbf{w}]$ is continuous across ∂V and that $\mathbf{w}$ satisfies a radiation condition.
From the continuity property and $\mathbf{w}(\mathbf{x}) = \mathbf{0}$, $\mathbf{x} \in V$, it follows, that $\mathbf{w}$ satisfies the

homogeneous Neumann condition on ∂V. From the uniqueness theorem for the exterior Neumann problem it then follows $\mathbf{w}(\mathbf{x}) = \mathbf{0}$, $\mathbf{x} \in V_\infty - V$.
From the jump condition for the double layer potential (Kupradze, 1956,1963) we have for $\mathbf{x} = \mathbf{x}_0 \pm h\,\mathbf{n}(\mathbf{x}_0)$, $\mathbf{x}_0 \in \partial V$

$$\lim_{h \downarrow 0} w_k(\mathbf{x}) = \int_{\partial V} \tau_{ij}^k(\mathbf{y},\mathbf{x}_0)\psi_i(\mathbf{y})dA(\mathbf{y}) \pm \frac{1}{2}\psi_k(\mathbf{x}_0)$$

or $[w_k(\mathbf{x}_0)]_-^+ = \psi_k(\mathbf{x}_0)$
Since $\mathbf{w}(\mathbf{x}) = 0$, $\forall \mathbf{x}$, we have $\psi(\mathbf{x}_0) = \mathbf{0}$ - the trivial solution - which proves the uniqueness of the solution to the null field equation for the Neumann problem.

Appendix D

AN IMPLEMENTATION OF THE HYBRID FINITE ELEMENT / BOUNDARY INTEGRAL EQUATION METHOD IN A PROGRAM PACKAGE

This appendix describes the HYBRID program package. The HYBRID package is an implementation of the hybrid finite element / boundary integral equation solution of the wave equation, for inhomogeneous media, consisting of a regular medium (regular in the sense, that an algorithm for the Green's state is available), with a single irregular inclusion of finite volume .
The programs have been written in FORTRAN 77 and have been tested on several computer systems, a Gould PN6080 running UNIX and a CDC cyber 855 under the NOS/BE operating system.
The present implementation is limited to 2-D media and horizontally polarized (SH) waves. A further limitation is imposed by the algorithms for the computation of the Green's state of the regular medium. In the present implementation the regular medium is a homogeneous (half) space.
The package consists of seven programs for the specification of the model of the medium, the model excitation and the computation of the model response to the excitation. The data to be transferred between different programs of the package are stored in disk files. The interdependence of the different programs in the package and the data files used by these programs is illustrated in the hierarchy diagram of figure D.1. Besides input / output with the direct access files, the programs read parameters and options from input files - created with an editor program - and write some output to a log file, that can be printed for inspection.
The model response is computed in the frequency domain in the form of multiplexed frequency spectra, for a number of wave field evaluation points. To obtain synthetic seismograms some postprocessing has to be done on the multiplexed response spectra, namely demultiplexing and either inverse Fourier transformation or computation of amplitude spectra, (both optionally preceded by filtering in the frequency domain) Resulting time traces or amplitude spectra can be displayed on a graphics terminal or a plotter.
The package has been split up in seven programs, that run separately. This way a

maximum flexibility and efficiency is achieved. In a modeling experiment several parameters can be changed without having to repeat all the previous calculations. Only those interim results are recomputed, that are affected by the modified parameters. If for example we want to apply several wave field excitations (plane waves, point sources or coincident sources / receivers), we only have to rerun the program dealing with the model excitation (program excit - see below) and use the original files produced in the other programs. Likewise it is relatively cheap to change the position of the field evaluation points (receiver positions). Only the data in files depending on the receiver positions have to be recomputed. If we want to change the material parameters of the scattering irregularity, leaving the geometry of its boundary unchanged, we only have to rerun the programs dealing with the finite element calculations (hyafp and fem - see below).

1. Description of the programs

The principal programs are (see figure D.1):

(1) hyafp
In this program, the model of the scattering obstacle is specified, in terms of geometry and physical parameters. A finite element mesh is generated and the stiffness and mass matrices **S** and **M** required in the hybrid formulation are computed and stored in the file FEMMOD. The program consists largely of a number of calls to subroutines of a general purpose finite element package (AFEP) library, (Segal, 1981).

(2) fem
Here the boundary traction matrix **D** (independent of ω) is computed first. Next the program computes the reduced dynamic stiffness matrix $\mathbf{W}(\omega)$ (see chapter 5)

$$\mathbf{W} = \mathbf{Z}_{RR} - \mathbf{Z}_{RI}\mathbf{Z}_{II}^{-1}\mathbf{Z}_{IR}$$

in a program loop over discrete frequencies in the specified bandwith. Results are written to a file FEM.

(3) grmat
The integral representations occurring in the hybrid formulation are discretized in this program, using the finite element type interpolation for the wave field and Gauss-Legendre numerical integration, to evaluate the integral coefficients, (see section 4.4.2.1).
The program is run in one of three possible modes, corresponding with evaluation points of the integral representation a) on the boundary of the scatterer, b) in the exterior of the scatterer and c) in the interior of the scatterer.
Model geometry data and physical parameters are read from the file FEMMOD, resulting matrix rows are written to one of three output files GMM, GMR, or GMI, corresponding with the three program modes mentioned.

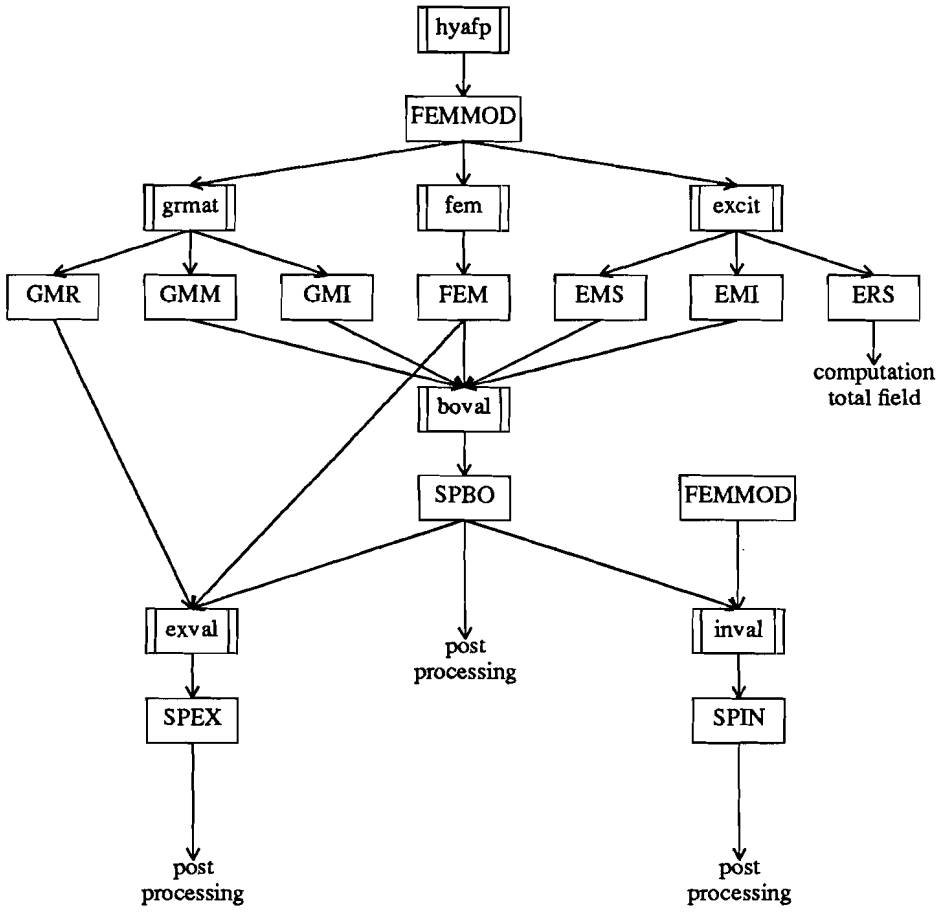

figure D.1 Hierarchy diagram of the HYBRID package, showing the flow of data via files (simple boxes) between programs (double sided boxes) of the package.

(4) excit
In this program, values of the incident displacement field u^0 occurring in the right hand side of the equations are computed.
The program is run in three modes similar to program grmat.

(5) boval
This program computes the boundary field, solving the finite element / boundary integral equations. Finite element input (the reduced stiffness matrix **W** is read from file FEM , matrix rows from the discretized integral representation are read from files GMM (boundary evaluation points) and optionally GMI (null field evaluation points). Incident field values are read from files EMS (boundary

points) and optionally EMI (null field points). Multiplexed spectra of the boundary points are written to the output file SPBO

(6) inval
Here the displacement field is computed in evaluation points in the interior of the scattering volume. The field values are computed solving the Dirichlet boundary value problem. The boundary values are read from the file SPBO (output from program boval). The necessary finite element data are read from file FEMMOD. Output is written to a file named SPIN.

(7) exval
In this program scattered displacement field values in evaluation points in the exterior of the scatterer are computed, evaluating the integral representation for the scattered field. Matrix rows of the discretized integral representation are read from file GMR (output from program grmat). Boundary field data are read from file SPBO (output boval). For a transparent scatterer SPBO contains boundary displacement values, the necessary boundary tractions are computed first from the boundary displacements, using the transformation matrices read from file FEM. Output is written to a file SPEX.

2. Data files used in the program package

The following data files are used by the program package:

(1) FEMMOD
Output from program hyafp. This file contains geometry data (nodal point coordinates) and finite element interim data (static stiffness matrix, mass matrix).

(2) FEM
Output from program fem . This file contains geometry data, a frequency independent boundary traction matrix and (for a number of frequencies) the reduced stiffness matrix $\mathbf{W}$.

(3) GMR
Output from program grmat . This file contains geometry data and the frequency dependent matrix of the discretized integral representation, for evaluation in the exterior of the scatterer.

(4) GMM
Output from program grmat . This file contains geometry data and the frequency dependent matrix of the discretized integral equation, for evaluation points on the boundary of the scatterer.

(5) GMI
Output from program grmat . This file contains geometry data and the frequency dependent matrix of the discretized integral representation, for evaluation points of the null field representation in the interior of the scatterer.

(6) EMS
Output from program excit . This file contains incident field values $u^0(\mathbf{x}_R)$, for evaluation points $\mathbf{x}_R$ on the boundary of the scatterer. These values appear in the right-hand side of the integral equations for the boundary field.

(7) EMI
Output from program excit . This file contains incident field values $u^0(\mathbf{x}_R)$, for evaluation points $\mathbf{x}_R$ in the interior of the scatterer. These values appear in the right-hand side of the null field equations for the boundary field.

(8) ERS
Output from program excit . This file contains incident field values $u^0(\mathbf{x}_R)$, for evaluation points $\mathbf{x}_R$ in the exterior of the scatterer. Adding these data to the corresponding values of the scattered field computed in program exval (file SPEX) - $u(\mathbf{x}_R) = u^{sc}(\mathbf{x}_R) + u^0(\mathbf{x}_R)$ - will give the total displacement field values in the receivers $\mathbf{x}_R$.

(9) SPBO
Output from program boval . It contains the boundary solution - multiplexed displacement or traction values in the boundary nodal points.

(10) SPEX
Output from program exval . It contains the evaluation of the scattered field $u^{sc}(\mathbf{x}_R)$ in a number of external receiver points $\mathbf{x}_R$ in multiplexed format.

(11) SPIN
Output from program inval . The file contains displacement field values $u(\mathbf{x}_R)$ in a number of internal receiver points $\mathbf{x}_R$ in multiplexed format.

3. Computer time requirements

An indication of the amount of time the central processing unit (cpu) is occupied by the different programs of the package is given in table D.1 below. Listed are the cpu times used for the modeling problems discussed in chapter 6.
The numbers given are maximum estimates for the cpu requirements, because they include a fraction of system overhead, that depends on the total workload of the multi-tasking system on which the programs have been run. The cpu times listed are for a Gould PN6080 computer, with a floating point accelerator.
The cpu times depend linearly on the number of frequency points in the computations, listed are the cpu times in seconds per frequency point.
Only the three most time consuming programs, grmat, fem and boval are listed (see D.2 for a program description), the costs of the other programs are an order of magnitude smaller.
The cpu times strongly depend on the model size, the first numerical columns of the table contain the maximum dimensionless wavenumber, the number of boundary points n_b, the number of null field points n_s and the number of internal points in the finite element grid.

model	section	ka_{max}	n_b	n_s	n_i	grmat	fem	boval	total cpu
cylinder	6.1	10.47	60	8	196	20	37	27	84
square(1)	6.2.1	10.47	60	8	196	19	36	30	85
canyon	6.3.1	47.12	81	9	-	45	-	35	80
fill	6.3.2	47.12	81	9	780	45	230	67	342

table D.1 Cpu time requirements (in seconds per frequency value), for the models of chapter 6 - see text.

REFERENCES

Abramowitz, M., and Stegun, I., 1964. *Handbook of mathematical functions*, New York, Dover.

Aki, K. and Larner, K. L., 1970. Surface Motion of a Layered Medium Having an Irregular Interface due to Incident Plane SH Waves, *J. Geophys. Res.*, **75**, 933-954.

Aki, K., and Richards, P. G., 1980. *Quantitative Seismology*, San Francisco, W.H. Freeman.

Alford, R.M., Kelly, K.R., and Boore, D.M., 1974. Accuracy of finite-difference modelling of the acoustic wave equation, *Geophysics*, **39**, 834-842.

Banaugh, R. P., and Goldsmith, N., 1963. Diffraction of steady acoustic waves by surfaces of arbitrary shape, *J. Ac. Soc. Am.*, **35**.

Bard, P.Y. and Bouchon, M., 1980. The seismic response of sediment-filled valleys. Part 1. The case of incident SH waves, *Bull. Seism. Soc. Am.*, **70**, 1263-1286.

Bastians M. W. J. M., 1986. *Fast evaluation of complete synthetic SH seismograms based on asymptotic mode theory*, PhD Thesis, Utrecht University.

Belytschko, T., and Mullen, R., 1978. On dispersive properties of finite element solutions. In , *Modern Problems in Elastic Wave Propagation*, eds Julius Miklowitz, and Jan D. Achenbach. Wiley.

Ben-Menahem, A., and Singh, S. J., 1981. *Seismic waves and sources*, Springer Verlag.

Berkhoff, J.C.W., 1974. Linear wave propagation problems and the finite element method. In *Finite elements in fluids 1, Viscous flow and hydrodynamics*, proceedings "International Symp. on the f.e.m. in flow problems", Univ. College of Wales, eds. Oden, J.T., Taylor, C., Gallagher, R.H. and Zienkiewicz, O.C.

Berkhoff, J.C.W., 1976. *Mathematical models for simple harmonic linear water waves wave diffraction and refraction*, PhD Thesis, Techn. Univ. Delft.

Bolomey, J.-C. and Tabbara , W., 1973. Numerical aspects on coupling between complementary boundary value problems., *IEEE Transactions on Antennas and propagation*, **AP-21**, 356-363.

Boore, D. M., 1972. Finite difference methods for seismic wave propagation in heterogeneous materials. In *Seismology: Surface waves and earth oscillations*, ed B.A. Bolt, **11**, Academic Press.

Boore, D. M., Larner, K., and Aki, K., 1971. Comparison of two independent methods for the solution of wave scattering problems: Respons of a sedimentary basin to vertically incident SH waves, *J. Geophys. Res.*, **76**, 558-569.

Bouchon, M. and Aki , K., 1977. Near-field of a seismic source in a layered medium with irregular interfaces, *Geophys. J. R. Astr. Soc.*, **50**, 669-684.

Brebbia C. A., 1978. *The Boundary Element Method for Engineers*, London, Pentech Press.

Burton, A.J., and Miller, G.F., 1971. The application of integral equation methods to the numerical solution of some exterior boundary value problems., *Proc. Roy. Soc. London*, Ser. A, **323**, 201-210.

Chin, R.C.Y., Hedstrom, G. and Thigpen, L., 1984. Numerical Methods in Seismology, *J. Comp. Phys.*, **54**, 18-56.

Colton, D. and Kress, R., 1983. *Integral Equation Methods in Scattering Theory*, New York, John Wiley. 669-684.

Colton, D. and Kress, R. , 1983. The unique solvability of the null field equations, *Q. Jl. Mech. Appl. Math.*, **36**, 87-95.

Cooley, J.W., and Tukey, S.W., 1965. An algorithm for the machine calculation of complex Fourier series, *Math. Comp.*, **19**, 297-301.

Copley L. G., 1967. Integral equation method for radiation from vibrating bodies, *J. Ac. Soc. Am.*, **41**, 807-816.

Copley, L.G., 1968. Fundamental results concerning integral representations in acoustic radiation, *J. Ac. Soc. Am.*, **44**, 28-32.

Courant, R., and Hilbert, D., 1968. *Methoden der Mathematischen Physik*, Berlin, Springer-Verlag.

Crichlow, J. M., Beckels, D., and Aspinall, W.P., 1984. Two-dimensional analysis of the effect of subsurface anomalies on the free surface respons to incident SH-waves, *Geophys. J. R. Astr. Soc.*, **79**, 495-511.

Day, S.M., 1977. *Finite element analysis of seismic scattering problems*, PhD Thesis, Univ. Cal., San Diego.

Desai, C.S., and Abel, J.F., 1972. *Introduction to the Finite Element Method*, New York, van Nostrand Reinhold.

Dongarra, J.J., Moler, C.B., Bunch, J.R., and Stewart, G.W., 1979. *LINPACK User's Guide*, Philadelphia, SIAM.

Eringen, A. C., and Suhubi, E. S., 1975. *Elastodynamics*, New York, Academic Press.

Harvey D. J., 1981. Seismogram synthesis using normal mode superposition: the locked mode approximation, *Geophys. J. R. astr. Soc.*, **66**, 37-70

Hoenl, H., Maue, A.W., and Westpfahl, K., 1961. Theorie der Beugung. In *Handbuch der Physik*, ed S. Fluegge, **25**, 218-583, Springer.

Hong, M., and Bond, L.J., 1986. Application of the finite difference method in seismic source and wave diffraction simulation, *Geophys. J. R. Astr. Soc.*, **87**.

De Hoop. A.T., 1958. *Representation theorems for the displacement in an elastic solid and their application to elastodynamic diffraction theory*, PhD Thesis, Techn. Univ. Delft.

Kelly, K. R., 1983. Numerical study of Love wave propagation, *Geophysics*, **48**, 833-853.

Kelly, K. R., Ward, R. W., Treitel, S., and Alford, R. M., 1976. Synthetic seismograms: a finite difference approach, *Geophysics*, **41**, 2-27.

Kennett, B.L.N., 1983. *Seismic wave propagation in stratified media*, Cambridge University Press.

Kuepper, F.J., 1958. Theoretische Untersuchungen ueber die Mehrfachaufstellung von Geophonen, *Geophys. Prosp.*, **6**, 194-256.

Kummer B., Behle A., Dorau F., 1987. Hybrid modeling of elastic-wave propagation in two-dimensional laterally inhomogeneous media, *Geophysics*, **52**, 765-771.

Kupradze, V. D., 1956. *Randwertaufgaben der Schwingungstheorie und Integralgleichungen*, Berlin, VEB Deutscher Verlag der Wissenschaften.

Kupradze, V. D., 1963. Dynamical problems in elasticity. In *Progress in solid mechanics*, eds I.N. Sneddon and R. Hill, Vol. 3.

Levander, A.R., and Hill, N.R., 1985. P-SV resonances in irregular low velocity surfaces, *Bull. Seism. Soc. Am.*, **75**, 847-864.

Lysmer J., Kuhlemeyer R. L., 1969. Finite dynamic model for infinite media, *Journal of the engineering mechanics division - proceedings of the American Society of Civil Engineers.*

Lysmer, J., and Drake, L. A., 1971. The propagation of Love waves across nonhorizontally layered structures, *Bull. Seism. Soc. Am.*, **61**, 1233-1251.

Marfurt, K. J., 1984. Accuracy of finite difference and finite element modeling of the scalar and elastic wave equations, *Geophysics*, **49**, 533-549.

Mitchell, A. R., 1969. *Computational methods in partial differential equations*, New York, Wiley.

Morse P. M., Fesbach H., 1953. *Methods of theoretical Physics*, New York, MCGraw-Hill.

Morse P. M., Ingard K. U., 1968. *Theoretical Acoustics*, New York, MCGraw-Hill. Mostow G. D., Sampson J. H., Meyer J.P., 1963. *Fundamental Structures of Algebra*, New York, McGraw-Hill.

Olsen, K., and Hwang, L. S., 1971. Oscillations in a bay of arbritrary shape and variable depth, *J. Geophys.Res.*, **76**, 5048-5064.

Ralston, A., 1965. *A first course in numerical analysis*, New York, McGraw-Hill.

Reynolds, A. C., 1978. Boundary conditions for the numerical solution of wave propagation problems, *Geophysics*, **43**, 1099-1111.

Sanchez-Sesma, F. J., 1983. Diffraction of elastic waves by three dimensional surface irregularities, *Bull. Seism. Soc. Am.*, **73**, 1621-1636.

Sanchez-Sesma, F. J., Herrera, I., and Aviles , J., 1982. A boundary method for elastic wave diffraction: application to scattering of SH waves by surface irregularities, *Bull. Seism. Soc. Am.*, **72**, 473-490.

Schenck, H. A., 1968. Improved integral formulation for acoustic radiation problems, *J. Ac. Soc. Am.*, **44**, 41-58.

Schuster, G.Th., 1984. *Some boundary integral equation methods and their application to seismic exploration*, PhD Thesis, Univ. Columbia.

Segal, A., 1980. *AFEP user manual*, , Dept. of Math. Techn. University Delft.

Shtivelman V., 1984. A hybrid method for wave-field computation (SH-Wave), *Geophys. Prosp.*, **32**, 236-257.

Shtivelman V., 1985. Two-dimensional acoustic modeling by a hybrid method, *Geophysics*, **50**, 1273-1284.

Sills L. B., 1978. Scattering of horizontally-polarized shear waves by surface irregularities. *Geophys. J. R. Astr. Soc.*, **54**, 319-348.

Sharma, D. L., 1967. Scattering of steady elastic waves by surfaces of arbitrary shape, *Bull. Seism. Soc. Am.*, **57**, 795-812.

Smith, W. D., 1974. A non reflecting plane boundary for wave propagation problems, *J. Comp. Phys.*, **15**, 492-503.

Smith, W. D., 1975. The application of finite element analysis to bodywave propagation problems, *Geophys. J. R. Astr. Soc.*, **42**, 747-768.

Stoer, J., 1972. *Einfuehrung in die numerische Mathematik I*, Berlin, Springer-Verlag.

Strang, G., and Fix, G.J., 1973. *An analysis of the finite element method*, Prentice-Hall.

Tan, T. H., 1975. Scattering of elastic waves by elastically transparant obstacles, *Appl. Sci. Res.*, **31**, 29-51.

Tan, T. H., 1975. *Diffraction theory for time harmonic elastic waves*, PhD Thesis, Techn. Univ. Delft.

Tobocman, W., 1984. Calculation of acoustic wave scattering by means of the Helmholtz integral equation, *J. Ac. Soc. Am.*, **76**, 599-607.

Van den Berg, A. P., 1984. A hybrid solution of wave propagation problems in regular media with bounded irregular inclusions, *Geophys. J. R. Astr. Soc.*, **79**, 3-10.

Van den Berg, A., 1987. A hybrid solution for wave propagation problems in inhomogeneous media, In *Mathematical Geophysics*, eds. N. J. Vlaar, G. Nolet, M. J. R. Wortel & S. A. P. L. Cloetingh, Reidel

Waters K., 1978. *Reflection Seismology*, New York, Wiley Interscience.

Wilkinson, J. H., 1965. *The algebraic eigenvalue problem*, Oxford University Press.

Wilton, D.T., 1978. Acoustic radiation and scattering from elastic structures., *Int. J. Num. Meth. Eng.*, **13**, 123-138.

Wong, H. L., and Jennings, P. C., 1975. Effects of canyon topography on strong ground motion, *Bull. Seism. Soc. Am.*, **65**, 1239-1257.

Zahradnik J., 1978. SH-wave propagation around inclusions of dimensions comparable to the wavelength, *Travaux de l'institut de l'academie tchecoslovaque des sciences*, **N455**, 131-148.

Zahradnik, J., and Urban, L., 1984. Effect of a simple mountain range on underground seismic motion, *Geophys. J. R. Astr. Soc.*, **79**, 167-183.

Zienkiewicz, O. C., 1977. *The finite element method*, 3rd edition, McGraw-Hill.

Zienkiewicz, O. C., Kelly, D. W., and Bettes, P., 1977. The coupling of the finite element method and boundary solution procedures, *Int.J. Num. Meth. Engineering*, **11**, 355-375.

CURRICULUM VITAE

De schrijver van dit proefschrift behaalde in 1969 het diploma HBS-B aan de Rijks HBS (thans Rijks Scholengemeenschap) te Oud-Beijerland. In dat zelfde jaar werd begonnen met de studie geologie aan de Rijksuniversiteit te Utrecht. In 1974 werd het kandidaatsexamen G4 afgelegd. Het doctoraalexamen geofysica met hoofdrichting fysica van de vaste aarde en bijvakken numerieke wiskunde en mathematische fysica werd in 1977 cum laude behaald. Vanaf 1978 is hij als wetenschappelijk medewerker verbonden aan de afdeling Theoretische Geofysica van het Instituut voor Aardwetenschappen van de Rijksuniversiteit Utrecht.

NASCHRIFT

Aan verschillende personen ben ik dank verschuldigd voor hun bijdragen tot het totstandkomen van dit proefschrift.
In de eerste plaats wil ik mijn promotor Professor N. J. Vlaar bedanken voor zijn ondersteuning en voor de discussies naar aanleiding van het onderzoek.
Mijn collega's bij de vakgroep geofysica bedank ik voor de plezierige samenwerking.
Rene Bastians en Roel Snieder bedank ik voor het suggereren van verbeteringen in het manuscript.
Guus Segal van de Technische Universiteit Delft dank ik voor het hulpvaardig ter beschikking stellen van de AFEP bibliotheek van eindige elementen routines.
Henk van der Vorst voormalig medewerker van het Academisch Computer Centrum Utrecht (thans werkzaam bij de Technische Universiteit Delft) dank ik voor verschillende adviezen met betrekking tot numeriek wiskundige problemen en het beschikbaar stellen van de LINPACK bibliotheek van lineaire algebra routines.
I thank Professor V. Červený and Dr. J. Zahradnik of the Charles University of Prague for their hospitality, offered to me during a working visit to Czechoslovakia. I want to thank Jiři Zahradnik for the inspiring discussions we had on the seismic modeling subject and for the effort he put into several numerical modeling experiments, performed to compare his finite difference approach with the hybrid method presented in this thesis.
Tenslotte wil ik Annemiek, mijn vrouw bedanken voor het geduld dat zij toonde gedurende menig weekend en avondlijk uur, dat ik aan het onderzoek van dit proefschrift werkte.